SEARCH FOR BLACK HOLES IN MULTIPARTICLE FINAL STATE IN PROTON-PROTON COLLISIONS AT $\sqrt{S} = 13$ TEV WITH CMS DETECTOR

MOHAMMAD JAVAD SOLEIMANI

FACULTY OF SCIENCE
UNIVERSITY OF MALAYA
KUALA LUMPUR

2017

SEARCH FOR BLACK HOLES IN MULTIPARTICLE FINAL STATE IN PROTON-PROTON COLLISIONS AT $\sqrt{S} = 13$ TEV WITH CMS DETECTOR

MOHAMMAD JAVAD SOLEIMANI

DISSERTATION SUBMITTED IN FULFILMENT OF THE REQUIREMENTS FOR THE DEGREE OF MASTER OF SCIENCE

FACULTY OF SCIENCE
UNIVERSITY OF MALAYA
KUALA LUMPUR

2017

UNIVERSITI MALAYA

ORIGINAL LITERARY WORK DECLARATION

Name of Candidate: (I.C./Passport No.:)

Registration/Matrix No.:

Name of Degree:

Title of Project Paper/Research Report/Dissertation/Thesis ("this Work"):

Field of Study:

I do solemnly and sincerely declare that:

(1) I am the sole author/writer of this Work;
(2) This work is original;
(3) Any use of any work in which copyright exists was done by way of fair dealing and for permitted purposes and any excerpt or extract from, or reference to or reproduction of any copyright work has been disclosed expressly and sufficiently and the title of the Work and its authorship have been acknowledged in this Work;
(4) I do not have any actual knowledge nor do I ought reasonably to know that the making of this work constitutes an infringement of any copyright work;
(5) I hereby assign all and every rights in the copyright to this Work to the University of Malaya ("UM"), who henceforth shall be owner of the copyright in this Work and that any reproduction or use in any form or by any means whatsoever is prohibited without the written consent of UM having been first had and obtained;
(6) I am fully aware that if in the course of making this Work I have infringed any copyright whether intentionally or otherwise, I may be subject to legal action or any other action as may be determined by UM.

Candidate's Signature Date:

Subscribed and solemnly declared before,

Witness's Signature Date:

Name:
Designation:

SEARCH FOR BLACK HOLES IN MULTIPARTICLE FINAL STATE IN PROTON-PROTON COLLISIONS AT $\sqrt{S} = 13$ TEV WITH CMS DETECTOR

ABSTRACT

Quantum gravity can become strong at a TeV energy scale in the bulk space-time in the context of large extra dimension, and could lead to microscopic black holes being produced and observed by the Large Hadron Collider (LHC) experiments. A search for black holes using a data sample corresponding to an integrated luminosity of 2.2 fb^{-1} collected with the CMS experiment at the LHC in pp collisions at a center-of-mass energy of 13 TeV in 2015 is presented. No excess characteristic of a black hole production or other new physics signals resulting in energetic multiparticle final states was observed. Standard model background, dominated by QCD multijet production, was determined exclusively from control regions in data, without any reliance on simulation. Model-independent limits on the cross section of a new physics signal in these final states are set and further interpreted in terms of limits on black hole production. In the context of models with large extra dimensions, semiclassical black holes with masses below ~ 8.7 TeV and quantum black holes with masses below ~ 8 TeV are excluded by this search, thus significantly extending limits set in the LHC Run 1.

Keywords: Microscopic Black Hole, Hierarchy Problem, Generalized Uncertainty Principle.

ABSTRAK

Graviti kuantum boleh menjadi kukuh pada skala tenaga karena justru di sebahagian besar ruang-masa dalam konteks dimensi yang lebih besar, dan boleh membawa kepada lubang hitam mikroskopik yang dikeluarkan dan dipatuhi oleh eksperimen LHC. Satu carian untuk lubang hitam menggunakan sampel data yang sepadan dengan kilauan bersepadu 2.2 fb^{-1} dikumpul dengan eksperimen CMS pada LHC dalam perlanggaran pp pada tenaga pusat-of-jisim 13 TeV pada 2015 dibentangkan. Tiada ciri melebihi pengeluaran lubang hitam atau lain-lain isyarat fizik baru menyebabkan bertenaga negeri akhir multiparticle diperhatikan. Latar belakang model Standard, dikuasai oleh pengeluaran QCD Multijet, telah ditentukan secara eksklusif dari kawasan kawalan ke atas data, tanpa apa-apa pergantungan kepada simulasi. Had Model-bebas ke atas keratan rentas isyarat fizik baru di negeri-negeri akhir ditetapkan dan seterusnya ditafsirkan dari segi had ke atas pengeluaran lubang hitam. Dalam konteks model dengan dimensi yang lebih besar, lubang hitam separuh kelasik dengan jisim di bawah $\sim$ 8.7 karenajustru TeV dan lubang hitam kuantum dengan jisim di bawah $\sim$ 8 karenajustru TeV ketepikan oleh carian ini, dengan itu ketara melanjutkan had yang ditetapkan di LHC Run 1.

ACKNOWLEDGEMENTS

First and foremost, praise be to my God for all his blessings for giving me patience and good health throughout the duration of this Master research. I would like to express my special appreciation and thanks to my research supervisor Prof. Dr. Wan Ahmad Tajuddin Wan Abdullah who has been supported me as well during my studying at UM. I am extremely grateful to him for all has taught me and his infinite amount of kindness and patience. I could have not asked for a better advisor.

Meanwhile, I would like to give special thanks to Prof. Dr. Greg Landsberg as my CMS group leader for all his kind supports and valuable guide. Appreciation is also due towards the University of Malaya for providing funding through the research grant RU-023-2014. Moreover, I express my deepest and warmest gratitude towards my dear mother, for her love and kind support, encouragements and sacrifices she made during my entire life, which without her I would never have gotten here.

My sincere thanks also goes to Dr. Tutanon Sinthuprasith and Dr. Ijaz Ahmed for fruitful discussion and also I would like to thank my friends John Charls Hakala and Martin Kwok for all their kind supports during my stay at CERN. I would also like to express my deepest appreciation to my dearest spouse Niloofar, who is always by my side when times I needed her and helped me a lot and without her, this work would not be here, and my lovable daughters, Nazanin Fatemeh and Nazanin Zeinab who served as my inspiration to pursue this undertaking.

TABLE OF CONTENTS

LIST OF FIGURES

LIST OF TABLES

CHAPTER 1: INTRODUCTION

1.1 Introduction

In our Universe, gravity is the weakest of all forces (Glashow, 1961; Weinberg 1967). Namely, the gravitational constant, $G_N \sim 10^{-38}$ GeV^{-2}, is much smaller than the electroweak constant, $G_F \sim 10^{-4}$ GeV^{-2}. Consequently, the Planck scale (energy when gravity becomes strong) is some 17 orders of magnitude higher than the electroweak scale. This is known as a hierarchy problem (Barbieri & Giudice, 1988). A number of theories exist that attempt to solve the hierarchy problem: supersymmetry, extra dimensions, etc.

In this analysis, we explore one of the possible solutions to the problem – a class of models in which n extra spatial dimensions give rise to strong gravity due to the fact that in $4 + n$ dimensions the fundamental Planck mass (M_D) can be as low as few TeV (Dimopoulos & Landsberg, 2001; Gidding & Thomas, 2002). The main two classes of models considered here are Arkani-Hamed, Dimopooulos, Dvali (ADD) model with large extra dimensions (Arkani-Hamed et al, 1998; 1999) and Randall–Sundrum (RS) model (Randall & Sundrum, 1999) with a single, warped extra dimension embedded in the anti-deSitter space (AdS_5).

In the ADD model, M_D is related to the "apparent" Planck mass in our 4-dimensional spacetime (M_{pl}) as $M_{Pl}^2 = M_D^{n+2} R^2$, where R is the spatial size of extra dimensions. Typical values of R for different n are summarized in Table 1.1. While the $n = 1$ case is ruled out by the very existence of our Solar system, higher number of extra dimensions have not been ruled out yet, and the strongest limits to date on this model come from dedicated LHC searches (see, e.g. references. (Ledroit-Guillon 2015; Landsberg, 2015) for a recent review) and range in the 4–9 TeV range depending on the model assumptions.

Table 1.1: Compactification radius R of extra dimensions n in the ADD model.

n	R
1	8×10^{12} m
2	0.7 mm
3	3 nm
4	6×10^{-12} m

In the RS model, the metric of the AdS_5 space is given by

$$ds^2 = \exp(-2kR|\varphi|)\eta_{\mu\nu}dx^\mu dx^\nu - R^2 d\varphi^2 \tag{1.1}$$

where $0 \leq |\varphi| \leq \pi$ is the coordinate along the compact dimension of radius R, k is the curvature of the AdS_5 space, often referred to as the “warp factor", x^μ are the conventional (3+1)-space-time coordinates, and $\eta^{\mu\nu}$ is the metric tensor of Minkowski space-time. Two 3-dimensional branes with equal and opposite tensions are positioned at the fixed points of the S_1/Z_2 orbifold in the AdS_5 space, at $\phi = 0$ (SM brane) and at $\phi = \pi$ (Planck brane). In this model, gravity is generated on the Planck brane, whereas at least some of the SM particles are confined to the SM brane, separated from the Planck brane in the extra dimension. Due to the warped metric in the direction of the extra dimension, operators with a characteristic size of M_{Pl} on the Planck brane give rise to exponentially suppressed energy scales on the SM brane: $M_D = \overline{M}_{Pl} \exp(-\pi kR)$, where $\overline{M}_{Pl} \equiv M_{Pl}/\sqrt{8\pi}$ is the reduced Planck scale. (In the literature this scale M_D is often referred to as Λ_π.) Thus the EWSB scale can be connected to the Planck scale with a relatively low degree of fine tuning by requiring the product of the warp factor and the compactification radius of the extra dimension to be $kR \sim 10$. In this model, R could have a “natural" value of $\sim 1/M_{Pl}$, thus offering a rigorous solution to the hierarchy problem.

The most restrictive limits on the RS model also come from the LHC and are reviewed in references (Ledroit-Guillon, 2015; Landsberg, 2015). While for small values of couplings

$\tilde{k} = k/\overline{M}_{Pl}$, LHC has largely excluded “natural" values of $M_D < 10$ TeV, for larger couplings $\tilde{k} > 0.2$, the excluded values of M_D are below 4 TeV (Landsberg, 2015).

At high-energy colliders, one of possible processes that enter in higher-dimensional space is the formation of microscopic black holes (BH) (Dimopoulos & Landsberg, 2001; Giddings & Thomas, 2002) with production cross section proportional to the squared Schwarzschild radius, given as

$$R_S = \frac{1}{\sqrt{\pi} M_D} \left[\frac{M_{BH}}{M_D} \left(\frac{8\Gamma(\frac{n+3}{2})}{n+2} \right) \right]^{\frac{1}{n+1}}, \tag{1.2}$$

where M_{BH} is the mass of the black hole. In the simplest production scenario, the cross section is given by an area of a black disk of a radius R_S, i.e. $\sigma \approx \pi R_S^2$ (Dimopoulos & Landsberg, 2001; Giddings & Thomas, 2002). In more complicated production scenarios, e.g. a scenario with the energy loss during the formation of the BH horizon, the cross section is modified from the black disk approximation by a factor of order one.

In the literature, one finds several conventions for the Planck scale M_D. In this analysis we use the definition of reference (Giddings & Thomas, 2002) (M_D^{GT}), which has been also adapted by the Particle Data Group (Particle Data Group Collaboration, 2014) and used by the LHC experiments. The other possible choice is the definition of reference (Dimopoulos & Landsberg, 2001) (M_D^{DL}). There is a trivial relationship between the two conventions (see Appendix A of reference (Giddings & Thomas, 2002)):

$$M_D^{GT} = M_D^{DL} \frac{2\pi}{(16\pi^3)^{\frac{1}{n+2}}}.$$

Thus, for $n = 2$, $M_D^{GT} \approx 1.3 M_D^{DL}$, while for $n = 6$, $M_D^{GT} \approx 2.9 M_D^{DL}$.

We consider BH models with $M_{BH} > M_D$. As BH production is a threshold phenomenon, we search for BHs above certain minimum mass $M_{BH}^{min} \geq M_D$. In the lack of signal, we will express the results of the search as limits on this minimum BH mass. In the semi-classical case (strictly valid for $M_{BH} \gg M_D$), the BH decays ("evaporates" via Hawking radiation) into a large number of energetic objects such as hadrons (jets), leptons, photons, etc. In some cases, significant amount of missing transverse energy may be produced in the process of BH evaporation. Missing transverse energy can result from the production of neutrinos (which constitute 5% of semiclassical BH decay products), W and Z boson decays, heavy-flavor quark decays, gravitons, or noninteracting stable BH remnants. Relative abundance of various particles produced in the process of BH evaporation is expected to follow the number of degrees of freedom per particle in the standard model. About 75% of particles produced are expected to be quarks and gluons, due to large number of color degree of freedoms. As the BH mass approaches M_D, the semi-classical approximation is expected to break down and the BH becomes a quantum object. These quantum black holes (QBH) typically decay before thermalization in a handful of objects, e.g., in two quarks (Calmet & Hsu, 2008; Gingrich, 2010). These decays could also violate baryon and lepton number conservations, allowing to look for QBH in, e.g., $e\mu$ final state. One of the models of semi-classical BH precursors is the string ball model (Dimopoulos & Emparan, 2002), which predicts a formation of a long jagged string excitation, folded into a “ball", which eventually transitions into a true BH, once its mass exceeds the M_D significantly.

Production of black holes has been theorized in both the ADD and RS models. In the latter case (Anchordoqui et al, 2002; Landsberg, 2006; Meade & Randall, 2008) the BH are expected to exhibit more quantum properties as the evaporation time typically is less than is needed for thermalization of the BH. Thus, when dealing with semi-classical BH case, we focus on the ADD model, and only consider RS model when dealing with QBHs.

A number of searches for both semi-classical and quantum BHs have been performed in the LHC Run 1. For an extensive review of these searches, see reference (Landsberg, 2015). Typical limits set on minimum BH mass by these searches is in 6 TeV range. An increased energy of the LHC in Run 2 (13 TeV) should allow this new search to probe much higher BH masses.

In this thesis, first, we study the radiation of the miniature black holes through the thermodynamical process at quantum gravity level. Indeed, in order to understand the hawking radiation mechanism for microscopic black holes as the main part of their decay process, one should take into account thermodynamics in presence of the Generalized Uncertainty Principle (GUP) as one of the potential solution. In this manner, we calculate thermodynamical parameters such as temperature and entropy, for charged microscopic black hole and charged rotating black holes. Then, we describe a search for the BH and set limits on the mass and the production cross section of the BH. We closely follow the original approach pioneered by CMS in Run 1 (CMS Collaboration, 2011; 2012; 2013) (and the corresponding internal analysis notes (CMS Collaboration, 2010; 2011)) and conduct an inclusive search for BH decays in all possible final states, dominated by the multijet ones in the semi-classical BH case and dijet one in the QBH case. This type of analysis is much less sensitive to fine aspects of BH evaporation and the relative abundance of various particles produced, as it considers all type of particles in the final state and uses a single discriminating variable, S_T, defined as a scalar sum of transverse energies of all energetic objects in an event (which we define as jets, electrons, muons, and photons with transverse energies $E_T > 50$ GeV, of which there are N), plus missing transverse energy in the event, if it exceeds the same 50 GeV threshold:

$$S_T = \left(\sum_{i=1}^{N} E_{T,i} \right) + (E_T^{miss} > 50\ \text{GeV}), \tag{1.3}$$

This definition of S_T is robust against variations in the BH evaporation model, and is also sensitive to the cases when there is large missing transverse energy due to enhanced emission of gravitons (superradiance models) or models in which a massive weakly interacting sub-Planckian remnant of a BH is formed at the terminal stage of Hawking evaporation.

The S_T distributions are then considered separately in various inclusive object multiplicity bins (i.e., $N \geq N^{min}$), the background is estimated exclusively from control samples in data, and the observed number of events with S_T values above a certain threshold is compared with the background and signal+background predictions to either establish the production of BHs or set limits on their minimum mass. This approach does not rely on the Monte Carlo (MC) description of the backgrounds; it also has higher sensitivity than exclusive searches in particular final states, e.g. lepton+jets (this type of analysis has been pursued by the ATLAS Collaboration (ATLAS Collaboration, 2013; 2014)). It is also less sensitive to the details of the BH evaporation and model parameters. (Recently, the inclusive CMS-style BH search was also published by the ATLAS Collaboration based on the complete Run 1 (8 TeV) data set (ATLAS Collaboration, 2015) and on first Run 2 (13 TeV) data (ATLAS Collaboration, 2015).)

The main challenge of the search is to describe the inclusive multijet background in a robust way, as the BH signal corresponds to a broad enhancement in the S_T distribution at the high end, rather than a narrow peak. Since the BH signal is expected to correspond to high multiplicity of final-state particles, one has to reliably describe the background for large jet multiplicities, which is quite challenging theoretically, as higher-order calculations that fully describe multijet production simply do not exist. Thus, one can not rely on the MC simulations to reproduce the S_T spectrum correctly.

To overcome this problem, a novel method of predicting the QCD background directly from collision data has been developed for the Run 1 analysis (CMS Collaboration, 2011; 2012; 2013). It has been found empirically, first via simulation-based studies, and then from the analysis of data at low jet multiplicities that the shape of the S_T distribution for the dominant QCD multijet background does not depend on the multiplicity of the final state, above a certain turn-on threshold. This observation, motivated by the way parton shower is developed via nearly collinear emission, which conserves S_T, allows one to predict S_T spectrum of a multijet final state using low-multiplicity QCD events, e.g. dijets or three-jet events. This provides a powerful method of predicting the dominant background for BH production by taking the S_T shape from dijet events, for which the signal contamination is expected to be negligible, and normalizing it to the observed spectrum at high multiplicities at the low end of the S_T distribution, where signal contamination is negligible even for large multiplicities of the final-state objects. The method has been also used for other CMS searches, e.g. search for stealth SUSY (CMS Collaboration, 2015) and search multijet resonances (CMS Collaboration, 2013). Since the S_T spectrum of the QCD background is predicted to change in proportion to the logarithm of the center-of-mass energy, we expect the same strategy used in the 8 TeV analysis to work essentially unmodified for the 13 TeV analysis. The objectives of this research are:

I) To explore one of the possible solutions to the hierarchy problem

II) To search for the results of black hole production resulting in production of energetic multi-particle final states in proton-proton collisions at $\sqrt{s} = 13$ TeV

This research and analysis will serve as basis for future study at the LHC in pp collisions at a center-of-mass energy higher than 13 TeV.

CHAPTER 2: THEORY

2.1 Standard Model

The theory that describes the role of the fundamental particles and interactions between them known as the Standard Model (SM) of particle physics which is the result of the theories and discoveries of thousands of physicists over the past century. The fundamental structure of matter is composed of twelve basic building blocks called fundamental particles, governed by four fundamental forces such as the electromagnetic, the weak, the strong, and the gravitational force. Our understanding of how these particles and forces excluding gravitational forces developed in the early 1970's which has precisely predicted a wide variety of phenomena, successfully explained experimental results and has become established as a well-tested physics theory. Based on the SM there are two type of the particles, half integer spin particles which are known as the fundamental fermions including leptons, quarks and their antiparticles, and integer spin particles known as bosons (gauge bosons and the Higgs boson).

There are six quarks in three generations, up (u) and down (d) in the first generation, strange (s) and charm (c) in the second generation and bottom (b) and top (t) in the third generation. Each quark can have three colours, red (r), green (g) and blue (b), but no free colour charge exists in nature at long distances. Similarly, There are six leptons classified in three generations. The electron (e) and the electron neutrino (ν_e) are in the first generation, the muon (μ) and the muon neutrino (ν_μ) are in the second generation and the tau (τ) and the tau neutrino (ν_τ) make the third generation.

However, the fundamental interactions in nature have mediators including a photon for the electromagnetic force, two W's and one Z boson for the weak force, eight gluons for the strong forces and maybe graviton for gravity. The gluons do not exist as isolated particle due to carry colour and anti-colour but they can exist within hadrons or in colourless combinations. The SM model is including three main symmetries: i) symmetry with the associated gauge boson field, B which is known as hypercharge symmetry, $U(1)$, ii) $SU(2)$ isospin symmetry which couples only to left-handed fermions, and iii) colour symmetry, $SU(3)$, which has three conserved colour charges. Here, we highlight, the first two symmetries are described by the electroweak theory and the third one by quantum chromodynamics (QCD). In the electroweak theory, there are three associated gauge fields such as W_1, W_2, and W_3 which during the electroweak symmetry breaking the W_1 and W_2 mix to give $W^{\pm}$ while the W_3 and B fields mix to give the photon and Z^0 bosons.

In this manner, quantum electrodynamics (QED) which is an abelian gauge theory, describes the interactions between spin half charged particles by the exchange of a field quantum, the photon, while QCD which is non-abelian gauge theory, describes the interaction of quarks via gluons. Two important features of QCD are confinement and asymptotic freedom. Based on the confinement, the quarks generally are confined in hadrons and an infinite amount of energy is required to separate a quark to infinity from its hadron. In this way, the strength of strong coupling is small at very small distance such that quarks and gluons interact weakly and behave as free particles according to asymptotic freedom.

The SM is well developed during the past decades, however, there are some fundamental questions in high energy physics which has no answer in the SM. Hence, fundamental theories beyond the SM model are proposed to answer these questions such as supersymmetry, extra dimensions, etc.

2.2 Black Holes at the LHC

The possibility of production of black holes (Argyres et al., 1998; Emparan etal., 2000) at particle colliders such as the Large Hadronic Collider (LHC) is one of the most exciting consequence of TeV-scale quantum gravity (Arkani-Hamed etal., 1998). Various theories of quantum gravity support the idea that near the Planck scale; the standard Heisenberg uncertainty principle should be reformulated by the so-called Generalized Uncertainty Principle (GUP) (Veneziano, 1986; Kempf etal., 1995; Kempf & Mangno, 1997). In particular, TeV-scale black hole physics (Meissner, 2004), string theory, (Amati, 1989) and loop quantum gravity indicate the existence of a minimum observable length and black hole Gedanken experiments support the idea in a fascinating manner (Scardigli, 1999). On the other hand, a test particle's momentum cannot be arbitrarily imprecise and there is an upper bound for momentum fluctuation based on the context of Doubly Special Relativity (DSR) (Ali et al., 2011; Das & Vagenas, 2008). Therefore, there is a maximal particle momentum. We study the effects of natural cutoffs encoded in GUPs on the thermodynamics of micro black holes with conserved electric charge during their formation and decay process (Calmet etal., 2008). Here, we consider a GUP that admits just a minimal length and maximal momentum which we call GUPI. Secondly, we use a more general GUP that admits a minimal length, minimal momentum, and maximal momentum, which we call, GUPII. We study thermodynamics of charged TeV-scale black holes with extra dimensions in Arkani-hamed, Dimopoulos, and Dvali (ADD) model (Arkani-Hamed et al., 1998) in the context of these GUPs as the most general static black hole and also charged rotating TeV-scale black hole as the most general micro black hole. The corrections to micro black hole thermodynamic parameters such as Hawking temperature, Bekenstein-Hawking entropy, and radiation rate may have important consequences on TeV-scale black hole production at particle colliders.

2.3 Generalized Uncertainty Principle (GUP)

2.3.1 Minimal Length and Maximal Momentum (GUPI)

Most of the quantum gravity approach, indicate the existence of a minimal measurable length of the order of the Planck length, $l_{pl} \sim 10^{-35} m$ (Maggiore, 1993). The existence of a minimal measurable length modifies the Heisenberg uncertainty principle to the so-called Generalized Uncertainty Principle (GUP). The GUP framework is essentially restricted on the measurement precision of the particle's position, so that as the minimal position uncertainty could not be made arbitrarily small towards zero (Kempf et al., 1995). On the other hand, Doubly Special Relativity (DSR) theories (Camelia, 2002) has considered that existence of a minimal measurable length would restrict a test particle's momentum to take any arbitrary values and therefore there exist an upper bound for momentum fluctuation (Magueijo & Smolin, 2003). It has been shown that there is a maximal particle's momentum due to fundamental structure of spacetime at the Planck scale. Based on this framework, the GUP that predicts both a minimal length and a maximal momentum can be written as follows (Ali et al., 2011; Das & Vagenas, 2008)

$$\Delta x \Delta p \geq \frac{\hbar}{2}\left(1 - 2\alpha\langle p\rangle + 4\alpha^2\langle p^2\rangle\right) \tag{2.1}$$

or

$$\Delta x \Delta p \geq \frac{\hbar}{2}\left(1 - \alpha\langle \Delta p\rangle + 2\alpha^2\langle \Delta p\rangle^2\right) \tag{2.2}$$

The relation (2.1) and/or (2.2) can lead us to the following commutator relation:

$$[x, p] = i\hbar\left(1 - \alpha p + 2\alpha^2 p^2\right) \tag{2.3}$$

where α is the GUP positive constant in the presence of both minimal length and maximal momentum. In the extra dimensional scenario based on the ADD model, the GUP can be written as follows (Nozari, 2006):

$$\Delta x_i \Delta p_i \geq \frac{\hbar}{2}\left(1 - \alpha L_{pl}(\Delta p_i) + 2\alpha^2 L_{pl}^2(\Delta p_i)^2\right) \tag{2.4}$$

where the Planck length in a model of the universe with large extra dimensions is defined as $L_{pl} = (\frac{\hbar G_d}{c^3})^{\frac{1}{d-2}}$. Here, G_d is the gravitational constant in d dimensional spacetime, which is given by $G_d = G_4 L^{d-4}$ in the ADD scenario, where L is the size of the extra dimensions. Here, we adopt the units $G = c = \hbar = 1$. By saturating the inequality (2.4), a simple calculation gives,

$$\Delta p_i = (\frac{\alpha L_{pl} + 2\Delta x_i}{4\alpha^2 L_{pl}^2})\left(1 \pm \sqrt{1 - \frac{8\alpha^2 L_{pl}^2}{(\alpha L_{pl} + 2\Delta x_i)^2}}\right) \tag{2.5}$$

So, the minimal position uncertainty has the value

$$\Delta x_i \geq \Delta x_{\min} = \alpha L_{pl}\left(\frac{2\sqrt{2} - 1}{2}\right) \tag{2.6}$$

This is a new minimal observable length scale on the order of the Planck length.

2.3.2 Minimal Length, Minimal Momentum, and Maximal Momentum (GUPII)

In this section, we tack into account a more generalized uncertainty principle that admits a minimal length, a minimal momentum, and maximal momentum as well. As discussed in previous section, the minimal length comes from the finite resolution of spacetime points in the Planck scale, as a string cannot probe distances smaller than its length. In doubly special relativity theories, we consider the Planck energy (Planck momentum) as an additional invariant rather than the velocity of light. Therefore, the existence of a maximal momentum is in agreement with various theories of quantum gravity. The existence of a minimal momentum was developed by generalizing the Heisenberg commutation relation (Kempf, 1997). In this case, there is no rotation of a plane wave on a general curved spacetime (Hinrichsen & Kempf, 1996; Zarei and Mirza, 2009), for large distances where the curvature become important. In fact, the precision with which the corresponding momentum can be described and it can be expressed as a nonzero minimal uncertainty. For instance, one can obtain the harmonic oscillator energy spectrum in the GUP framework which implies maximal momentum uncertainty and minimal uncertainties in both position and momentum. It is known that quantum mechanical energy of its ground state, is nonzero and has a minimal value. In this case, the smallest uncertainty in momentum is not zero and can be considered nontrivially as the minimal momentum. Based on these arguments, as a consequence of small correction to the canonical commutation relations, one infers the following expression

$$\Delta x \Delta p \geq \frac{\hbar}{2}\left[1 - 2\alpha(\Delta p) + 4\alpha^2(\Delta p)^2 + 4\beta^2(\Delta x)^2\right] \tag{2.7}$$

which in extra dimension can be written as follows

$$\Delta x_i \Delta p_i \geq \frac{\hbar}{2}\left[1 - 2\alpha L_{pl}(\Delta p_i) + 4\alpha^2 L_{pl}^2(\Delta p_i)^2 + 4\beta^2 L_{pl}^2(\Delta x_i)^2\right] \tag{2.8}$$

Here, α and β are dimensionless, positive coefficients, and independent of Δx and Δp but in general they may depend on the expectation value of x and p. The inequality (2.8) leads us to a nonzero minimal uncertainty in both position and momentum. It is easy to show

$$\Delta x_i \geq \Delta x_{\min} = \frac{\hbar\alpha L_{pl}\left(1 - 2\sqrt{1 - 12\alpha^2\beta^2 L_{pl}^4}\right)}{16\alpha^2\beta^2 L_{pl}^4 - 1} \tag{2.9}$$

$$\Delta p_i \geq \Delta p_{\min} = \frac{\hbar\beta L_{pl}\left(1 + 2\sqrt{1 - 12\alpha^2\beta^2 L_{pl}^4}\right)}{16\alpha^2\beta^2 L_{pl}^4 - 1} \tag{2.10}$$

which these relations represent the existence of the minimal length and minimal momentum in presence of the extra dimensions based on the ADD model. Based on the generalized Heisenberg algebra, we suppose that operators of position and momentum obey the following commutation relation

$$[x, p] = i\hbar \left(1 - 2\alpha p + 4\alpha^2 p^2 + 4\beta^2 x^2\right) \tag{2.11}$$

In this case, on the boundary of the allowed region, the curve is given by

$$\Delta p_i = \left(\frac{\alpha L_{pl} + \Delta x_i}{4\alpha^2 L_{pl}^2}\right) \times \left(1 \pm \sqrt{1 - \frac{(4\alpha^2 L_{pl}^2)(1 + 4\beta^2 L_{pl}^2 (\Delta x_i)^2)}{(\alpha L_{pl} + \Delta x_i)^2}}\right) \tag{2.12}$$

In what follows, we use these two general forms of the GUP(I and II) as our primary input and construct a perturbational calculations to find thermodynamical properties of charged TeV-scale black hole and its quantum gravitational corrections. Here, we draw attention that since generalized Heisenberg uncertainty principle is a model independent concept (Hossenfelder, 2003), the obtained results are consistent with any fundamental quantum gravity theory.

2.4 Charged Micro Black Hole Thermodynamics

2.4.1 Hawking Temperature

In order to characterize black hole, there are only three quantities namely, mass, M, electric charge, Q, and angular momentum, J (Frolov et al., 2005; Padmanabhan, 2005). In this manner, a charged black hole is the one which carries electric charge and the Schwarzschild solution is no longer valid. The Reissner-Nordström geometry describes the empty space surrounding a charged black hole. On the other hand, the idea of the Large Extra Dimensions (LEDs) might allow studying interactions at Trans-Planckian energies in particle colliders such as LHC and the ADD model (Arkani-Hamed et al., 1998) used new d dimensional large space-like without curvature. Therefore, a natural candidate for TeV-scale charged black holes of higher dimensional is that of the Reissner-Nordström

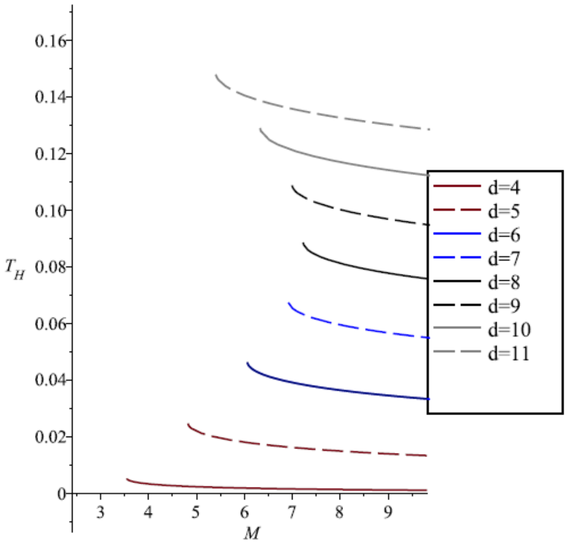

Figure 2.1: Hawking Temperature with respect to the mass in terms of GUPI

d-dimensional solution of the Einstein field equation (Myers & Perry, 1986) given by

$$ds^2 = f(r)c^2dt^2 - f^{-1}(r)dr^2 - r^2d\Omega^2_{d-2} = g_{\mu\nu}dx^{\mu}dx^{\nu} \tag{2.13}$$

where Ω_{d-2} is the metric of the unit S^{d-2} as $\Omega_{d-2} = \frac{2\pi^{\frac{(d-1)}{2}}}{\Gamma(\frac{d-1}{2})}$, and

$$f(r) = 1 - \frac{r_s}{r^{(d-3)}} + \frac{r_Q^2}{r^{2(d-3)}} \tag{2.14}$$

Here, the parameter r_s is related to the mass M of the black hole as

$$r_s = \frac{8\pi G_d}{(d-2)\Omega_{d-2}}M \tag{2.15}$$

where $G_d = G_4 L^{d-4}$ and the electric charge of the black hole is given by

$$Q^2 = \frac{(d-2)(d-3)}{8\pi G_d}r_Q^2 \tag{2.16}$$

where the outer horizon is situated at

$$r_h^{d-3} = r_s + \left(r_s^2 - r_Q^2\right)^{1/2} \tag{2.17}$$

In order to apply the original Bekenstein-Hawking formalism to the d-dimensional charged black holes, let us start with the first law of the black hole mechanics (Bekenstein, 1973; Bardeen et al., 1973),

$$dM = \frac{k}{8\pi} dA + \sum_i Y_i dy_i \tag{2.18}$$

where $\sum_i Y_i dy_i$ are related to the work done on the black hole by an external agent. However, since Hawking radiation was proposed, it has been endowed with thermodynamic meaning, i.e.

$$dM = TdS + \sum_i Y_i dy_i \tag{2.19}$$

The first law is generalized to the electrically charged black holes as (Wald, 1984)

$$dM = TdS + \mu dQ \tag{2.20}$$

where μ plays the role of a chemical potential and Q counts the number of charges. In general, the entropy of the black hole is assumed to be a function of its area, S=S(A) (Bekenstein, 1973). Following the definition of thermodynamics, from (2.19) and (2.20), the temperature is expressed as

$$T = \left(\frac{\partial M}{\partial S}\right)_Q = \frac{dA}{dS} \times \left(\frac{\partial M}{\partial A}\right)_Q = \frac{dA}{dS} \times \frac{k}{8\pi} \tag{2.21}$$

where the variable Q is fixed.

In this case, considering the black hole as d-dimensional cube, the position uncertainty should not be greater than a specific scale which is identified by twice radius of the horizon for a static spherically symmetric black hole such as Reissner-Nordström (Adler et al., 2001). Therefore, using GUPI leads to

$$2r_{h+} \geq \Delta x_i \geq \frac{\hbar}{2}\left[\frac{1}{\Delta p_i} - \alpha L_{pl} + 2\alpha^2 L_{pl}^2 (\Delta p_i)\right] \tag{2.22}$$

which imposes constraint on the momentum uncertainty.

Following a heuristic argument (Adler et al., 2001), based on the usual Heisenberg uncertainty principle, uncertainty in the energy of the Hawking particles is $\Delta E \approx c\Delta p$. In this case, one deduces the following Equation for the Hawking temperature of the black hole based on the LED scenario as

$$T_H \approx \frac{(d-3)\,\Delta p_i}{4\pi} \tag{2.23}$$

where, the constant, $\frac{(d-3)}{4\pi}$, is a calibration factor in d-dimensional spacetime. In this manner, the modified Hawking temperature of the black hole based on the GUPI becomes

$$T_H^{GUPI} = \frac{(d-3)}{16\pi\alpha^2 L^2{}_{pl}} \times \left[(4r_{h+} + \alpha L_{pl}) - ((4r_{h+} + \alpha L_{pl})^2 - 8\alpha^2 L_{pl}^2)^{1/2}\right] \tag{2.24}$$

Based on the Equation (2.24), GUPI gives rise to the existence of a minimal mass of the charged micro black hole given by

$$M_{\min}^{GUPI} = \frac{(d-2)\,\Omega_{d-2}}{16\pi\left[\left(\frac{2\sqrt{2}-1}{4}\right)\alpha L_{pl}\right]^{d-3}}\left(\left[\left(\frac{2\sqrt{2}-1}{4}\right)\alpha L_{pl}\right]^{2d-6} + \frac{8\pi Q^2}{(d-2)\,(d-3)}\right) \tag{2.25}$$

The expression (2.25) shows that the Hawking temperature of the black hole is only defined for $M \geq M_{\min}$. In this case, the temperature of the black hole with minimum mass defined

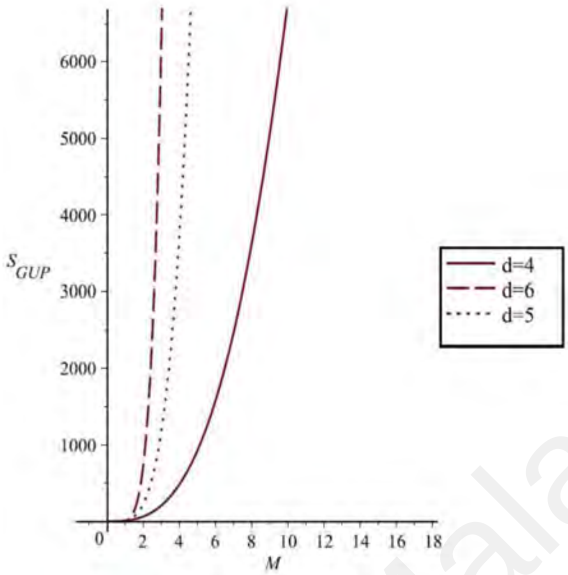

Figure 2.2: Hawking Temperature with respect to the mass in terms of GUPII

by (2.25) reaches a maximum value and reads

$$T_{\max}^{GUPI} = \frac{(d-3)}{4\pi\alpha^2 L_{pl}} M_p{}^{\frac{1}{(d-3)}} \left(\frac{8\pi M_{\min}^{GUPI}}{(d-2)\Omega_{d-2}}\right)^{\frac{1}{d-3}} \times \left(1 + \sqrt{1 - \frac{(d-2)\Omega_{d-2}^2 Q^2}{(d-3)8\pi M_{\min}^{GUPI}}}\right)^{\frac{1}{d-3}} + \frac{(d-3)}{16\pi\alpha} \tag{2.26}$$

In the standard picture of the micro black hole, the evaporation process can be divided into three characteristic stages (Giddings & Thomas, 2002) as i)Balding phase which is the initial stage that black hole emits mainly gravitational radiations and sheds all the quantum numbers and multiple momenta apart from those determined by its mass, charge and angular momentum, ii)Evaporation phase which the black hole starts losing its angular momentum through the emission of the Hawking radiation, and iii)Planck phase as the final stage mainly the black hole mass approaches the true Planck scale as the black hole remnant with mass M_{min}. Within these stages, the charged TeV-scale black hole temperature increases through its evaporation process and the radius of the event horizon decrease in the framework of GUPI. This phase is also known as the Hawking phase. In the last stage, the temperature reaches to a finite temperature which is calculated by Equation (2.26) (see Figure 2.1 and Figure 2.2). However, as Figure 2.3 shows, when electric charge, Q, increases, the minimum mass and its order of magnitude increase and the temperature peak displaces to the lower temperature.

We also consider a more general uncertainty principle that admits a minimal length, a minimal momentum, and a maximal momentum, GUPII, to compute the corrected Hawking temperature of the charged black hole. Based on the Equations (2.11), (2.12), and (2.23), in the same manner as GUPI, we obtain

$$T_H^{GUPII} = \frac{(d-3)(2r_{h+} + \alpha L_{pl})}{16\pi\alpha^2 L_{pl}^2}\left[1 - \sqrt{1 - \frac{4\alpha^2 L_{pl}^2(1 + 16L_{pl}^2\beta^2 r_{h+}^2)}{(2r_{h+} + \alpha L_{pl})^2}}\right]. \tag{2.27}$$

Therefore, the generalized uncertainty principle that admits a minimal length, a minimal momentum, and a maximal momentum, gives rise to the existence of a minimal mass of the charged black hole as

$$\begin{aligned} M_{\min}^{GUPII} = \tfrac{(d-2)\Omega}{16\pi}\Bigg(\Bigg(&\tfrac{\left(1+2\sqrt{1-12\beta^2\alpha^2L_{pl}^4}\right)L_{pl}\alpha}{32\beta^2\alpha^2L_{pl}^4-2}\Bigg)^{2d-6} + \tfrac{8\pi Q^2}{(d-2)(d-3)}\Bigg) \\ &\times\Bigg(\Bigg(\tfrac{\left(1+2\sqrt{1-12\beta^2\alpha^2L_{pl}^4}\right)L_{pl}\alpha}{32\beta^2\alpha^2L_{pl}^4-2}\Bigg)^{d-3}\Bigg)^{-1} \end{aligned} \tag{2.28}$$

Here, there is restriction on the range of the parameters α and β. The Equations (2.27) and (2.28) shows that α and β cannot take arbitrary value. Therefore, α and β are related parameters which essentially depend on the aspects of the candidates for quantum gravity proposal. The results show that in the large extra dimension scenario, the temperature of the charged black hole increases and leads to faster decay of the black hole. It is evident that in the large extra dimension scenario, the black hole remnant has mass more than its four

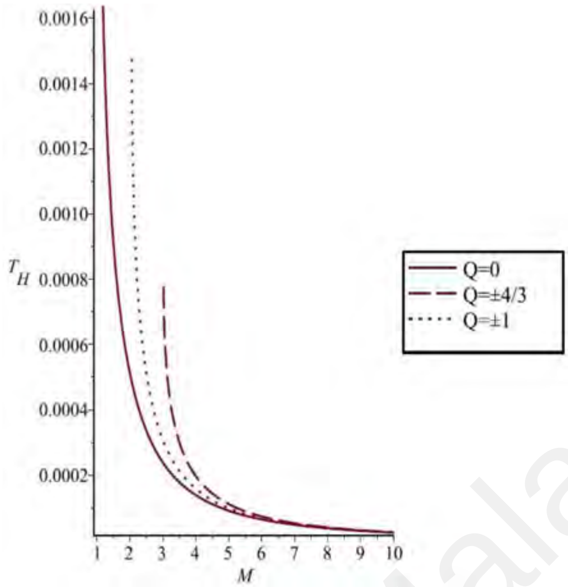

Figure 2.3: Hawking Temperature for different amount of Charges

dimensional counterpart. Therefore, in the generalized uncertainty principle framework, the quantum black holes are hotter, shorter lived and evaporate less than classical black holes.

2.4.2 Entropy and Radiation

It is well known that the Bekenstein-Hawking entropy is proportional to its horizon area which behaves in every way like a thermodynamic entropy (Hawking, 1971; Bekenstein, 1974; Strominger & Vafa, 1996; Carlip, 1999; Solodukhin, 1999). In order to find concrete form of the entropy of the charged micro black hole in presence of generalized uncertainty principle, we consider a particle captured by the black hole. Therefore, the loss of the information results in the increase of the entropy of the black hole. We obtain

$$\Delta S \simeq \frac{dS}{dA}\Delta A \tag{2.29}$$

In this case, the inequality (2.4) can be rewritten in the Heisenberg uncertainty principle format, $\Delta x_i \Delta p_i \geq \hbar'$ where $\hbar'$ may be regarded as an effective Planck constant (Xiang & Wen, 2009). Thus, the increase in area satisfies

$$\Delta A \geq \gamma \hbar' \tag{2.30}$$

where γ is a calibration factor.

The information of one bit is lost when a particle vanishes and the black hole specify increasing the entropy by $(\Delta S)_{\min} = \ln 2$. On the other hand, the lower bound of (2.29) gives the minimum increase in the horizon area. We then obtain

$$\frac{dA}{dS} \simeq \frac{(\Delta A)_{\min}}{(\Delta S)_{\min}} = \frac{\gamma \hbar'}{\ln 2} \tag{2.31}$$

By substituting (2.31) into Equation (2.21) we get

$$T = \frac{k}{8\pi} \times \frac{\gamma \hbar'}{\ln 2} \tag{2.32}$$

In this manner, the standard result, $T = \frac{k}{2\pi}$, should be reproduced as $\alpha \to 0$ which yields the calibration factor $\gamma = 4 \ln 2$. In this case, based on Equation (2.31) the black hole entropy can be expressed as

$$S \simeq \int \frac{(\Delta S)_{\min}}{(\Delta A)_{\min}} dA = \frac{1}{4} \int \frac{dA}{\hbar'} \tag{2.33}$$

Since, we are dealing with the Reissner-Nordström black hole of fixed charge, based on the Equation (2.19), it is easy to show

$$S \simeq 2\pi \int \frac{dM}{k\hbar'} \tag{2.34}$$

In order to obtain the modified entropy based on the GUPI, one should perform integration on S which is physically reasonable to set $M_{\min}$ as lower limit of integration. Based on these arguments, and by substitution of Equations (2.24) and (2.32) into (2.34), one can obtain

$$S^{GUPI} = \frac{16\pi\alpha^2 L_{pl}^2}{d-3} \int_{M_{\min}}^{M} dM \times \left[\left(4r_{h+} + \alpha L_{pl}\right) \left(1 - \sqrt{1 - \frac{8\alpha^2 L_{pl}^2}{(4r_{h+} + \alpha L_{pl})^2}} \right) \right]^{-1} \tag{2.35}$$

and similarly the entropy for the GUPII given

$$S^{GUPII} = \frac{16\pi\alpha^2 L_{pl}^2}{d-3} \int_{M_{\min}}^{M} dM \times \left[\left(2r_{h+} + \alpha L_{pl}\right) \left(1 - \sqrt{1 - \frac{4\alpha^2 L_{pl}^2 (1 + 16 L_{pl}^2 \beta^2 r_{h+}^2)}{(2r_{h+} + \alpha L_{pl})^2}} \right) \right]^{-1} \tag{2.36}$$

The integral (2.36) can be solved numerically. One can use the semi classical entropy to measure the semi classical approximation validity. Therefore, the higher dimensional charged black hole remnants have less classical feature compared to their four dimensional counterpart.

We now proceed to obtain the relation between emission rate of the charged TeV-scale black hole radiation and spacetime dimensions. It was shown (Emparan et al., 2000) in d-dimensions, that the radiated energy by a black body of temperature T and surface area A is given by

$$\frac{dE_d^{GUP}}{dt} = \sigma_d A T_d^{GUP} \tag{2.37}$$

which is based on the standard calculations of the statistical mechanics in higher dimensions, σ_d is the d-dimensional Stefan-Boltzman constant,

$$\sigma_d = \frac{\Omega_{d-3}}{(2\pi)^{d-1}(d-2)} \int_0^\infty \frac{Z^{d-1}}{e^z - 1} dz = \frac{\Omega_{d-3}}{(2\pi)^{d-1}(d-2)} \Gamma(d)\zeta(d) \tag{2.38}$$

with $\zeta(d)$ denoting the Riemann zeta function. Here, the outer event horizon is located at $r = r_{h+}$, and the area of the event horizon is $A_d = r_{h+}^{d-2}\Omega_{d-2}$. Therefore, using Equations (2.24) and (2.27) as the modified Hawking temperature in the framework of the GUPI, and GUPII, we obtain

$$\begin{aligned} \frac{dE_d^{GUPI}}{dt} &= \frac{(4r_{h+}+\alpha L_{pl})\Omega_{d-3}\Omega_{d-2}(d-3)}{16\pi\alpha^2 L_{pl}^2 (2\pi)^{d-1}(d-2)} \Gamma(d)\zeta(d) r_{h+}^{d-2} \\ &\times \left(1 - \sqrt{1 - \frac{8\alpha^2 L_{pl}^2}{(4r_{h+}+\alpha L_{pl})^2}}\right) \end{aligned} \tag{2.39}$$

and

$$\begin{aligned} \frac{dE_d^{GUPII}}{dt} &= \frac{(2r_{h+}+\alpha L_{pl})\Omega_{d-3}\Omega_{d-2}(d-3)}{16\pi\alpha^2 L_{pl}^2 (2\pi)^{d-1}(d-2)} \Gamma(d)\zeta(d) r_{h+}^{d-2} \\ &\times \left(1 - \sqrt{1 - \frac{4\alpha^2 L_{pl}^2 (1+16\beta^2 L_{pl}^2 r_{h+}^2}{(2r_{h+}+\alpha L_{pl})^2}}\right) \end{aligned} \tag{2.40}$$

These are complicated relation. Here, we highlight that the σ_d changes very little with respect to the dimension. It was shown that most of the radiation goes into purely four dimensional fields, and the evaporation of the small black hole does not proceed as in a purely four dimensional theory (Emparan et al., 2000). In this case, the fact confirms that the rate of the energy which is radiated by black body with radius R and temperature T is roughly independent of the dimensions even though higher dimensional spacetime have infinitely many more modes due to the excitations in the extra dimensions. Here, we consider the case of $d = 4$, $d = 7$, and $d = 10$. Since $\sigma_4 \simeq 0.082$, $\sigma_7 \simeq 0.062$ and

$\sigma_{10} \simeq 0.097$, one can compute numerically the following ratios,

$$\frac{(\frac{dE_4^{GUPI}}{dt})}{(\frac{dE_7^{GUPI}}{dt})} \simeq 9.89, \frac{(\frac{dE_4^{GUPII}}{dt})}{(\frac{dE_7^{GUPII}}{dt})} \simeq 9.89, \frac{(\frac{dE_4^{GUPI}}{dt})}{(\frac{dE_{10}^{GUPI}}{dt})} \simeq 10.84, \frac{(\frac{dE_4^{GUPII}}{dt})}{(\frac{dE_{10}^{GUPII}}{dt})} \simeq 10.84 \qquad (2.41)$$

and

$$\left.\frac{(\frac{dE_4^{GUPI}}{dt})}{(\frac{dE_7^{GUPI}}{dt})}\right|_{Q=0} \simeq 8.76, \left.\frac{(\frac{dE_4^{GUPII}}{dt})}{(\frac{dE_7^{GUPII}}{dt})}\right|_{Q=0} \simeq 8.76, \left.\frac{(\frac{dE_4^{GUPI}}{dt})}{(\frac{dE_{10}^{GUPI}}{dt})}\right|_{Q=0} \simeq 9.97, \left.\frac{(\frac{dE_4^{GUPII}}{dt})}{(\frac{dE_{10}^{GUPII}}{dt})}\right|_{Q=0} \simeq 9.97 \qquad (2.42)$$

The results show evidently that the charged TeV-scale black holes radiate mainly into the 4-dimensional brane independent of the type of the GUP. In fact, the charged TeV-scale black hole emits radiation both in the bulk and into the brane and the electric charge increases the radiation rate of the micro black hole into the brane. We use the radius of the outer horizon to calculate the area of the black body emitter in Equations (2.41) and (2.42). However, in the geometric optics approximation, the black hole acts as a perfect absorber of a slightly larger radius. Therefore, there is a critical radius $r_c = (\frac{3\sqrt{3}}{2})r_0 \simeq 2.6r_0$ for a Schwarzschild black hole, in four dimensions for null geodesics, where r_0 is the event horizon radius. Detailed calculation have shown (Sanchez, 1978) that the total energy radiated is better approximated by assuming the area given by r_c rather than r_0. Based on this argument, we draw attention that some corrections to Equations (2.39) and (2.40) should be considered as Equation (2.37) is related to the area.

In this case, critical radius of the black hole as an absorber is given by (Emparan et al. 2000)

$$r_c = (\frac{d-1}{2})^{\frac{1}{d-3}} \sqrt{\frac{d-1}{d-3}} r_{h+} \qquad (2.43)$$

Based on the assumptions of the theory of large extra dimensions, gravitation and possibly scalar fields, are the only types of the fields allowed to be emitted in the bulk during the

Hawking evaporation phase. The emission on the brane can take the form of the fermions, gauge bosons, and scalar Higgs from the perspective of the brane observer. In this case, the radiation into the brane may lead to the experimental detection of the Hawking radiation and thus of the production of the TeV-scale black hole remnants. Finally, in the next section, we discuss the remnants and some charge effects on the micro black hole thermodynamics.

2.5 Thermodynamics of charged rotating micro black hole

Now, we would calculate the thermodynamical properties of charged rotating micro black hole, using the generalized uncertainty principle based on the Yang-Mills black hole model. In this case, the Kerr-Newman geometry describes the empty space surrounding a charged rotating black hole. Based on the extra dimensions scenario and the ADD model, a natural candidate for the TeV-scale charged rotating black hole is that of a higher dimensional Kerr-Newman solution of the Einstein field equation (Ghosh & Papnoi, 2014)

$$\begin{aligned}
&ds^2 = \left(\tfrac{\Delta - a^2 sin^2\theta}{\Sigma}\right) dt^2 - \tfrac{\Sigma}{\Delta} dr^2 + 2a \\
&\times \left[1 - \left(\tfrac{\Delta - a^2 sin^2\theta}{\Sigma}\right)\right] dt d\varphi - \sum d\theta^2 - \\
&\left[\sum + a^2 sin^2\theta \left(2 - \tfrac{\Delta - a^2 sin^2\theta}{\Sigma}\right)\right] \times sin^2\theta d\varphi^2 - r^2 cos^2\theta d\Omega^2_{d-4}
\end{aligned} \tag{2.44}$$

where Equation (2.44) is in Boyer-Lindquist coordinates. Here,

$$\begin{aligned}
&\Delta = r^2 + a^2 - \tfrac{\mu}{r^{d-5}} - Q^2 \\
&\sum = r^2 + a^2 cos^2\theta
\end{aligned} \tag{2.45}$$

the parameters μ and a are respectively related to the mass (M) and the angular momentum (J) of the black hole via the following relations,

$$\begin{aligned}
&M = \tfrac{(d-2)}{16\pi} A_{d-2}\mu \\
&J = \tfrac{1}{8\pi} A_{d-2}\mu a
\end{aligned} \tag{2.46}$$

and,

$$\frac{M}{J} = \frac{(d-2)}{2a} \tag{2.47}$$

Here, A_{d-2} is the area of a unit (d-2) sphere, which is given by

$$\begin{aligned} A_{d-2} &= \int_0^{2\pi} d\varphi \int_0^{\pi} sin\theta cos^{d-4}\theta d\theta \\ &\times \prod_{i=3}^{d-4} \int_0^{\pi} sin^{(d-4)-i}\theta_i d\theta_i = \frac{2\pi^{\frac{(d-1)}{2}}}{\Gamma\left(\frac{d-1}{2}\right)} \end{aligned} \tag{2.48}$$

We would like to draw attention to the fact that Q is related to Q' by $Q^2 = \frac{N}{N-2}Q'^2$, where Q' is a Yang-Mill gauge charge (Yang & Mills, 1954) and for a vanishing $Q = 0$, one recovers the Myers-Perry black hole solution discussed in (Myers & Perry, 1986). In this case, there are regular inner and outer event horizons, $r_{\pm}$, which we obtain as a solution of Equation (2.45)

$$r^{d-3} + \left[a^2 - Q^2\right] r^{d-5} - \mu = 0 \tag{2.49}$$

In fact, similar to the Kerr solutions, in our case the metric has two types of the horizon-like hypersurface: a stationary limit surface and an event horizon. While the surface area of the event horizon has been related to the entropy of a black hole (Bekenstein, 1973), that of the stationary limit surface has not been given a physical interpretation. On the other hand, when we are dealing with a charged rotating black hole, the event horizon shrinks, and the inner one appears. Particularly, the thermodynamics associated with the outer event horizon of the black hole is related to the fundamental process of Hawking radiation (Wu, 2005). By modeling the black hole as a d-dimensional cube of size equal to its event horizon radius, r_+, the position uncertainty, δx, of the Hawking particle at the emission can be chosen as its Compton wavelength which is proportional to the inverse of the Hawking temperature (Medved & Vagenas, 2004; Nozari & Sefidgar, 2007). The position uncertainty should then not be greater than a specific scale which is defined as follows (Adler at al., 2001; Xiang & Wen, 2009)

$$2\zeta \geq \Delta x_i \tag{2.50}$$

where, this imposes constraint on the momentum uncertainty and $\zeta_d = \sqrt{r_{+_d}^2 + a^2}$ where r_{+_d} is the event horizon radius in d-dimensional space-time. In semiclassical framework, the Hawking temperature of black hole is proportional to the surface gravity which for Kerr-Newman black hole in d-dimensional space time is given by (Ghosh & Papnoi, 2014)

$$T_H^d = \frac{(d-5)\left(r_+^2 + a^2\right) + 2r_+^2 - (d-3)\,Q^2}{4\pi r_+ \left(r_+^2 + a^2\right)} \tag{2.51}$$

where Planck constant reveals the quantum nature of black hole radiation. In the Bekenstein's original work (Bekenstein, 1973), Heisenberg's uncertainty principle is crucial to the linear relation between Hawking temperature and surface gravity. In this manner, GUP changes the semiclassical framework to a certain context, and the semiclassical black hole temperature (2.51) should suffer a modification. Based on heuristic argument and Equation (2.23) the modified charged rotating black hole Hawking temperature in a model universe with large extra dimension based on the ADD scenario and GUP becomes

$$T_d^{GUP} = \frac{(d-3)\left(2\zeta_d + \alpha l_p\right)}{16\pi\alpha^2 l_p^2}\left[1 \pm \sqrt{1 - \frac{4\alpha^2 l_p^2\left(1 + 16\beta^2 l_p^2 \zeta_d^2\right)}{\left(2\zeta_d + \alpha l_p\right)^2}}\right] \tag{2.52}$$

Therefore, the generalized uncertainty principle that admits a minimal length, a minimal momentum, and maximal momentum gives rise to the existence of a minimal mass, $M_{\min}$, of charged rotating TeV-scale black hole. In this way, if the negative sign is chosen in Equation (2.52), the above result agrees with the standard results for large mass, based on the Heisenberg uncertainty principle. However, there is no evident physical meaning for the positive sign in Equation (2.52).

In order to find the concrete form of charged rotating micro black hole based on GUP, we consider the loss of information caused by a captured particle by the black hole which results in the increase of black hole entropy. From the Bekenstein-Smarr differential mass formula (Bekenstein, 1973; Smarr, 1973):

$$dM = \frac{1}{8\pi}\kappa dA + \Phi dQ + \Omega dJ \tag{2.53}$$

where κ, Φ, and Ω denote the surface gravity, electrostatic potential of the event horizon, and angular velocity of Kerr-Newman black hole with conserved charge and angular momentum. It is easy to show that (Ghosh & Pappnoi, 2014)

$$A_H = r_+^{d-4}\zeta^2 \frac{2\pi^{\frac{d-1}{2}}}{\Gamma\left(\frac{d-1}{2}\right)} \tag{2.54}$$

According to Equations (2.50) and (2.54), ζ is a bridge which crosses the gap between A and S, hence it has geometric and thermodynamic meanings (Xiang & Wen, 2009). Finally, based on Equations (2.33) and (2.34), we obtain the Bekenstein-Hawking entropy of charged rotating TeV-scale black hole in the presence of the generalized uncertainty principle cutoff effects as follows,

$$S_d^{GUP} = \frac{\pi^{\left(\frac{d-1}{2}\right)}}{\Gamma\left(\frac{d-1}{2}\right)} \int \left(\frac{\left(\zeta^2 - a^2\right)^{d/2-3}\left((d-2)\zeta^2 - 2a^2\right)}{16\beta^2 {l_p}^2 \zeta^2 + 1} \left(1/2\zeta^{-2} - 1/2\frac{\alpha l_p}{\zeta^3}\right)^{-1} \right) d\zeta \tag{2.55}$$

which the black hole entropy with some arbitrary number of spacetime dimensions can be calculated as

$$
\begin{aligned}
S_4^{GUP} &= 4/3\pi^{3/2}\zeta^3 + 2\pi^{3/2}\alpha l_p\zeta^2 + 4\pi^{3/2}\alpha^2{l_p}^2\zeta - 32\pi^{3/2}\zeta^2\alpha^3\beta^2{l_p}^5 - \tfrac{64}{3}\pi^{3/2}\zeta^3\alpha^2{l_p}^4\beta^2 \\
&\quad - 16\pi^{3/2}\zeta^4\alpha{l_p}^3\beta^2 - \tfrac{64}{5}\pi^{3/2}\zeta^5\beta^2{l_p}^2 + 4\pi^{3/2}{l_p}^3\alpha^3\ln\left(\zeta - \alpha l_p\right)
\end{aligned}
$$

$$
\begin{aligned}
S_5^{GUP} &= \tfrac{3}{2}\pi^2\zeta^3\sqrt{\zeta^2 - a^2} + 1/4\pi^2a^2\zeta\sqrt{\zeta^2 - a^2} - 16\pi^2\beta^2{l_p}^2\zeta^5\sqrt{\zeta^2 - a^2} \\
&\quad + 3\pi^2\sqrt{\zeta^2 - a^2}\zeta\alpha^2{l_p}^2 + 2\pi^2\sqrt{\zeta^2 - a^2}\zeta^2\alpha l_p - 4\pi^2\sqrt{\zeta^2 - a^2}\zeta a^2\alpha^2\beta^2{l_p}^4 \\
&\quad - \tfrac{64}{15}\pi^2\alpha\beta^2{l_p}^3a^2\zeta^2\sqrt{\zeta^2 - a^2} - \tfrac{96}{5}\pi^2\alpha\beta^2{l_p}^3\zeta^4\sqrt{\zeta^2 - a^2} - \tfrac{128}{15}\pi^2\alpha\beta^2{l_p}^3a^4\sqrt{\zeta^2 - a^2} \\
&\quad - 4\pi^2\beta^2{l_p}^2a^2\zeta^3\sqrt{\zeta^2 - a^2} - 6\pi^2\beta^2l^2a^4\zeta\sqrt{\zeta^2 - a^2} - 24\pi^2\sqrt{\zeta^2 - a^2}\zeta^3\alpha^2\beta^2{l_p}^4 \\
&\quad - 4\pi^2\ln\left(\zeta + \sqrt{\zeta^2 - a^2}\right)a^4\alpha^2\beta^2{l_p}^4 - \pi^2\ln\left(\zeta + \sqrt{\zeta^2 - a^2}\right)a^2\alpha^2{l_p}^2 \\
&\quad + 1/4\pi^2a^4\ln\left(\zeta + \sqrt{\zeta^2 - a^2}\right) - 6\pi^2\beta^2{l_p}^2a^6\ln\left(\zeta + \sqrt{\zeta^2 - a^2}\right)
\end{aligned}
$$

$$
\begin{aligned}
S_6^{GUP} &= \tfrac{8}{5}\pi^{5/2}\zeta^5 - \tfrac{128}{7}\pi^{5/2}\zeta^7\beta^2{l_p}^2 - \tfrac{64}{3}\pi^{5/2}\zeta^6\alpha{l_p}^3\beta^2 - \tfrac{128}{5}\pi^{5/2}\zeta^5\alpha^2{l_p}^4\beta^2 \\
&\quad + \tfrac{64}{5}\pi^{5/2}\zeta^5a^2\beta^2{l_p}^2 - 32\pi^{5/2}\zeta^4\alpha^3\beta^2{l_p}^5 + 16\pi^{5/2}\zeta^4a^2\alpha\beta^2{l_p}^3 + 2\pi^{5/2}\zeta^4\alpha l_p \\
&\quad + \tfrac{64}{3}\pi^{5/2}\zeta^3a^2\alpha^2\beta^2{l_p}^4 + \tfrac{8}{3}\pi^{5/2}\zeta^3\alpha^2{l_p}^2 - \tfrac{4}{3}\pi^{5/2}\zeta^3a^2 + 32\pi^{5/2}\zeta^2a^2\alpha^3\beta^2{l_p}^5 \\
&\quad + 4\pi^{5/2}\zeta^2\alpha^3{l_p}^3 - 2\pi^{5/2}\zeta^2a^2\alpha l_p - 4\pi^{5/2}a^2\alpha^2{l_p}^2\zeta - 4\pi^{5/2}\ln\left(\zeta - \alpha l_p\right)a^2\alpha^3{l_p}^3
\end{aligned}
\tag{2.56}
$$

Since α and β are small quantities, one can expand Equation (2.55) up to the second order of α and β based on the Equation (2.4) to conclude Equation (2.56). We still keep the terms of order of $\alpha^2\beta^2$ and sspecially for $d = 4$ up to order $\alpha^2$to reveal the effect of the beta parameter more precise and logarithmic correction as well. We restrict the range of the parameters α and β which shows that α and β cannot take any arbitrary value. In this manner, it is straightforward to find the relation of the entropy of black hole on the area in the absence of the α and β. It is easy to find that in the scenario of large extra dimensions,

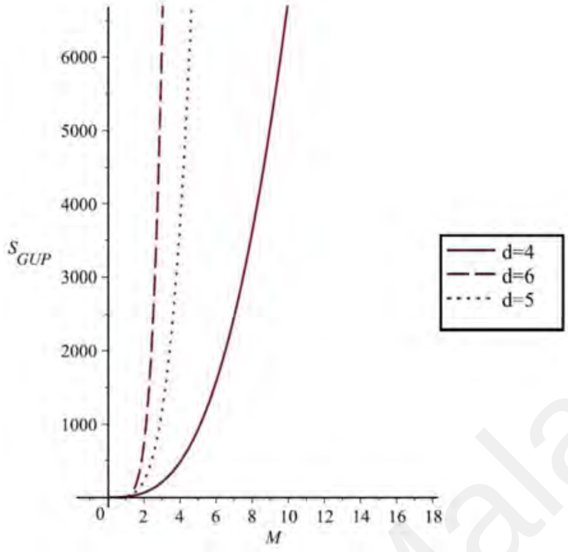

Figure 2.4: Entropy of black hole for $d = 4, 5, 6$ **dimension with** $\alpha = 0.1$ **and** $\beta = 0.01$

black hole entropy decreases and the classical picture breaks down since the black hole's entropy is small. So, the semi classical entropy could be used to measure the semi classical validity.

We now proceed to discuss some thermodynamic and related black hole parameters in terms of different dimension cases.

2.5.1 4-dimensions case

When $d = 4$, we obtain Δ as follows (see Equation (2.45))

$$\Delta = r^2 + a^2 - 2Mr + Q^2 \tag{2.57}$$

which admits a solution $r_\pm$, identified as the inner/outer event horizons. The outer event horizon is

$$r_+ = M + \sqrt{(M^2 - Q^2) - a^2} \tag{2.58}$$

In this case, the angular momentum J and charge Q must be restricted by $\left(\frac{J}{M}\right)^2 < \left(M^2 - Q^2\right)$. Other wise there is no horizon and one has a naked singularity. In which follow, we calculate ${T_d}^{GUP}$ for $d = 4$ (outer four-dimensional brane)

$$T_4^{GUP} = \tfrac{1}{128\pi M^3 J^3} \left(\begin{array}{l} 256M^8\beta^2{l_p}^2 - 256M^6Q^2\beta^2{l_p}^2 - 256M^4J^2\beta^2{l_p}^2 + 96M^4Q^4\beta^2{l_p}^2 \\ +192M^2Q^2J^2\beta^2{l_p}^2 + 96J^4\beta^2{l_p}^2 - 16M^2Q^6\beta^2{l_p}^2 - 48Q^4J^2\beta^2{l_p}^2 \\ -48\tfrac{Q^2J^4\beta^2{l_p}^2}{M^2} - 16\tfrac{J^6\beta^2{l_p}^2}{M^4} + Q^8\beta^2{l_p}^2 + 4\tfrac{Q^6J^2\beta^2{l_p}^2}{M^2} + 6\tfrac{Q^4J^4\beta^2{l_p}^2}{M^4} \\ +4\tfrac{Q^2J^6\beta^2{l_p}^2}{M^6} + \tfrac{J^8\beta^2{l_p}^2}{M^8} + 256M^5J\beta^2{l_p}^2 - 128M^3Q^2J\beta^2{l_p}^2 \\ -128MJ^3\beta^2{l_p}^2 + 16MQ^4J\beta^2{l_p}^2 + 32\tfrac{Q^2J^3\beta^2{l_p}^2}{M} + 16\tfrac{J^5\beta^2{l_p}^2}{M^3} \\ +64M^2J^2\beta^2{l_p}^2 + 4M^2J^2 \end{array} \right) \times$$
$$\left(4MJ\alpha l + 16M^4 - 8M^2Q^2 - 8J^2 + Q^4 + 2\tfrac{Q^2J^2}{M^2} + \tfrac{J^4}{M^4} + 8MJ\right) \tag{2.59}$$

Based on the Equation (2.59), the GUP gives rise to the existence of a minimal mass which one can find it by solving the following inequality

$$\frac{1}{4}\frac{\left(1 + 2\sqrt{-12\alpha^2\beta^2 l_p^4}\right)^2 l_p^2\alpha^2}{\left(16\alpha^2\beta^2 l_p^4 - 1\right)^2} < M + \sqrt{M^2 - Q^2 - \frac{J^2}{M^2}} + \frac{J^2}{M^2} \tag{2.60}$$

This inequality can be solved numerically. One can find easily that the Hawking temperature of a charged rotating micro black hole in 4-dimensions space-time is only defined for $M > M_{\max}$.

2.5.2 6-dimensions case

Equation (2.49) for $d = 6$ reduces to

$$r^3 + (a^2 - Q^2)r - \mu = 0 \tag{2.61}$$

which gives the event horizon radius as follows

$$r_+^6 = \frac{\chi^{\frac{1}{3}}}{6} - \frac{2\left(a^2 - Q^2\right)}{\chi^{\frac{1}{3}}} \tag{2.62}$$

where $\chi = 108\mu + 12\sqrt{-12Q^2 + 36Q^4a^2 - 36Q^2a^4 + 12a^6 + 81\mu^2}$ and according to the Equation (2.46), $\mu = 0.46M$. Obviously, the angular momentum and charge should be restricted to avoid no horizon and naked singularity. Therefore, we obtain

$$\begin{aligned} T_6^{GUP} = \tfrac{3\alpha l_p}{8\pi} & \left(16\left(\begin{array}{l} \frac{\sqrt[3]{4}M}{144Q^2J\mu}\left(\begin{array}{c} 24\frac{Q^4J^2}{M^2} - \frac{12Q^2J^4}{M^4} - \frac{4J^6}{M^6} \\ +72\frac{Q^2J\mu}{M} + 4Q^2 - 27\mu^2 \end{array}\right) - \\ 12\frac{4^{2/3}Q^2J\mu}{M}\left(-Q^2 + \frac{J^2}{M^2}\right) \\ \times\left(\begin{array}{c} 24\frac{Q^4J^2}{M^2} - 12\frac{Q^2J^4}{M^4} - 4\frac{J^6}{M^6} \\ +72\frac{Q^2J\mu}{M} + 4Q^2 - 27\mu^2 \end{array}\right)^{-1} \end{array}\right)^2 \beta^2{l_p}^2 + 1\right) \\ \times & \left(1 - \tfrac{2}{\alpha l_p}\left(\begin{array}{l} \frac{\sqrt[3]{4}M}{144Q^2J\mu}\left(\begin{array}{c} 24\frac{Q^4J^2}{M^2} - 12\frac{Q^2J^4}{M^4} - 4\frac{J^6}{M^6} \\ +72\frac{Q^2J\mu}{M} + 4Q^2 - 27\mu^2 \end{array}\right) \\ -12\frac{4^{2/3}Q^2J\mu}{M}\left(-Q^2 + \frac{J^2}{M^2}\right)\left(\begin{array}{c} 24\frac{Q^4J^2}{M^2} - 12\frac{Q^2J^4}{M^4} - 4\frac{J^6}{M^6} \\ +72\frac{Q^2J\mu}{M} + 4Q^2 - 27\mu^2 \end{array}\right)^{-1} \end{array}\right)\right)\Bigg) \end{aligned} \tag{2.63}$$

In the same way, one can also obtain the Hawking temperature and $M_{\min}$ respectively for other dimensions. In the scenario with large extra dimensions based on the ADD model in the presence of the most general modified uncertainty principle, the temperature of the higher dimensional charged rotating black hole increases with respect to the dimensions in constant M (Figure 2.5). In fact, the higher dimensional black holes at fixed event horizon radii are hotter and their minimum mass as black hole remnant mass increase (see Figure 2.5). In this case, there is restriction of the range of the parameters α and β. Based on the Equation (2.52) and its respective minimum mass which shows that α and β cannot take

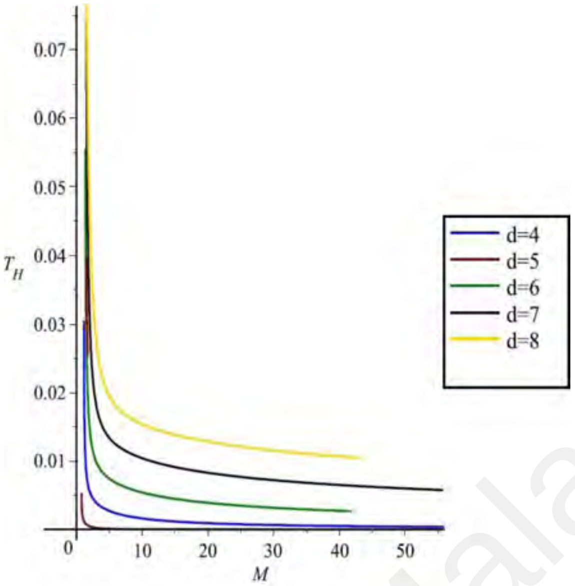

Figure 2.5: Hawking temperature for different space-time dimensions

arbitrary value, we obtain

$$2\frac{\left(1-2\sqrt{16\beta^2{l_p}^2\zeta^2+1}\right)\zeta}{\left(64\beta^2{l_p}^2\zeta^2+3\right)l_p} \le \alpha \le 2\frac{\left(1+2\sqrt{16\beta^2{l_p}^2\zeta^2+1}\right)\zeta}{\left(64\beta^2{l_p}^2\zeta^2+3\right)l_p} \tag{2.64}$$

which could be considered as range of α and β. Here, we highlight that maximum Hawking temperature and minimum mass decreases when α increases (Figure 2.6) while β causes increasing temperature (see Figure 2.7). In this manner, Figure 2.8 shows that the Entropy increases when α increases and β causes decreasing entropy (see Figure 2.9). Meanwhile, α and β are related parameters which depend on the aspects of the candidates for quantum gravity proposal. In this way we revealed the effect of minimal length, maximal momentum, and minimal momentum on the thermodynamical parameters like Hawking temeperature and the entropy as well (see Equations (2.56), (2.59), (2.63).

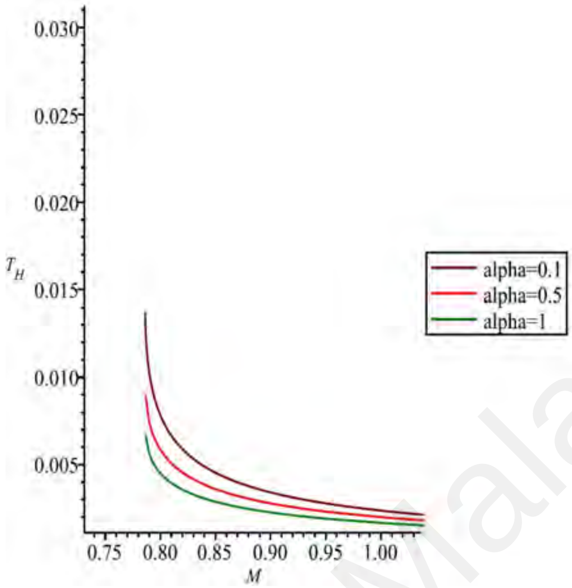

Figure 2.6: Hawking temperature Variation for different α in a fixed β

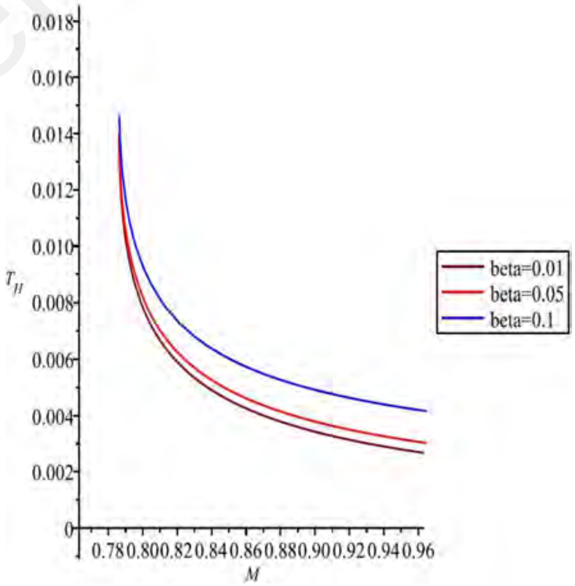

Figure 2.7: Hawking temperature Variation for different β in a fixed α

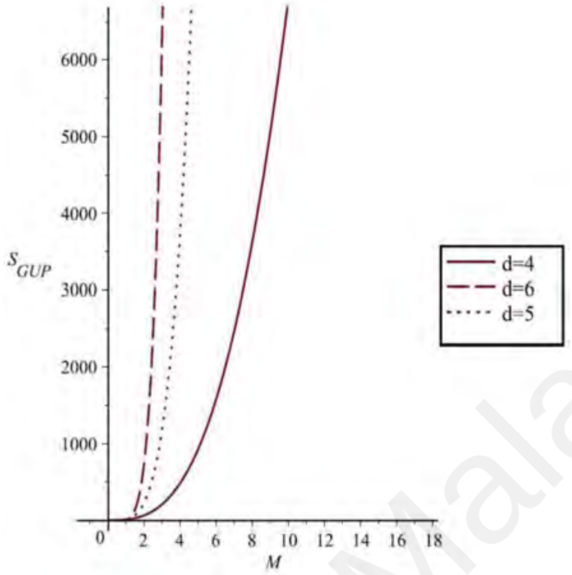

Figure 2.8: Entropy Variation for different α in a fixed β

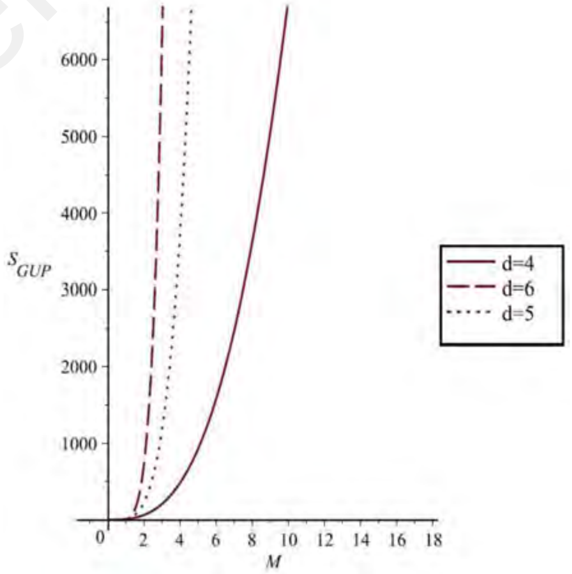

Figure 2.9: Entropy Variation for different β in a fixed α

2.6 Effects of angular momentum and charge on thermodynamics

In order to characterize black hole, there are only mass, charge, and angular momentum (Frolov et al., 2005; Padmanbhan, 2005). Microscopic black holes are called thermal black hole. We would like to highlight that they are considered as semi-classical model in the literature. Same as charged non-rotating black hole case, this type of black holes are expected to go through different stages during their life time (Giddings & Thomas, 2002) as follows: I) The balding phase: at this initial stage, the black hole emits mainly gravitational radiations and sheds all the quantum numbers and multiple momenta apart from those determined by its mass, charge and angular momentum. II) The spin-down phase: during this stage, the black hole starts losing its angular momentum through the emission of Hawking radiation. III) The Schwarzschild phase: the black hole is no longer rotating and continues to lose its mass in the form of Hawking radiation. IV) The Planck phase: at this final stage the black hole mass approaches the true Planck scale as black hole remnant with mass M_{min} which was discussed in the previous sections. The allowed initial particles forming TeV-scale black holes at the LHC are quarks, anti-quarks, and gluons which can form different types of the black holes in terms of charge and spin (Gingrich, 2010). Although we are dealing with a micro black hole as a semi-classical black hole, for simplicity we have considered the initial angular momentum of the black hole due to the spin states of the incoming partons and ignore the possibility of an initial small orbital angular momentum due to an impact parameter.

Figure 2.12 shows the angular momentum effects on the minimum mass and maximum Hawking temperature. The minimum mass and its order of magnitude increases when angular momentum increases and meantime the temperature peak displaces to the lower temperature. It is obvious that charge variation causes changes on temperature dramatically compare to the angular momentum variation (see Figure 2.15).

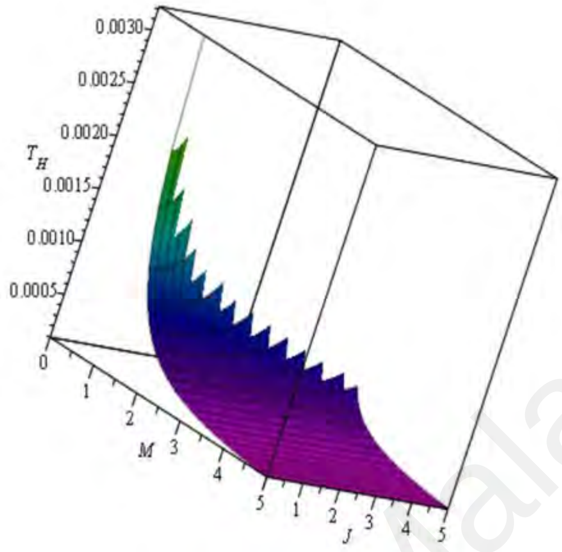

Figure 2.10: Spin-down phase effect on the black hole temperature

After the balding and spin-down phases, the black hole will decay via the semi-classical Hawking evaporation process (Hawking, 1975). We have shown that after spin-down phase the black hole continues to evaporate without rotation which is considered as the Schwarzschild phase (Figures 2.11 and 2.13).

For the spin-down phase, the absorption probability also depends on the angular momentum parameter and the space-time properties and emission rate increases with the increase in the angular momentum (Ido et al., 2005). Figures 2.10 and 2.11 show no special distribution in terms of the angular momentum during the spin-down phase because this phase has a preferred axis for the bran localized emission, the rotation axis of the TeV-scale black hole (Kanti, 2009). The initial particles formed nine possible charge states: $\pm\frac{4}{3}, \pm 1, \pm\frac{2}{3}, \pm\frac{1}{3}, 0$ (Landsberg, 2006). Figure 2.14 shows the charge effects on the minimum mass and maximum Hawking temperature of black hole. Obviously, when charge increases, the minimum mass and its order of magnitude increases, and the

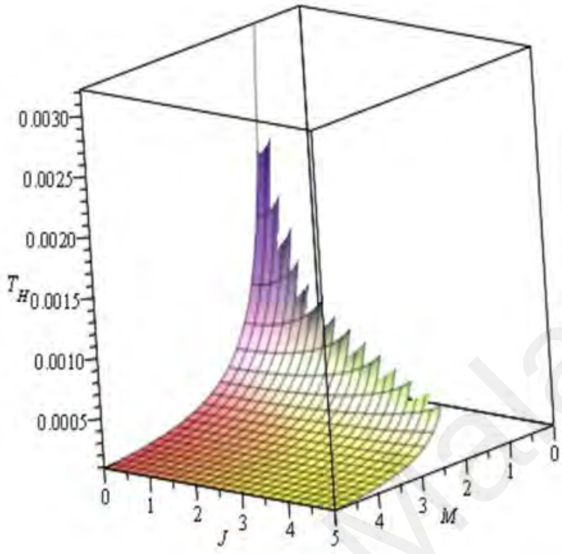

Figure 2.11: Angular momentum, J, and mass, M vs. the Hawking temperature

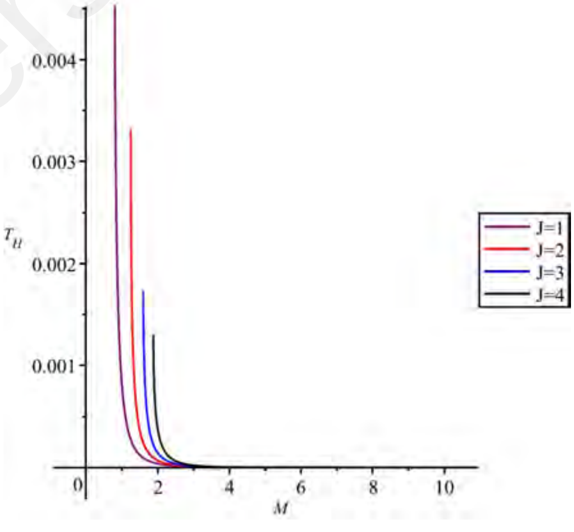

Figure 2.12: Hawking temperature Variation for different angular momentum ***J***

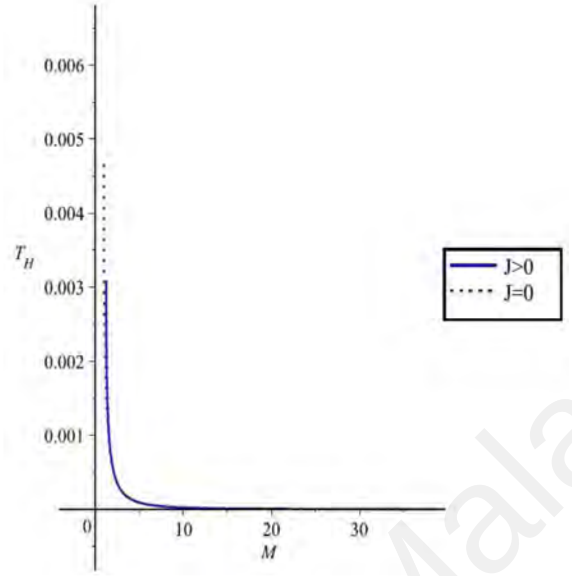

Figure 2.13: Continue evaporation after the spin-down phase

temperature peak displaces to the lower temperature as well as angular momentum effect.

Here, we would like to draw attention that we have described the higher dimensional Kerr-Newman black hole geometry based on the solution of the Einstein equation field in reference (Ghosh & Pappnoi, 2014) due to the line element dependency to gauge charge. Although it was shown (Dai et al., 2009) that the TeV-scale black hole charge will reach zero much faster than its mass and the charge to mass ratio is much less than one.

Therefore, if the fundamental Planck scale is of the order of TeV, the Large Hadron Collider would produce charged rotating micro black hole which as a consequence of their evaporation, degenerate to charged non-rotating TeV-scale balck hole at the last stage and thus yield charged black hole remnants.

2.7 Black Holes Remnan as Dark Matter Candidate

Since Zwicky's observation of the large velocity dispersion of the members of the coma galaxy (Zwicky, 1933), the dark matter problem has been raised as part of the astrophysics

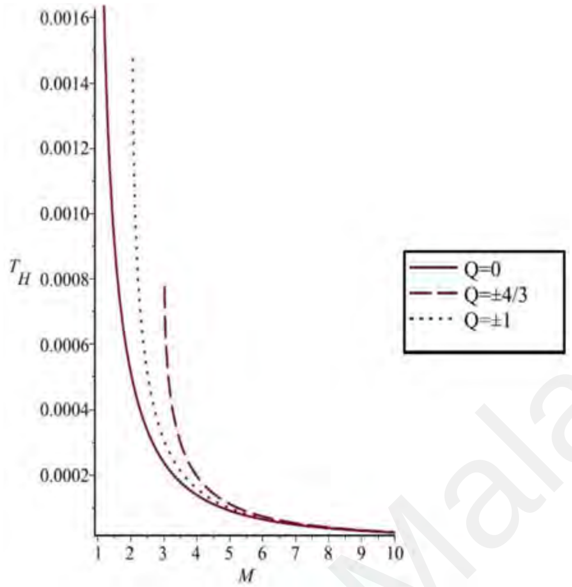

Figure 2.14: Effect of different charge amounts on Hawking temperature

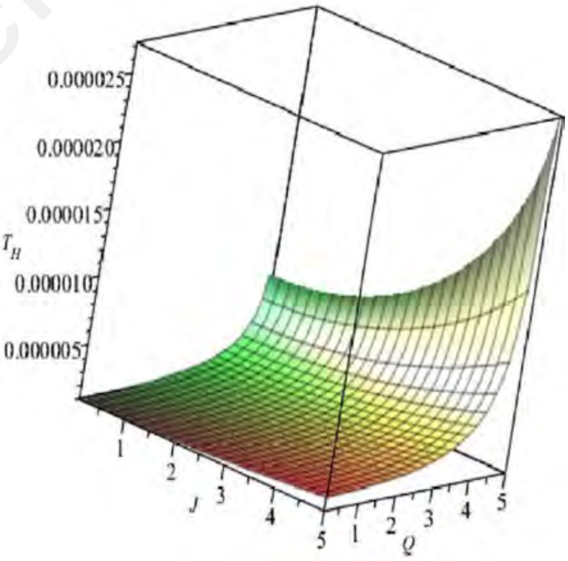

Figure 2.15: Effect of the angular momentum, J and charge, Q on the Hawking temperature

for more than eighty years. However, it took several decades to be recognized as a real problem. Its modern form goes back to the early 1980's when the so-called cold dark matter paradigm appeared (Peebles, 1982). Most of the matter in the universe is made up of the dark matter in which its identity is an open problem. So far, it has been observed only through its gravitational interactions. A logical possibility is that dark matter is hidden, that is, neutral under all standard model gauge interactions (Berezhiani et al., 1996; 2001; Mohapatra & Teplitz, 2000; Foot & Volas, 2004). There exist many dark matter candidates. In order to describe the properties of elementary particle candidates all the possible models use the standard concept of quantum field theory (Kikuchi & Okada, 2008, Kusenko & Shaposhinkov, 1998). Most of the candidates are non-baryonic weakly interacting massive particles (WIMPs) or WIMP-like particles. Black Hole remnants are a natural candidate for dark matter (McGibbon, 1987) since they are a form of WIMPs. Recently, it is investigated in which non-charged black hole remnants are the primary source of the dark matter based on the GUP model (Chen & Adler, 2003; Adler et al., 2001; Nozari & Mehdipour, 2006). On the other hand, some models have been proposed in which dark matter particles are charged under some hidden gauge group (Ackerman et al., 2009; Feng & Kumar, 2008; Hooper & Zurek, 2008; Kim et al., 2008; Huh et al., 2008). Here, based on the Equations (2.25), and (2.28), we have shown, the final stage of evaporation of the charged TeV-scale black hole is a remnant which has mass increasing with spacetime dimensions.The allowed particles forming the black hole at LHC are quarks, antiquarks, and gluons which formed nine possible electric charge states such as $\pm\frac{4}{3}$, ± 1, $\pm\frac{2}{3}$, $\pm\frac{1}{3}$, 0 (Gingrich, 2010; Landsberg, 2006). Figure 2.14 shows the electric charge effects on the minimum mass of the black hole and the maximum Hawking temperature. In this case, when the electric charge increases, the minimum mass and its order of magnitude increases, and the temperature peak shifts to the lower temperature. This consequence allows us to divide the remnant into several categories. In case of $Q = 0$, the stable remnant of the micro black hole could be considered as WIMPs or WIMP-like particles (Chen & Adler, 2003; Adler et al., 2001; Nozari & Mehdipour, 2006). The ratio of the black hole charge, Q, with respect to its mass, M, generally could be considered as three states; i) $Q > M$ ii) $Q \leq M$ iii) $Q \simeq M$. It can be shown that it is impossible to make the electric charge of a classical black hole larger than its mass, in Planck unit, by an influx of the charged particles on the horizon (Misner et al., 1973; Lightman et al., 1975) and this result remains true in TeV-scale as well (Dolgov & Freese, 2007). The charged black hole strongly prefer to emit particles of the same sign since they penetrate the potential barrier easier (Dai et al., 2009). This allows the black hole to discharge its electric charge easily. In this manner, the electric charge goes to zero much faster than its mass and it has been shown (Dai et al., 2009) that for the dark matter particles whose the ratio of the charge to the mass is much less than one, it could exclude the heavy dark matter and the existence of primordial black hole is incompatible with the ratio of the charge to the mass which is of order one. It was calculated, that the charge and the mass of the charged particles which could be considered as a candidate of the dark matter, fall in the following range

$$100\,(Q/e)^2 \leq M \leq 10^8\,(Q/e)\,TeV \tag{2.65}$$

then, their absence in the galactic disk can be naturally explained by their interaction with the galactic magnetic fields (Chuzhoy & Kolb, 2009). Therefore, evidently, the charged Tev-scale black hole remnant could be considered as the potential candidate of the dark matter. In this case, it is straightforward to calculate the limited range of the minimal length and maximal momentum coefficient, α, based on the Equations (2.25) and (2.65).

Table 2.1: Range of the minimal length and maximal momentum coefficient, α, limited by the possible mass of the dark matter candidate for different values of the charge, dimensions $d = 4, 5, 6$ in GUPI

$\lvert Q \rvert$	$d = 4$	$d = 5$	$d = 6$
1/3	$0.13788 \leq \alpha \leq 1.458 \times 10^8$	$0.48727 \leq \alpha \leq 1.164 \times 10^4$	$0.77370 \leq \alpha \leq 5.502 \times 10^2$
2/3	$0.13759 \leq \alpha \leq 2.916 \times 10^8$	$0.48630 \leq \alpha \leq 1.646 \times 10^4$	$0.77207 \leq \alpha \leq 6.933 \times 10^2$
1	$0.13753 \leq \alpha \leq 4.374 \times 10^8$	$0.48612 \leq \alpha \leq 2.015 \times 10^4$	$0.77178 \leq \alpha \leq 7.936 \times 10^2$
4/3	$0.13751 \leq \alpha \leq 5.832 \times 10^8$	$0.48606 \leq \alpha \leq 2.327 \times 10^4$	$0.77167 \leq \alpha \leq 8.735 \times 10^2$

Table 2.2: Range of the minimal length and maximal momentum coefficient, α, as well as minimal momentum coefficient, β, limited by the possible mass of the dark matter candidate for different values of the charge, dimensions $d = 4, 5, 6$ in GUPII

$\|Q\|$	$d = 4$	$d = 5$	$d = 6$
1/3	$0.21865 \leq \alpha \leq 4.443 \times 10^7$	$0.09485 < \alpha \leq 3.546 \times 10^3$	$0.23577 < \alpha \leq 1.676 \times 10^2$
2/3	$0.21703 \leq \alpha \leq 8.886 \times 10^7$	$0.09473 \leq \alpha \leq 5.014 \times 10^3$	$0.23528 \leq \alpha \leq 2.112 \times 10^2$
1	$0.21674 \leq \alpha \leq 1.333 \times 10^7$	$0.094718 \leq \alpha \leq 6.141 \times 10^3$	$0.23519 \leq \alpha \leq 2.418 \times 10^2$
4/3	$0.21663 \leq \alpha \leq 1.777 \times 10^7$	$0.094710 \leq \alpha \leq 7.092 \times 10^3$	$0.23515 \leq \alpha \leq 2.661 \times 10^2$
1/3	$0.649 \times 10^{-8} \leq \beta \leq 1.32021$	$0.814 \times 10^{-4} \leq \beta \leq 3.04333$	$0.172 \times 10^{-2} \leq \beta \leq 1.22436$
2/3	$0.324 \times 10^{-8} \leq \beta \leq 1.33008$	$0.575 \times 10^{-4} \leq \beta \leq 3.04704$	$0.136 \times 10^{-2} \leq \beta \leq 1.22693$
1	$0.216 \times 10^{-8} \leq \beta \leq 1.33189$	$0.470 \times 10^{-4} \leq \beta \leq 3.04772$	$0.119 \times 10^{-2} \leq \beta \leq 1.22740$
4/3	$0.162 \times 10^{-8} \leq \beta \leq 1.33252$	$0.407 \times 10^{-4} \leq \beta \leq 3.04796$	$0.108 \times 10^{-2} \leq \beta \leq 1.22757$

Table 2.1 shows the range of the minimal length and the maximal momentum, α, for different values of the charge in different dimensions, $d = 4, 5, 6$. It is obvious, that increase of the spacetime dimension applies narrow cuts on the range of the α in presence of the GUPI. In this way, one can also calculate the range of the minimal momentum coefficient, β, based on Equations (2.28) and (2.65) as well (see Table 2.2). However, to calculate the range of the α and β, one needs to take into account $\beta^2 \leq \frac{1}{12\alpha^2}$ as another constraint (see Equation (2.28)) rather than Equation (2.65). In this case, it is obvious, that the range of the α has more limited in presence of the β (Table 2.1 and 2.2). As a potential candidate for the dark matter, and based on the pioneering work of Chuzhoy et al (Chuzhoy & Kolb, 2009), one can consider the charged TeV-scale black hole remnant into three categories. The first one is the micro black hole remnant with positive unit charge which its chemical properties would be very similar to the proton and could recombined with the electrons. The second group is the TeV-scale remnant with negative unit charge which can recombine with the baryons, forming neutral or positively charged particles. The third category is the remnant with fractional charge which might also recombine with the ordinary matter, though with smaller binding energies in which the combinations would be more vulnerable to dissociation. Therefore, if the fundamental Plank scale is of the order of TeV, LHC would produce charged black hole which as a consequence of their evaporation yield the charged black hole remnants as a candidate of dark matter particles.

CHAPTER 3: THE CMS DETECTOR AT THE LARGE HADRON COLLIDER

3.1 Introduction

The analysis described in this thesis has been performed using pp collisions collected by CMS in 2015. CMS is one of the general purpose detectors at the LHC. In this chapter, a brief introduction to the CMS detector is given by describing its major components. The types of information used in the analyses are mostly based on calorimeter measurements.

3.2 The Large Hadron Collider

The LHC is the world's largest particle accelerator operating at the highest collider energy ever achieved in an accelerator. It is a ring 27 kilometres in circumference, 100 metres beneath the French-Swiss border near Geneva, Switzerland. It is designed to collide mainly proton-proton (pp) beams, moving in opposite directions, with 14 TeV centre of mass energy and a luminosity of $10^{34}\ cm^{-2}\ s^{-1}$. Inside the LHC, there are eight accelerating cavities and each one of them provides a strong electric field of about 5 MV/m used to accelerate the beams. It also contains 1232 superconducting main dipole magnets (to bend the beams), providing a total field of 8.33 T, and 392 super conducting quadrupole magnets (to focus the beams), providing a total field of 6.86 T. The LHC is expected to shed light on some of the most fundamental questions of physics, the understanding of basic laws through which nature governs this universe. In the exciting year of 2015, the LHC not only successfully operated at 13 TeV centre of mass energy but also accomplished one of its major goals, the discovery of the Higgs boson in past few years.

There are four major detectors on the LHC ring: ATLAS, CMS, ALICE dedicated to heavy ion physics) and LHCb (dedicated to b-physics). ATLAS (A Toroidal LHC ApparatuS) and CMS (Compact Muon Solenoid) are the two general purpose detectors that have been built to probe pp collisions mainly. The analysis described in the next chapter is

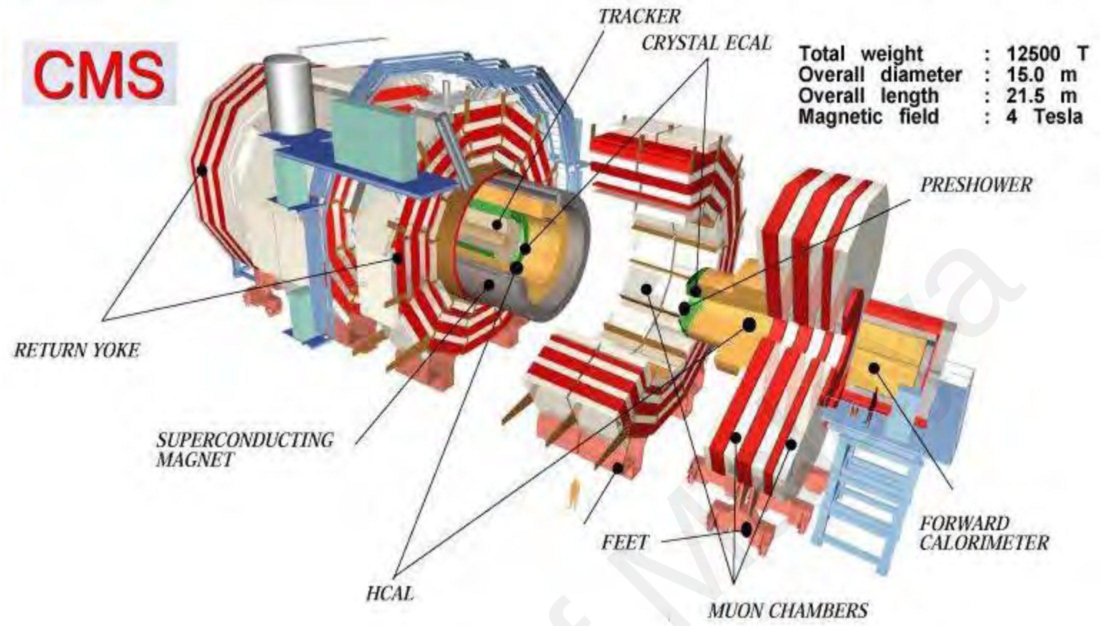

Figure 3.1: Layout of the full CMS detector

performed with the CMS 2015 data from pp collisions.

3.3 The CMS Detector

The CMS detector is shown in Figure 3.1. The CMS experiment is 21 m long, 15 m wide and 15 m high, and sits in a cavern that could contain all the residents of Geneva; albeit not comfortably. The detector is like a giant filter, where each layer is designed to stop, track or measure a different type of particle emerging from proton-proton and heavy ion collisions. Finding the energy and momentum of a particle gives clues to its identity, and particular patterns of particles or “signatures” are indications of new and exciting physics.

The detector is built around a huge solenoid magnet. This takes the form of a cylindrical coil of superconducting cable, cooled to $-268.5^{\circ c}$, that generates a magnetic field of 4

Tesla, about 100,000 times that of the Earth. Particles emerging from collisions first meet a tracker, made entirely of silicon, that charts their positions as they move through the detector, allowing us to measure their momentum. Outside the tracker are calorimeters that measure the energy of particles. In measuring the momentum, the tracker should interfere with the particles as little as possible, whereas the calorimeters are specifically designed to stop the particles in their tracks.

The Electromagnetic Calorimeter (ECAL) - made of lead tungstate, a very dense material that produces light when hit – measures the energy of photons and electrons whereas the Hadron Calorimeter (HCAL) is designed principally to detect any particle made up of quarks (the basic building blocks of protons and neutrons). The size of the magnet allows the tracker and calorimeters to be placed inside its coil, resulting in an overall compact detector. As the name indicates, CMS is also designed to measure muons. The outer part of the detector, the iron magnet "return yoke", confines the magnetic field and stops all remaining particles except for muons and neutrinos. The muon tracks are measured by four layers of muon detectors that are interleaved with the iron yoke. The neutrinos escape from CMS undetected, although their presence can be indirectly inferred from the "missing transverse energy" in the event. Within the LHC, bunches of particles collide up to 40 million times per second, so a "trigger" system that saves only potentially interesting events is essential. This reduces the number recorded from one billion to around 100 per second.

CHAPTER 4: DATA AND MONTE CARLO SAMPLES

4.1 Data

For the analysis described in this note, the data collected by the CMS experiment at a center-of-mass energy 13 TeV which corresponds to a total integrated luminosity of 2.2 fb^{-1} are used. The data samples used are given below:

- /JetHT/Run2015C_25ns-05Oct2015-v1/MINIAOD
- /JetHT/Run2015D-05Oct2015-v1/MINIAOD
- /JetHT/Run2015D-PromptReco-v4/MINIAOD

Luminosity sections are used only if the LHC operated at 25ns bunch crossing spacing and the CMS solenoid delivered a field of 3.8 T, and must be certified by the CMS data certification team. The luminosity sections used were taken from the CMS data certification team's Golden JSON:

- Cert_246908-260627_13TeV_PromptReco_Collisions15_25ns_JSON.txt

4.2 MC Background

The simulated background used in this analysis are listed in table 4.1. The samples are from the RunIISpring15 cycle of CMS MC production and are produced using the CMSSW_7_4_* release of the CMS software CMSSW.

Table 4.1: The major Monte Carlo simulated samples using in the analyis are listed

Sample	/Official Dataset Name/*/RunIISpring15DR74-Asympt25ns_MCRUN2_74_V*/MINIAODSIM	# No. of Events	Cross-section [pb]
$t\bar{t}$	/TTJets_TuneCUETP8M1_13TeV-madgraphMLM-pythia8/*	11339232	831.64
$WJets$	/WJetsToLNu_HT-400To600_TuneCUETP8M1_13TeV-madgraphMLM-pythia8/*	1901705	48.98
	/WJetsToLNu_HT-600To800_TuneCUETP8M1_13TeV-madgraphMLM-pythia8/*	3984529	12.8
	/WJetsToLNu_HT-800To1200_TuneCUETP8M1_13TeV-madgraphMLM-pythia8/*	1574633	5.26
	/WJetsToLNu_HT-1200To2500_TuneCUETP8M1_13TeV-madgraphMLM-pythia8/*	255637	1.33
	/WJetsToLNu_HT-2500ToInf_TuneCUETP8M1_13TeV-madgraphMLM-pythia8/*	253036	0.03
qcd	/QCD_HT100to200_TuneCUETP8M1_13TeV-madgraphMLM-pythia8/*	80093092	27540000
	/QCD_HT200to300_TuneCUETP8M1_13TeV-madgraphMLM-pythia8/*	18717349	1735000
	/QCD_HT300to500_TuneCUETP8M1_13TeV-madgraphMLM-pythia8/*	20086103	366800
	/QCD_HT500to700_TuneCUETP8M1_13TeV-madgraphMLM-pythia8/*	19542847	29370
	/QCD_HT700to1000_TuneCUETP8M1_13TeV-madgraphMLM-pythia8/*	15011016	6524
	/QCD_HT1000to1500_TuneCUETP8M1_13TeV-madgraphMLM-pythia8/*	4963895	1064
	/QCD_HT1500to2000_TuneCUETP8M1_13TeV-madgraphMLM-pythia8/*	3848411	121.50
	/QCD_HT2000toInf_TuneCUETP8M1_13TeV-madgraphMLM-pythia8/*	1961774	25.40
γ + jets	/GJets_HT-40To100_TuneCUETP8M1_13TeV-madgraphMLM-pythia8/*	4597996	23080.0
	/GJets_HT-100To200_TuneCUETP8M1_13TeV-madgraphMLM-pythia8/*	5026005	9110.0
	/GJets_HT-200To400_TuneCUETP8M1_13TeV-madgraphMLM-pythia8/*	10328623	2281.0
	/GJets_HT-400To600_TuneCUETP8M1_13TeV-madgraphMLM-pythia8/*	2476770	273.0
	/GJets_HT-600ToInf_TuneCUETP8M1_13TeV-madgraphMLM-pythia8/*	2550765	94.50
Drell-Yan	/DYJetsToLL_M-50_HT-100to200_TuneCUETP8M1_13TeV-madgraphMLM-pythia8/*	2625679	139.40
	/DYJetsToLL_M-50_HT-200to400_TuneCUETP8M1_13TeV-madgraphMLM-pythia8/*	955972	42.75
	/DYJetsToLL_M-50_HT-400to600_TuneCUETP8M1_13TeV-madgraphMLM-pythia8/*	1049242	5.49
	/DYJetsToLL_M-50_HT-600toInf_TuneCUETP8M1_13TeV-madgraphMLM-pythia8/*	998912	2.21

4.3 Signals

Signal simulation is done using BlackMax 2.02.0 (Dai et al., 2008) (semi-classical BH and string balls), Charybdis2 1.003 (Harris et al., 2003) (semi-classical BH), and qbh 3.00 (Gingrich, 2010) generators. Most of the samples are generated privately, with the setup identical to that used in central production. The CMS detector performance is simulated using FastSim (Orbaker, 2009). A number of samples were also simulated centrally, using detailed CMS detector simulation via geant4 (Geant4 Collaboration, 2003). Privately produced samples were extensively validated against the centrally produced one, and an excellent agreement between the reconstructed quantities has been observed as shown in Figure 4.1 and Figure 4.2.

For the semi-classical BH signal, we used the set of signal samples listed in Table 4.2. The minimum black hole mass (M_{BH}) points are generated in 0.5 TeV steps.

For the string ball (SB) signals, it's important to make sure that the signal points correspond to the SB formation regime. This can be achieved by an appropriate choice of the M_D, n, the string coupling g_S, and the string scale M_S. Similar to the case of BH, we only consider SB formation when M_{SB} exceeds M_S. There are two characteristic mass points in the string ball production (Dimopoulos & Emparan, 2002): when the minimum string ball mass M_{SB} is equal to M_S/g_S and to M_S/g_S^2. The second point corresponds to a collapse of the SB into a BH. Below the second point, the SB is formed, which then evaporates at a constant Hagedorn temperature (Hagedorn, 1965) equal to $M_S/(2\sqrt{2}\pi)$. The first characteristic point corresponds to the saturation of the SB production. Above this point, the parton-level cross section does not depend on the string ball mass. Therefore, the parameters were chosen in such a way that the sensitivity of this search corresponds to $M_{SB} < M_S/g_S^2$, i.e. the SB regime. For typical M_S values ~ 1 TeV we are able to probe, the sensitivity of the search mainly corresponds to the saturated SB production.

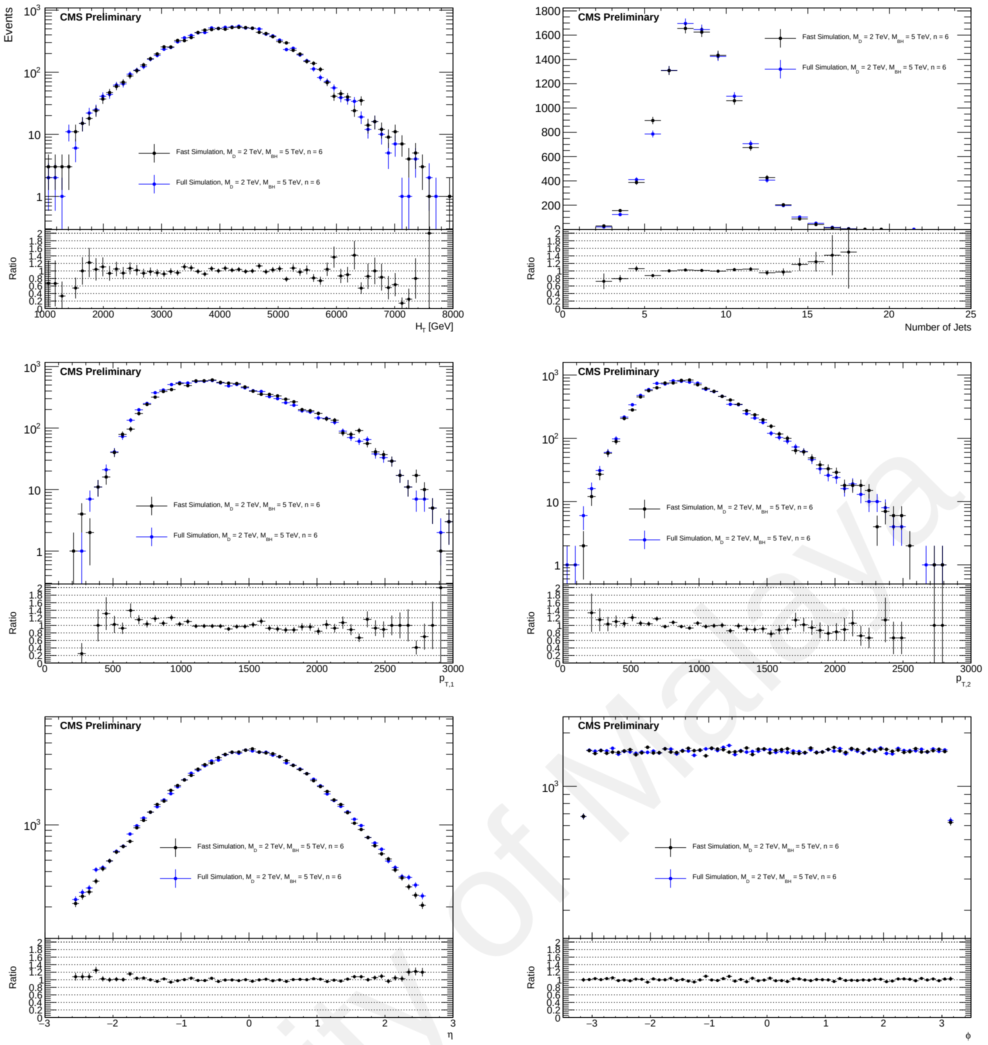

Figure 4.1: The distributions of the scalar sum of the transverse momenta of all inclusively selected-jets events (H_T) (top left), the number of jet multiplicities (top right), the transverse momentum of the first (middle left) and second (middle right) leading jets, the pseudorapidity (η) of all jets (bottom left), and the azimuthal angle of all jets (ϕ) (bottom right) and are shown. The excellent agreements between the fast simulation (black points) and full simulation (blue points) are observed

As shown in reference (Dimopoulos & Emparan, 2002), in the string ball model used, there is a correspondence between the fundamental Planck scale M_D and the string scale M_S (assuming compactification of extra dimensions on a torus): $M_D = (2\pi)^{\frac{6-n}{2+n}} g_S^{\frac{-2}{2+n}} M_S$. Given small dependence of the SB cross section on the number of extra dimensions, we probe SB production for the case of fixed $n = 6$, which simplifies the above formula to: $M_D = M_S / g_S^{\frac{1}{4}}$. Typical cross sections of SB production as a function of M_{SB} for various choices of the string scale and coupling are shown in Figure 4.3, which allow us to pick

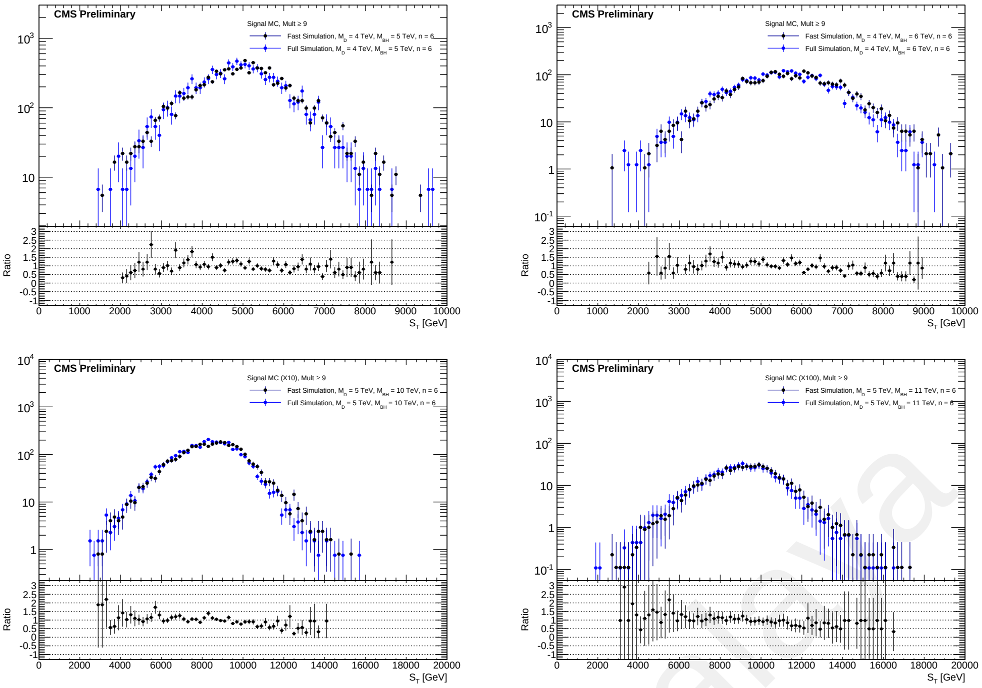

Figure 4.2: The distributions of S_T for events with multiplicity $N \geq 9$ for other microscopic black hole scenarios with six extra dimensions: $M_D = 4$ TeV, $M_{BH} = 5$ TeV (top left), $M_D = 4$ TeV, $M_{BH} = 6$ TeV (top right), $M_D = 5$ TeV, $M_{BH} = 10$ TeV (bottom left), and $M_D = 5$ TeV, $M_{BH} = 11$ TeV (bottom right). Even in more extreme BH scenarious, good agreement between fast simulation and full simulation is observed

the set of the parameters we expect to probe with the current data set. This set of signal points is listed in Table 4.5.

Finally, for quantum BH production, we use the qbh version 3 generator and produce the signal points listed in Table 4.4.

For all the signal samples we use leading order (LO) MSTW2008LO (Martin et al., 2010) parton distribution functions (PDF). This choice is driven by the fact that this set tends to give conservative estimate of the signal cross section at high masses, as checked with the modern NNPDF3.0 (NNPDF Collaboration, 2015) LO PDFs (with the value of strong coupling constant of 0.118 used for the central prediction) with a standard uncertainty eigenset, shown in Figure 4.4.

While the cross section variation at very large black hole masses due to PDF uncertainties

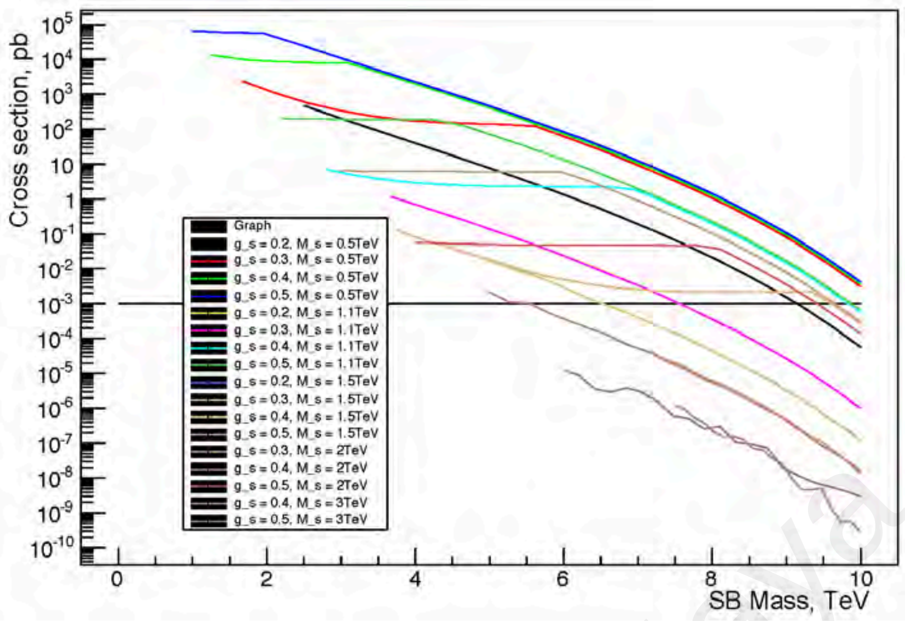

Figure 4.3: Cross section of string ball production as a function of the minimum string ball mass, indicating two transition points. The horizontal line corresponds to 1 fb cross section, which is indicative of the expected sensitivity of this analysis

can be as large as an order of magnitude the MSTW2008LO PDFs correspond to the lower side of this uncertainty range, thus indicating a reasonable and conservative choice for signal simulation. (We do not include the PDF uncertainty in the cross section limit calculations, as they belong to the theoretical uncertainty on the signal, and not to the experimental procedure used to obtain the limits.) While the MSTW2008LO PDF has been superseded more recently by the MMHT2014LO PDF (Harland-Lang et al., 2015), numerically the results for massive BHs based on these two PDF sets are indistinguishable, as there were no new data constraining PDFs at such large x added as a part of the global fit used for the MMHT2014LO PDF extraction. Since the Run 1 publications are all based on the MSTW2008LO PDF set, we kept the same set for the Run 2 analysis for straightforward and direct comparison of the two results.

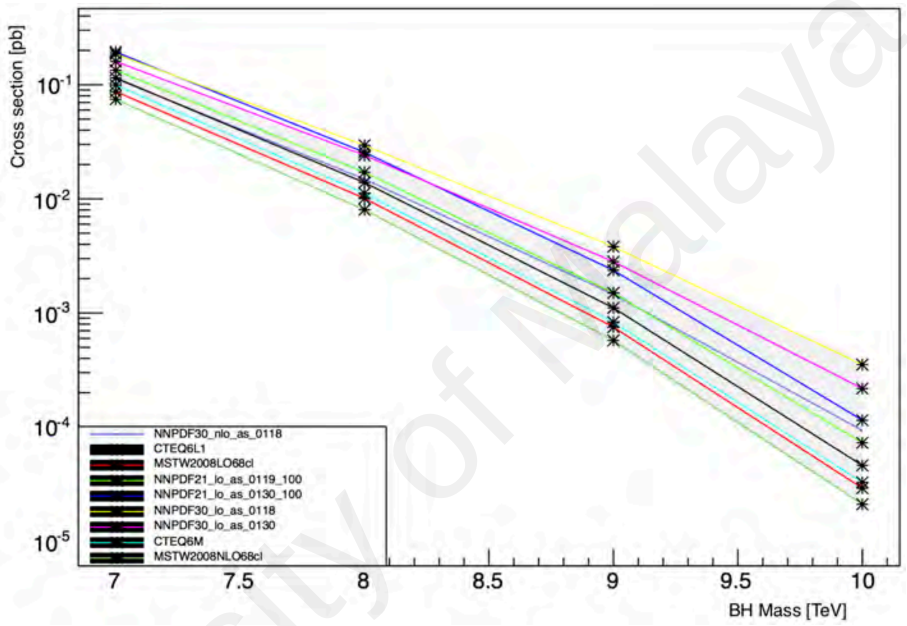

Figure 4.4: Cross section of semi-classical black hole production as a function of the minimum black hole mass for various choices of PDF set used for signal simulation. The dark blue curve and the surrounding hatched band correspond to NNPF3.0 LO PDF set and its uncertainty. The MRST2008LO set (shown with the red line) is conservatively used to estimate signal cross section in this analysis. The signal points correspond to $M_D = 5.0$ TeV, $n = 6$ and non-rotating black holes without stable remnant

Table 4.2: **Semi-classical black hole signal samples used in the analysis**

M_D, TeV	n	M_{BH}, TeV	$Generator$
Non-rotating black holes, no gravitons			
2.0	2, 4, 6	3.0–11.0	BlackMax
3.0	2, 4, 6	4.0–11.0	BlackMax
4.0	2, 4, 6	5.0–11.0	BlackMax
5.0	2, 4, 6	6.0–11.0	BlackMax
6.0	2, 4, 6	7.0–11.0	BlackMax
7.0	2, 4, 6	8.0–11.0	BlackMax
8.0	2, 4, 6	9.0–11.0	BlackMax
9.0	2, 4, 6	10.0, 11.0	BlackMax
Nonrotating black holes			
2.0	2, 4, 6	3.0–11.0	Charybdis
3.0	2, 4, 6	4.0–11.0	Charybdis
4.0	2, 4, 6	5.0–11.0	Charybdis
5.0	2, 4, 6	6.0–11.0	Charybdis
6.0	2, 4, 6	7.0–11.0	Charybdis
7.0	2, 4, 6	8.0–11.0	Charybdis
8.0	2, 4, 6	9.0–11.0	Charybdis
9.0	2, 4, 6	10.0, 11.0	Charybdis
Rotating black holes, no gravitons			
2.0	2, 4, 6	3.0–11.0	BlackMax
3.0	2, 4, 6	4.0–11.0	BlackMax
4.0	2, 4, 6	5.0–11.0	BlackMax
5.0	2, 4, 6	6.0–11.0	BlackMax
6.0	2, 4, 6	7.0–11.0	BlackMax
7.0	2, 4, 6	8.0–11.0	BlackMax
8.0	2, 4, 6	9.0–11.0	BlackMax
9.0	2, 4, 6	10.0, 11.0	BlackMax
Rotating black holes			
2.0	2, 4, 6	3.0–11.0	BlackMax
3.0	2, 4, 6	4.0–11.0	BlackMax
4.0	2, 4, 6	5.0–11.0	BlackMax
5.0	2, 4, 6	6.0–11.0	BlackMax
6.0	2, 4, 6	7.0–11.0	BlackMax
7.0	2, 4, 6	8.0–11.0	BlackMax
8.0	2, 4, 6	9.0–11.0	BlackMax
9.0	2, 4, 6	10.0, 11.0	BlackMax
2.0	2, 4, 6	3.0–11.0	Charybdis
3.0	2, 4, 6	4.0–11.0	Charybdis
4.0	2, 4, 6	5.0–11.0	Charybdis
5.0	2, 4, 6	6.0–11.0	Charybdis
6.0	2, 4, 6	7.0–11.0	Charybdis
7.0	2, 4, 6	8.0–11.0	Charybdis
8.0	2, 4, 6	9.0–11.0	Charybdis
9.0	2, 4, 6	10.0, 11.0	Charybdis

Table 4.3: Semi-classical black hole signal samples used in the analysis

M_D, TeV	n	M_{BH}, TeV	$Generator$
Rotating black holes, with mass/momentum loss			
2.0	2, 4, 6	3.0–11.0	Charybdis
3.0	2, 4, 6	4.0–11.0	Charybdis
4.0	2, 4, 6	5.0–11.0	Charybdis
5.0	2, 4, 6	6.0–11.0	Charybdis
6.0	2, 4, 6	7.0–11.0	Charybdis
7.0	2, 4, 6	8.0–11.0	Charybdis
8.0	2, 4, 6	9.0–11.0	Charybdis
9.0	2, 4, 6	10.0, 11.0	Charybdis
Rotating black holes, using flux criterion for remnant			
2.0	2, 4, 6	3.0–11.0	Charybdis
3.0	2, 4, 6	4.0–11.0	Charybdis
4.0	2, 4, 6	5.0–11.0	Charybdis
5.0	2, 4, 6	6.0–11.0	Charybdis
6.0	2, 4, 6	7.0–11.0	Charybdis
7.0	2, 4, 6	8.0–11.0	Charybdis
8.0	2, 4, 6	9.0–11.0	Charybdis
9.0	2, 4, 6	10.0, 11.0	Charybdis
Rotating black holes, boiling remnant			
2.0	2, 4, 6	3.0–11.0	Charybdis
3.0	2, 4, 6	4.0–11.0	Charybdis
4.0	2, 4, 6	5.0–11.0	Charybdis
5.0	2, 4, 6	6.0–11.0	Charybdis
6.0	2, 4, 6	7.0–11.0	Charybdis
7.0	2, 4, 6	8.0–11.0	Charybdis
8.0	2, 4, 6	9.0–11.0	Charybdis
9.0	2, 4, 6	10.0, 11.0	Charybdis
Rotating black holes, stable remnant			
2.0	2, 4, 6	3.0–11.0	Charybdis
3.0	2, 4, 6	4.0–11.0	Charybdis
4.0	2, 4, 6	5.0–11.0	Charybdis
5.0	2, 4, 6	6.0–11.0	Charybdis
6.0	2, 4, 6	7.0–11.0	Charybdis
7.0	2, 4, 6	8.0–11.0	Charybdis
8.0	2, 4, 6	9.0–11.0	Charybdis
9.0	2, 4, 6	10.0, 11.0	Charybdis

Table 4.4: Quantum black hole signal samples used in the analysis

M_D, TeV	n	M_{BH}, TeV	$Generator$
Quantum black holes – ADD model			
4.0	1–6	4.0–12.0	QBH
5.0	1–6	5.0–12.0	QBH
6.0	1–6	6.0–12.0	QBH
7.0	1–6	7.0–12.0	QBH
8.0	1–6	8.0–12.0	QBH
9.0	1–6	9.0–12.0	QBH
10.0	1–6	10.0–12.0	QBH
11.0	1–6	11.0, 12.0	QBH
12.0	1–6	12.0	QBH
Quantum black holes – RS model			
4.0	1	4.0–12.0	QBH
5.0	1	5.0–12.0	QBH
6.0	1	6.0–12.0	QBH
7.0	1	7.0–12.0	QBH
8.0	1	8.0–12.0	QBH
9.0	1	9.0–12.0	QBH
10.0	1	10.0–12.0	QBH
11.0	1	11.0, 12.0	QBH
12.0	1	12.0	QBH

Table 4.5: Stringball samples used in the analysis

M_D, TeV	n	M_S, TeV	M_{SB}, TeV	g_s	$Generator$
			String Balls		
1.4	2, 4, 6	1.1	3.0–11.0	0.4	Blackmax
1.6	2, 4, 6	1.3	3.0–11.0	0.4	Blackmax
2.1	2, 4, 6	1.7	3.0–11.0	0.4	Blackmax
1.64	6	1.1	5.5–10.0 in 0.5 TeV steps	0.2	Blackmax
1.49	6	1.1	5.0, 6.0, 7.0–10.0 in 0.5 TeV steps	0.3	Blackmax
1.89	6	1.5	5.0, 6.0, 7.0–10.0 in 0.5 TeV steps	0.4	Blackmax
2.38	6	2.0	5.0, 6.0, 7.0–10.0 in 0.5 TeV steps	0.5	Blackmax

CHAPTER 5: EVENT SELECTION

5.1 Trigger

Since a priori we do not know the exact final state, instead of triggering using single-object or multiobject triggers, we employ a trigger based on the total energy deposited in the detector in an event. For this purpose, a high-level trigger (HLT) selecting data events on the basis of a threshold on the scalar sum of object's transverse momenta (H_T) using objects reconstructed by particle flow (PF) algorithm (Beaudette; CMS Collaboration, 2010; 2011) is used, which is named as HLT_PFHTx, where x denotes the threshold on H_T (800 GeV in this analysis). The trigger is fully efficient for S_T above 1 TeV.

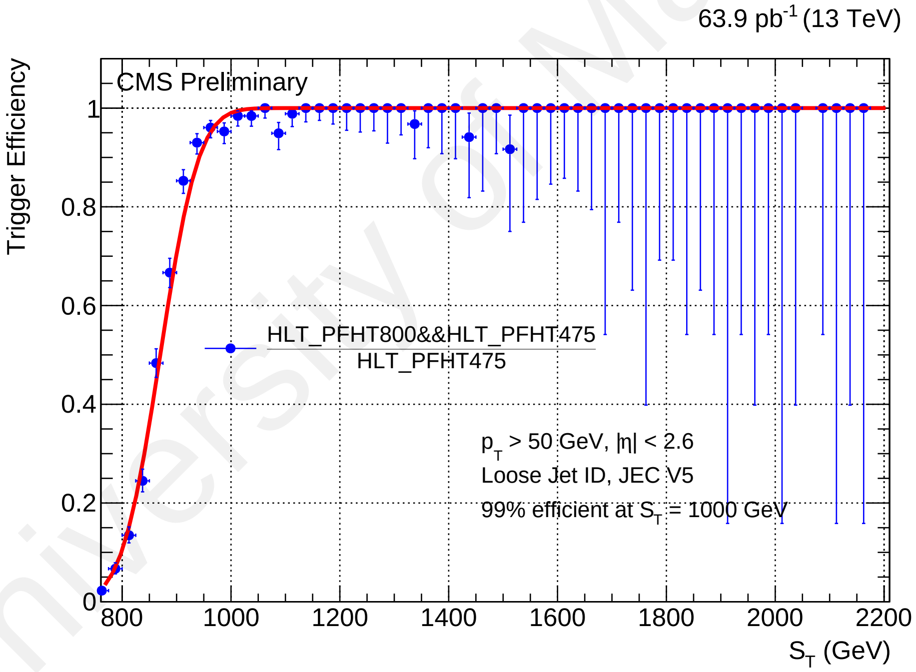

Figure 5.1: Trigger efficiency in data: Run2015D

5.2 Primary Vertex and Trigger Selections

Selected events are required to fire the HLT_PFHT800_v* trigger. At least one primary vertex is required to be reconstructed based on at least four tracks, requiring the track fit to have the number of degrees of freedom, $n_{dof} \geq 5$, with $|z_{PV}| < 24$ cm and $\rho_{PV} < 2$ cm, where $|z_{PV}|$ and ρ_{PV} are the vertex positions with respect to the nominal interaction point along the z axis and in the transverse plane (i.e., the plane perpendicular to the direction of the incoming proton beam), respectively.

5.3 Object definition

In this section, the final state objects are defined which will be later be used in this analysis for the kinematic study. The Particle-Flow (PF) algorithm (Beaudette; CMS Collaboration, 2010; 2011) is used for the reconstruction of all physics objects involved.

5.3.1 Muons

The selected muons must have a transverse momentum $p_t > 20$ GeV, be within the trigger acceptance ($|\eta| < 2.1$) and pass the muon quality criteria (muon ID) . The quality of the selected muon candidates has to meet the requirements of a "global muon" and should pass the PF muon identification i.e, "PF muon". Furthermore the quality of the global fit to the tracker trajectory and muon detector segments must satisfy the $\chi^2/\text{ndof} < 10$ requirement, which reduces the contribution coming from hadronic punch-through and muons that originate from hadrons decaying in flight. Muon candidates are also required to have at least two track segments in muon detectors and at least one valid hit in the muon detectors included in the global-muon track fit. A requirement on the transverse impact parameter (d_{xy}) and the longitudinal distance (d_z) of the muon candidate track with respect to the primary vertex is required to be < 2 mm and < 5 mm, respectively, to reduce contramination from cosmic muons. The muon candidate is also required to have a at least one hit in the pixel tracker and the total number hits in the tracker layers > 5.

Furthermore a cut on relative particle-flow isolation defined as:

$$I_{rel}^{\delta\beta-corr} = \frac{I^{ch.h} + \max\left(\left(I^{\gamma} + I^{n.h} - 0.5 \times \sum p_T^{PU}\right), 0\right)}{p_T} \tag{5.1}$$

is applied on the muon candidate with the so-called "Delta Beta" corrections. The variables $I^{ch.h}$, I^{γ}, and $I^{n.h}$ are the sums of the transverse energies deposited by charged hadrons coming from the pileup, photons, and neutral hadrons respectively, in a cone of size $\Delta R = 0.4$. The last term in the Eq.5.1 is defined as the sum of transverse momentum of all the tracks coming from additional pileup vertices. This is used to estimate an average contribution coming from neutral particles coming from pileup events by multiplying the sum by a factor of 0.5. We require $I_{rel} < 0.15$ for a muon candidate to be selected as a muon in this analysis.

5.3.2 Electrons and Photons

In this analysis the standard cut-based electron identification is adopted. (E. C. Based ID). The cut based ID is a simple to use and robust set of selection and identification criteria for the electron candidates, with standard working points provided by the EGamma group:

- Veto: This working point (WP) has an average efficiency of ~ 95% and can be used to veto any additional lepton comining in the selection.
- Loose: It has an average efficiency of ~ 90%.
- Medium: It has an average efficiency of ~ 80%.
- Tight: It has an average efficiency of ~ 70%.

In this analysis "Medium" working point (WP) is used for the cut based identification of electrons. Along with the "Relative isolation ($I_{rel}^{\rho-corr}$)" condition with Effective Area (EA) corrections for the pile-up.

$$I_{rel}^{\rho-corr} = \frac{I^{ch.h} + \max\left(\left(I^{\gamma} + I^{n.h} - \rho \times A\right), 0\right)}{p_T} \tag{5.2}$$

where ρ is the average energy of subtracted charged hadrons excluded from jet clustering and A is the area of the jet cone in the $\eta - \phi$ plane. An isolation cone of $\Delta R = 0.3$ is chosen for the reconstruction of electrons. The electrons passing the loose identification criterion are selected by the requirement $I_{rel}^{\rho-corr} < 0.1$. More details on the cut-based electron ID working points can be found at (E. C. Based ID).

Similarly for photons, a cut-based “medium" identification is used in the analysis, which requires photon candidates a required to satisfy a set of identification criteria:

- The transverse size of the electromagnetic cluster is required to be compatible with the one expected from prompt photons. In the case of photon candidates in the saturation region the requirement takes into account the induced distortion in the shape of the electromagnetic clusters.
- The ratio of hadronic to EM energy (H/E) is required to be below 0.05.
- The sum of the transverse momenta (ICh) of charged particle-flow hadron candidates contained in a cone of radius 0.3 in $\eta - \phi$ space is required to be below 5 GeV. Charged particle-flow candidates compatible with conversion tracks associated with the photon candidates are excluded from the sum.
- The sum of the transverse energy of the photon candidates contained in a cone of radius 0.3 in in $\eta - \phi$, corrected for pileup effects, is required to be below 2.5 GeV.
- Photon candidates associated with electron tracks incompatible with conversion tracks are removed.

In addition, the following isolation requirements are used. The ρ-corrected PF charged-hadron Isolation must satisfy $pfChargedHadronIso < 1.37$ GeV for the barrel and < 1.10 GeV for the endcap photons. The ρ-corrected PF neutral-hadron Isolation requirement depends on the p_T of the photon: $I^{n.h} < 1.06$ GeV $+ 0.014 p_T + 0.000019$ GeV$^{-1} {p_T}^2$

in the barrel and 2.69 GeV + 0.0139p_T + 0.000025 GeV^{-1}p_T^{2} in the endcaps. Finally the ρ-corrected PF photon Isolation requirement also depend on the photon p_T as: I^γ = 0.28 GeV + 0.0053p_T in the barrel and 0.39 GeV + 0.0034p_T in the endcaps.

Further details on the cut-based photon identification can be found in (P. C. Based ID).

5.4 Jets

Jets used in this analysis are reconstructed based on the PF candidates clustered with the anti-k_T algorithm with a distance parameter of 0.4. The jet energy is scaled by a factor that describes the detector response, depending on the transverse energy and the pseudorapidity of the jet. These corrections are derived using simulation and verified with 13 TeV collision data.

Jets selected for this analysis must to pass the following standard ("tight') quality requirements:

- Jets must have corrected p_T> 50 GeV and $|\eta|$ < 5.2;
- Charged-hadron subtraction (removal of charged hadrons from pileup);
- Number of jet constituents (i.e, PF objects used to form the jet) > 1;
- Neutral-hadron energy fraction: NHF < 0.90;
- Neutral EM energy fraction: NEM < 0.90;
- if $|\ \eta\ |$< 2.4, Charged EM energy fraction CEM < 0.90;
- if $|\ \eta\ |$< 2.4, Charged-hadron energy fraction CHF > 0;
- if $|\ \eta\ |$< 2.4, Neutral hadron energy fraction NHF > 0;
- Jet momentum fraction carried by a muon in the jet < 0.8.

5.5 Noise Filters

Standard event filters recommended by JetMET POG are employed to filter events with misreconstructed jets due to calorimeter noise, beam halo muons, or low-quality vertices are applied: (J. Pog)

- Hadron calorimeter barrel and endcap noise filter
- Hadron calorimeter barrel and endcap noise isolation filter
- Cathode strip chamber beam halo muon filter
- Low quality reconstructed vertex filter
- Electromagnetic calorimeter supercrystal noise filter

In very rare cases, a jet or a muon, coupled wit the particle-flow reconstruction, could mimic a jet signature, resulting in events with unphysically high amount of E_T^{miss}. (M. working group) While a dedicated filter to remove these events is being developed within the CMS, we impose an additional selection on $E_T^{miss}/S_T' < 0.5$, where S_T''s the S_T variable corrected for the E_T^{miss}, i.e. a sum of all energetic leptons, photons, and jets in the event. The value of the cutoff parameter was picked using the comparison of data and QCD simulation at relatively small values of S_T, and looking for any deviation from unity, as shown in Figure 5.2. The effects of tight jet ID and the E_T^{miss}/S_T' on the final selection are showed in Figure 5.3.

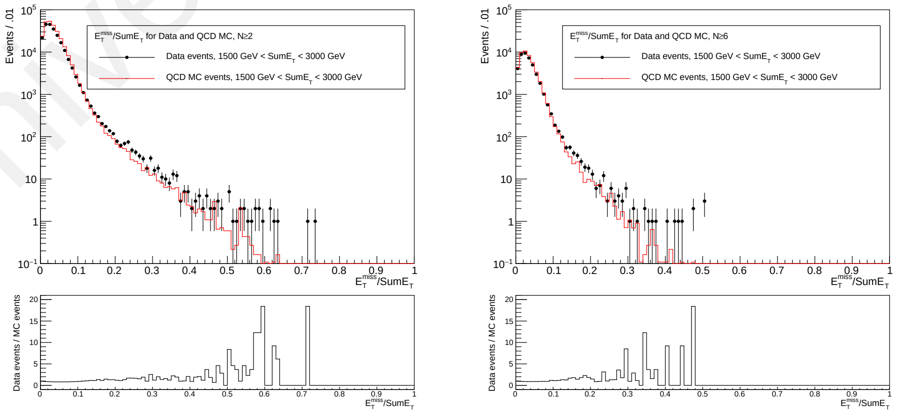

Figure 5.2: Plots of the E_T^{miss}/S_T' distributions and ratios in data and MC for events passing all other cuts besides the E_T^{miss}/S_T' cut, for events with (left) $N \geq 2$ and (right) $N \geq 6$

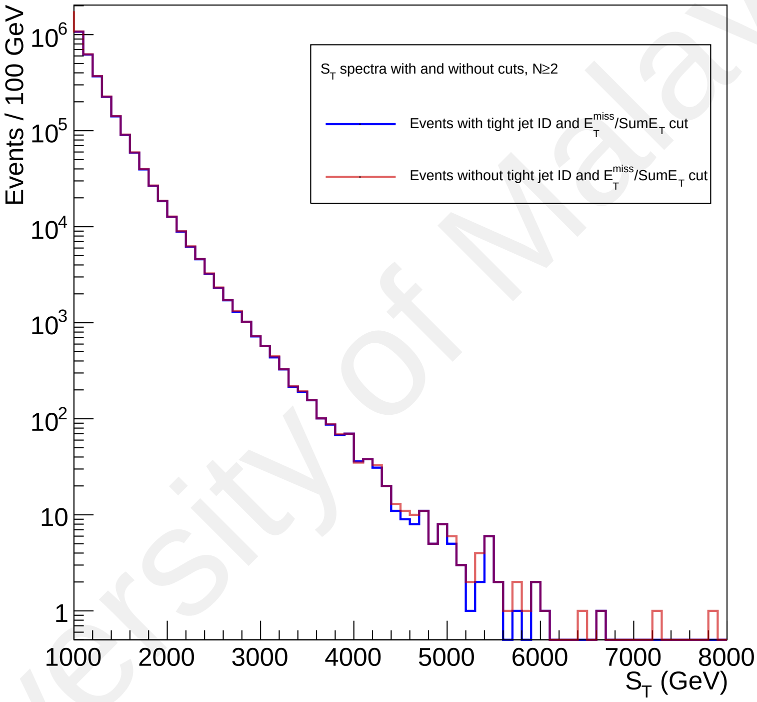

Figure 5.3: Plot of the S_T distributions for 2.2 fb^{-1} 25ns 2015 data where S_T is calculated using tight jet ID criteria with the E_T^{miss}/S_T' cut versus only the loose jet ID criteria (red) for events with $N \geq 2$

CHAPTER 6: BACKGROUND ESTIMATION

The main backgrounds in the analyzed final multiparticle state are: QCD multijet, V+jets (where V = W, Z), $\gamma + jet$, and $t\bar{t} + jets$ production, with the QCD multijet background being by far the dominant one. As indicated in Figure 6.6, the non-QCD background contribution to the total background is very small and therefore is neglected in the analysis. We also note an overall good agreement between data and MC background predictions for low-multiplicity data, as detailed in Figure 6.7. Nevertheless, we do not rely on the simulation of the QCD background at high jet multiplicity at all, so these plots only serve an illustration purpose.

The QCD multijet background estimation methods are based on data and stayed unchanged since (CMS Collaboration, 2010; 2011). The idea of the background estimation method is based on the fact that the shape of the tail of S_T distributions is invariant, up to a scaling factor, for different multiplicities. Consequently, this means that the shape of the background (also referred to as template) can be extracted from data with low multiplicities, and then rescaled to higher multiplicities.

The background template is obtained by fitting an ansatz function $\frac{P_0(1+x)^{P_1}}{x^{P_2+P_3\log(x)}}$ to the S_T distribution between 1400 and 2400 GeV for exclusive multiplicity $N = 2$ as shown in Figure 6.1. Any sizable contribution of new physics at these masses have been ruled out by dedicated Run 1 analyses, including earlier BH searches (CMS Collaboration, 2011; 2012; 2013). The fit uncertainty is estimated in the same manner as in (CMS Collaboration, 2010), which is determined by two additional functions $\frac{P_0}{(P_1+x)^{P_2}}$ and $\frac{P_0}{(P_1+P_2x+x^2)^{P_3}}$. The function (or piecewise defined function) yeilding the greatest difference from the main fit is used as the shape systematic uncertainty envelope, which is then symmeterized around the main fit making an uncertainty envelope. Figure 6.2 demonstrates the relative shape systematic uncertainty (black line) as a function of S_T. The shape systematic uncertainty is also indicated as the grey shaded band in Figures 6.8 and 6.9. Several more template functions used in the literature related to the fit of falling transverse momenta spectra and their generalizations were tested, but all alternative functions fall within the envelope given by the three template functions above. In addition, the effects of the uncertainties associated with the fit functions' parameters was investigated, and it ws found that varying each of the ansatz function's parameters by one standard deviation (as reported by the MINOS fitting algorithm) would yeild a function well within the uncertainty envelope given by the three template functions, as shown in Figure 6.10

The background template extracted by fitting the $N = 2$ S_T spectrum is normalized to obtain a background estimate for the S_T spectra at higher multiplicities, using normalization regions with the bounds that depend on the multiplicity. The choice of normalization regions is based on the studies of the S_T invariance in the QCD MC samples and are listed in Table 6.1. The lower bound of the normalization region is chosen to be above the turn-on of the multiplicity invariance (the background shape at large multiplicities deviates from that at $N = 2$ multiplicity below a certain threshold, which increases with the multiplicity, since the minimum possible value of S_T increases once we require more objects in the event). The upper bound is chosen so that the signal contamination in the normalization region is negligible for the signal with the BH masses above the Run 1 exclusion (~ 6 TeV), and so that the normalization region has reasonable statistics. The normalization scaling factors are calculated as the ratio of the events in the normalization regions (NR) for the inclusive multiplicities of $N \geq 2 \ldots 10$ to the exclusive multiplicity of $N = 2$.

We assign an additional uncertainty to address possible S_T noninvariance by estimating the difference between the background predictions based on $N = 2$ (default) and $N = 3$. Figure 6.3 shows the ratio of the background shapes obtained using these two exclusive multiplicities, which shows that it is flat. We conservatively assign an additional uncertainty of 5% to account for possible differences (which is a subdominant uncertainty in the high-S_T range relevant for the analysis).

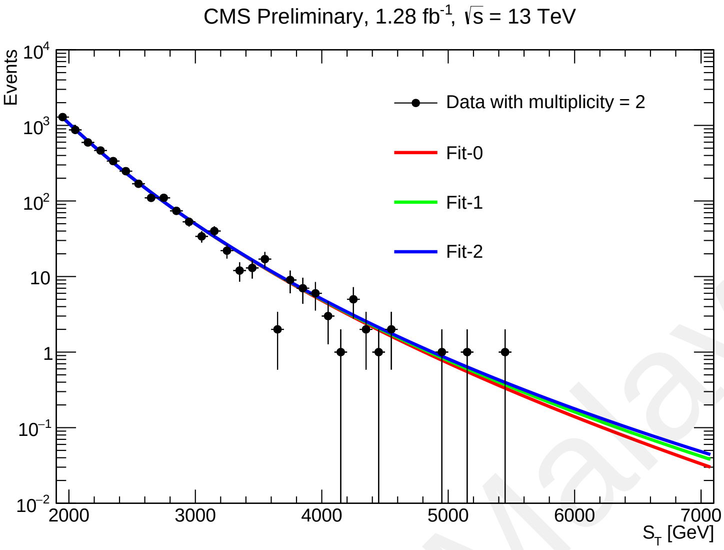

Figure 6.1: The S_T distribution of exclusive multiplicity of two is used as the background template. Three fitted functions (red, green, and blue) are overlayed on top the data (black points)

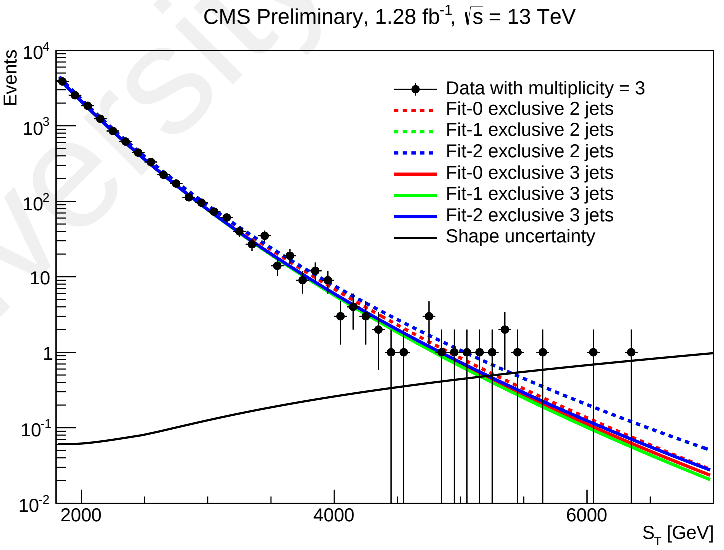

Figure 6.2: The relative shape systematic uncertainty is shown as a function of S_T. The dashed lines are the fitted functions from exclusive multiplicity of two, which are normalized to the number of events in exclusive multiplicity of three (black points), in 2000 GeV $< S_T <$ 2300 GeV range. The fitted functions of exclusive multiplicity of three are shown in solid lines

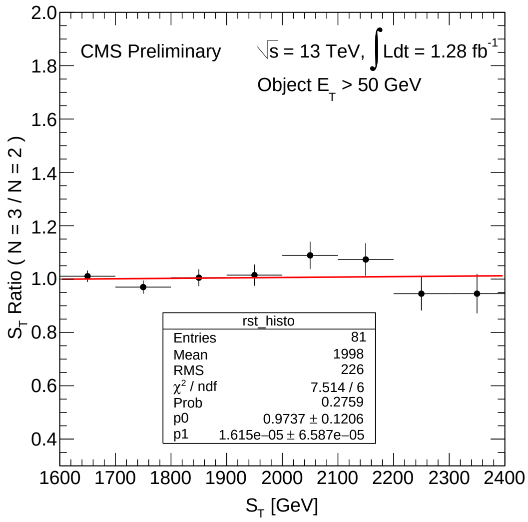

Figure 6.3: Ratio of the background predictions obtained from exclusive $N = 3$ and $N = 2$ S_T spectra

While we completely rely on data in predicting the dominant background in this search, we do qualify some of the assumption using QCD multijet MC simulation. We do not expect the simulation to reproduce all the fine details of data at high multiplicities, as even multileg LO MC generators, such as MadGraph are not versatile enough to properly simulate, e.g. 8-jet final state. Therefore, we use QCD simulation only as an auxiliary tool to qualitatively show that the S_T scaling holds well for high-multiplicity data and to estimate the turn-on curve of the S_T invariance, as we can only reliably predict the background on the plateau of this curve. Figures 6.4 and 6.5 show the ratio of the S_T distribution in both data and simulation for various inclusive multiplicities to the background shape obtained by fitting simulated $N = 2$ QCD multijet spectrum. These figures show that S_T invariance holds well in both data and simulation, and it also indicates that the turn-on is slower at higher multiplicities (as expected, given that higher number of objects correspond to higher S_T) and can be used to choose the optimal normalization regions for the background estimate.

Note that the features of S_T invariance have been studied in fine detail in the 8 TeV data.

Since the S_T spectrum of the QCD backgound is predicted to change in proportion to the logarithm of the center-of-mass energy, all the features thoroughly studied with the 8 TeV data are expected to survive for 13 TeV center-of-mass energy.

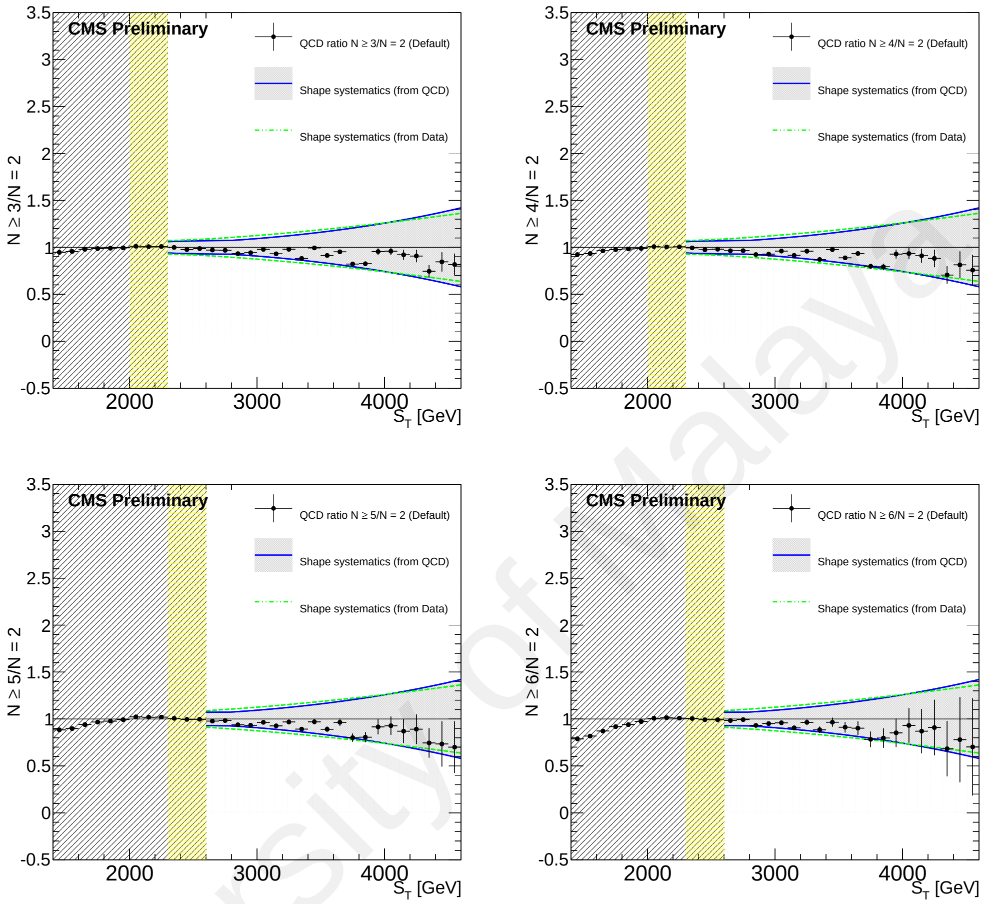

Figure 6.4: The ratio of the S_T spectrum in data (black points with error bars) and simulation (red points with error bars) to the simulated background fit for $N = 2$. The four panes correspond to inclusive multiplicities $N \geq 3 \ldots 6$

On the basis of shape invariance, the normalized shape of fit performed on multiplicity two is used to extract background from higher inclusive multiplicities $N \geq 3, \ldots, 10$. The background template of multiplicity two is normalized to higher multiplicities, which is based on a certain normalization region depending on the multiplicity. The choice of normalization regions based on the above MC study is given in Table 6.1. The normalization scaling factors are calculated as the ratio of the events in the normalization regions (NR) in the inclusive multiplicities of $N \geq 3, \ldots, 10$ to the exclusive multiplicity of $N = 2$. The

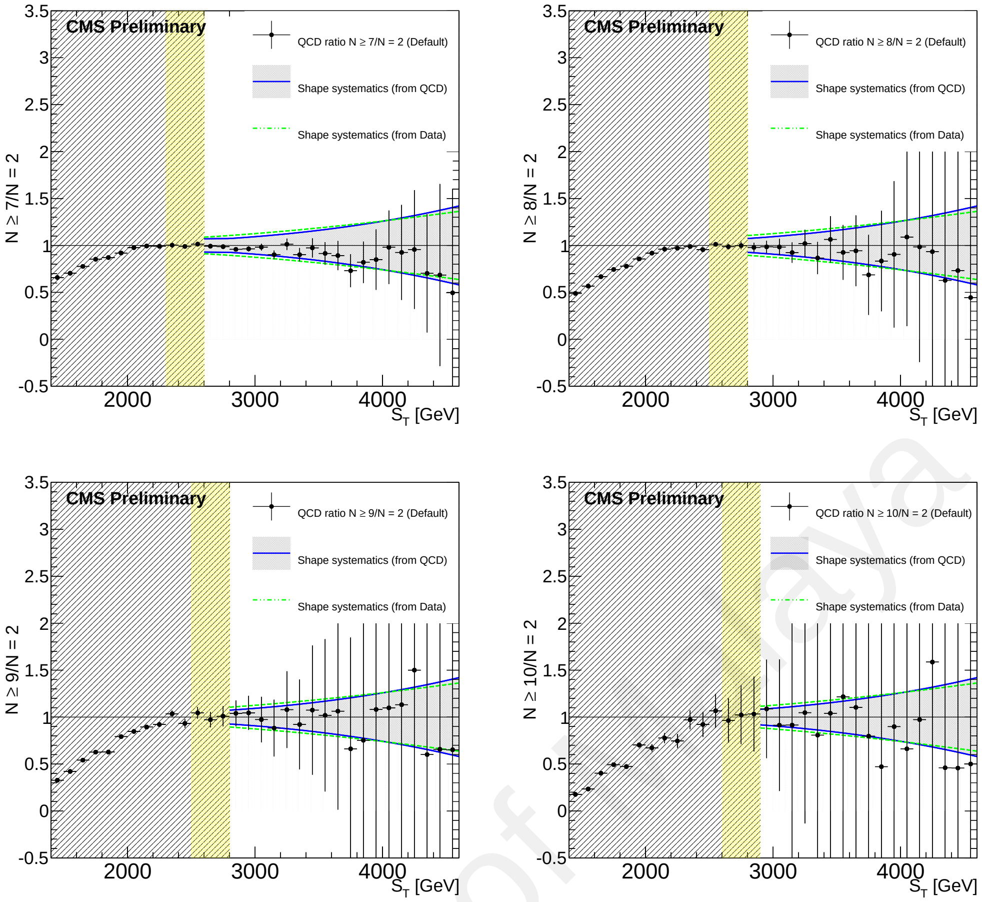

Figure 6.5: The ratio of the S_T spectrum in data (black points with error bars) and simulation (red points with error bars) to the simulated background fit for $N = 2$. The four panes correspond to inclusive multiplicities $N \geq 7 \ldots 10$

relative normalization scaling uncertainties are derived from the number of events in the NR, as $\frac{1}{\sqrt{N_{NR}}}$, where N_{NR} is a number of events in a normalization region.

The normalization regions with corresponding normalization scaling factors and uncertainties are shown in Table 6.1, for all the inclusive multiplicity cases.

Table 6.1: For the fitting region $1400 < S_T < 2400$ GeV, the normalization regions and corresponding normalization scaling factors and uncertainties ($\frac{1}{\sqrt{N_{NR}}}$, where N_{NR} is the number of events) for inclusive multiplicities, $N \geq 3, 4, \ldots 10$

Multiplity	Normalization Region [GeV]	Normalization Scaling
≥ 3	2000 – 2300	7.95± 0.06
≥ 4	2000 – 2300	5.90± 0.04
≥ 5	2300 – 2600	3.74± 0.14
≥ 6	2300 – 2600	2.02± 0.08
≥ 7	2300 – 2600	0.93± 0.04
≥ 8	2500 – 2800	0.412± 0.021
≥ 9	2500 – 2800	0.166± 0.008
≥ 10	2600 – 2900	0.657± 0.004

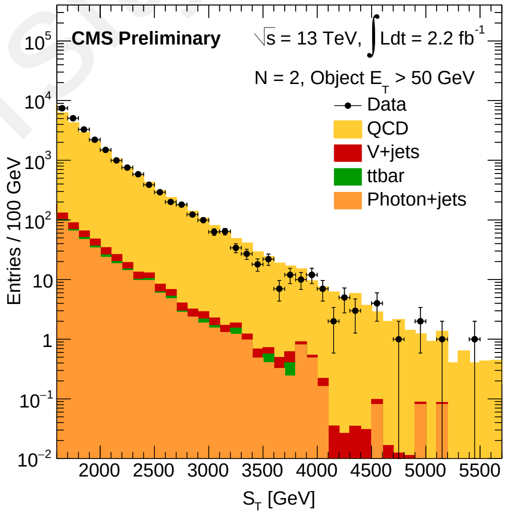

Figure 6.6: Contributions of the main QCD multijet background, as well as V+jets (where V = Z, W), $\gamma + jets$, and $t\bar{t} + jets$ backgrounds to the S_T distribution for multiplicity $N = 2$

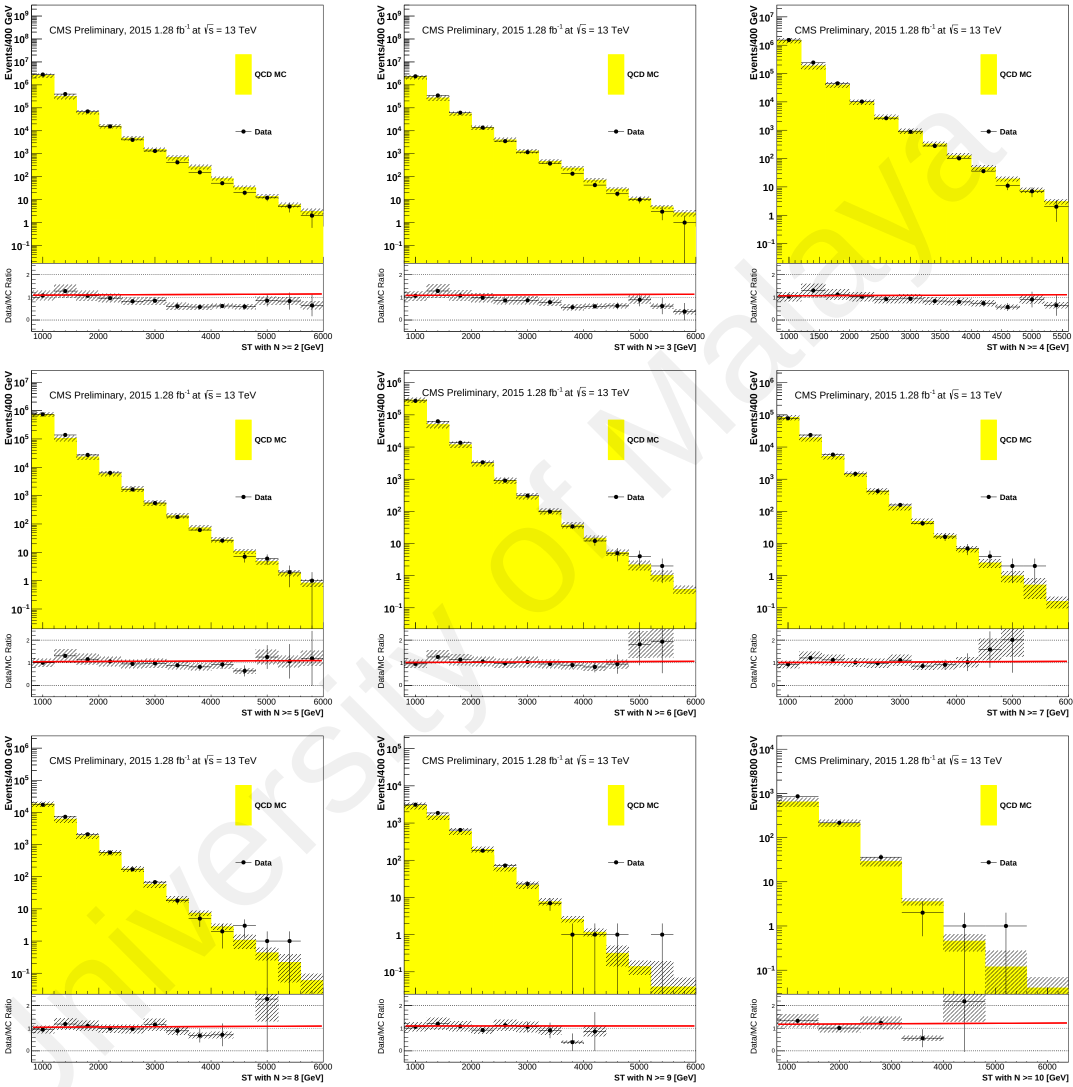

Figure 6.7: Contributions of the main QCD multijet background from the simulations with the data for various inclusive multiplicity bins

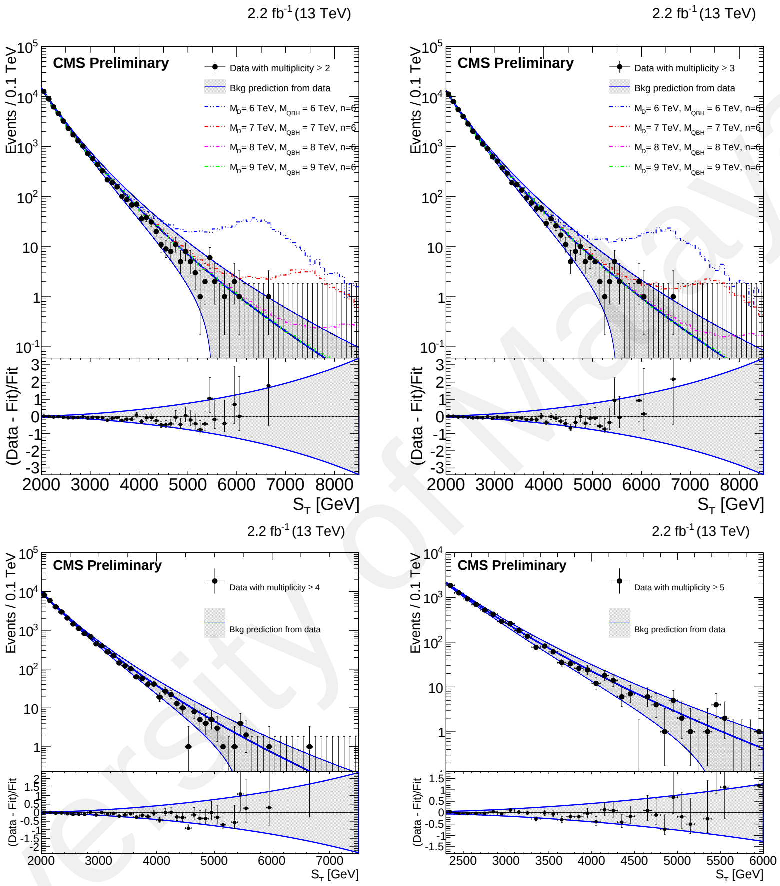

Figure 6.8: The distributions of the total transverse energy, S_T for inclusive multiplicities of objects (photons, muons, photons or jets) $N \geq 2, 3, 4, 5$. Observed data are shown by points with error bars, the solid blue lines along with the grey shaded band show the main background estimation (central blue line), along with the uncertainty band (outer blue lines). The deviation of the fit from the data is shown in the lower panes. The top two plots also show several quantum black hole signal points

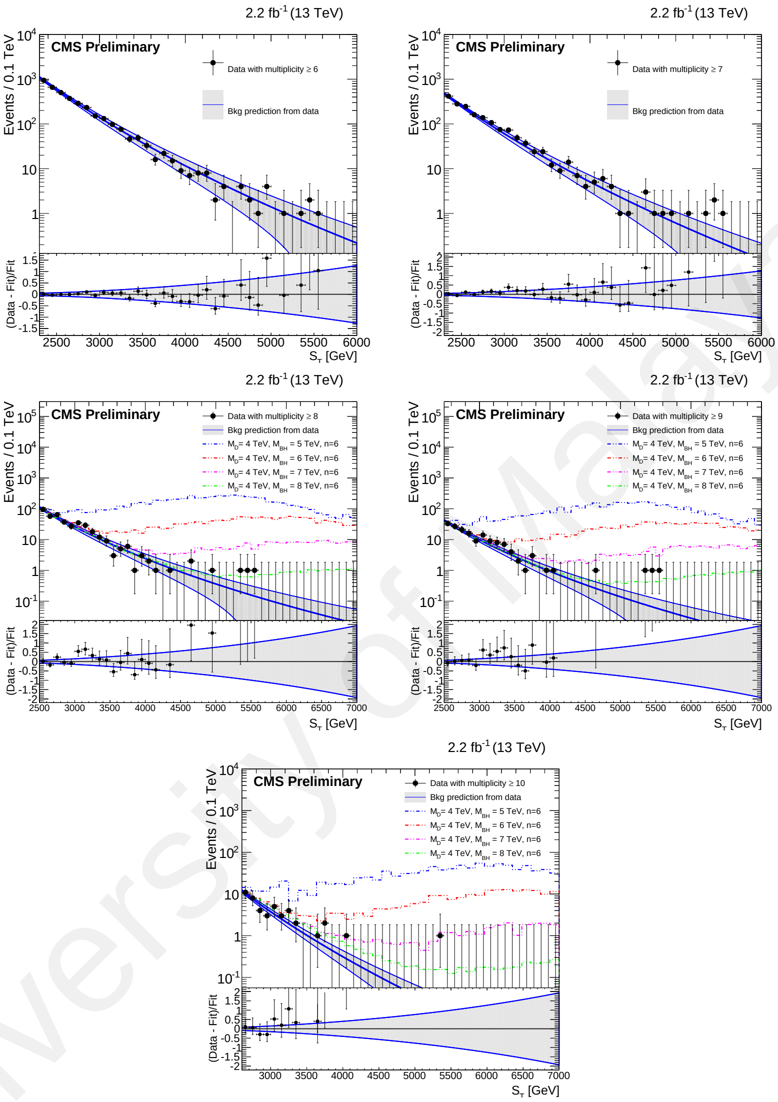

Figure 6.9: The distributions of the total transverse energy, S_T for inclusive multiplicities of objects (photons, muons, photons or jets) $N \geq 6, 7, 8, 9, 10$. Observed data are shown by points with error bars, the solid blue lines along with the grey shaded band show the main background estimation (central blue line), along with the uncertainty band (outer blue lines). The deviation of the fit from the data is shown in the lower panes. The bottom three plots also show several semiclassical black hole signal points

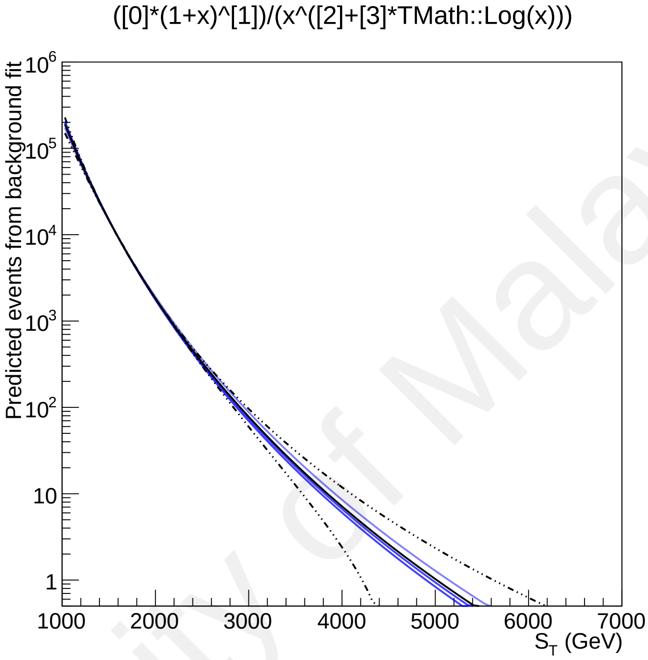

Figure 6.10: Plot of nominal background fit function (solid black), the background fit uncertainty envelope from fitting different fit functions and symmetrizing the outlying values about the background fit function (dotted black), as well as a plot of the nominal fit function with the shape parameters varied plus or minus their uncertainty as reported by the MINOS fitting algorithm (blue). Only one parameter at a time is changed ±sigma while the others are held at their nominal value. Note that the normalization parameter [0] was not considered here as normalization uncertainty is considered already–instead the normalization parameter was set for each varied function such that the normalization in the fit range was equal to that of the nominal fit function

CHAPTER 7: SYSTEMATIC UNCERTAINTIES

There are a few sources of systematic uncertainties in this Analysis: uncertainties due to reconstructed objects identification inefficiencies, energy scales, choice of parton density functions (PDF) libraries and sets, *etc*. In this Section we describe the most significant of them.

7.1 Parton distribution functions

Parton distribution functions give us the probability finding a f flavored parton with momentum x at a factorization scale Q and they could be expressed with the formula:

$$\frac{d\sigma}{dz}(pp \to X) = \sum_{i,j} PDF_{i,p}(x_1, f_1, Q) \otimes PDF_{j,p}(x_2, f_2, Q) \otimes \frac{d\sigma_{ij} \to X(Q^2)}{dz} \quad (7.1)$$

There are two possible sources of systematic uncertainties related to PDFs: an uncertainty due to choice of the PDF library and an uncertainty due to variations induced by the fluctuations of the PDF sets themselves within a specific PDF library. To estimate the PDF uncertainty on the acceptance, we relied on the reweighing method which relies on factorizing the PDF part in Equation 7.1. This way, we were able to calculate $2n + 1$ weights for each event using (CMS Collaboration, 2009; PDF4LHC Recommendations):

$$w^j = \frac{PDF^j(x_1, f_1, Q) \cdot PDF^j(x_2, f_2, Q)}{PDF^0(x_1, f_1, Q) \cdot PDF^0(x_2, f_2, Q)} \quad (7.2)$$

where $0 \leq j \leq 2n$.

The value of the acceptance is then calculated by using all w^0 weights and then all w^1 weights and so on. This results in $2n + 1$ different values of the acceptance. Then, using the master formula given in Eq. 7.3 and Eq. 7.4 we determine the uncertainty on the acceptance as an upward and downward fluctuation from the central value of acceptance.

$$\Delta X^{+}_{max} = \sqrt{\sum_{i=1}^{N}[max(X^{+}_{i} - X_0, X^{-}_{i} - X_0, 0)]^2} \tag{7.3}$$

and

$$\Delta X^{-}_{max} = \sqrt{\sum_{i=1}^{N}[max(X_0 - X^{+}_{i}, X_0 - X^{-}_{i}, 0)]^2} \tag{7.4}$$

where X_0 is the central value of acceptance, ΔX^{+}_{max} and ΔX^{-}_{max} are the up/down variations that correspond to PDF sets. Using the above mentioned procedure, the uncertainty on the acceptance is calculated for three PDF libraries (MSTW, CTEQ6.1, and CT10) for one of the benchmark models (nonrotating BlackMax black hole with $M_D = 3$ TeV, $M_{BH} = 5.5$ TeV, and $n = 2$). The uncertainty on the acceptance using the main PDF set MSTW2008 does not exceed 0.5%. On the other hand, the uncertainty on the acceptance using CTEQ6.1 is the largest and is up to 6%. To be conservative, we assign a total of 6% systematic uncertainty due to the choice of PDF sets on all signal samples. We note that the PDF4LHC recommends to use the Eq. 7.3.

7.2 Jet energy corrections

The jet energy scale (JES) uncertainty affects the signal acceptance. In order to account for this effect, the jet four momenta are shifted up and down by 1-σ of the JES uncertainty, which is a function of transverse mometum and pseudorapidity. The JES uncertainty depends on the M_{BH} and varies from < 1% up to 5% level. In this analysis, we assign a conservative value of systematic uncertainty due to JES to 5%.

The values of systematic uncertainties that are used in this Analysis are summarized in Table 7.1.

Table 7.1: Summary of systematic uncertainties

Uncertainty	**Effect on Signal Acceptance**	**Effect on Background**
Integrated Luminosity	±4.4%	±4.4%
Jet Energy Scale	±5%	–
PDF	±6%	–
Rescaling	–	±(0.7 – 6.1)%
Shape modeling	–	±(1 – 130)%, depends on the S_T value.

CHAPTER 8: LIMITS

We use the hybrid (LHC style) full (as opposed to an asymptotic) CL_S method (Junk, 1999; Read, 2002) with lognormal factors in the likelihood to constrain the nuisance parameters near their best estimated values to set limits. The limit calculation is performed using the Higgs combination tool (Higgs analysis guide). We compared the results of full CL_S calculations with those from asymptotic CL_S calculations and found them to be identical within the uncertainties up to $S_T^{min} \sim 4000$ GeV.. For higher S_T values, when the number of events above the S_T threshold becomes small, full CL_S calculations give up to 40% higher cross section limit. Therefore, we used full CL_S method to calculate the limits for this analysis.

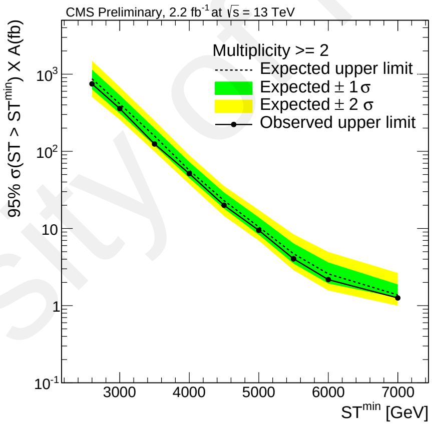

Figure 8.1: Model-independent upper limits on the cross section times acceptance for an exclusive multiplicity $N = 2$. Observed (expected) limits are shown as blue solid line (red dotted line)

The main result of this analysis is a set of model-independent limits on $\sigma \times A$ (signal cross section times acceptance) in inclusive $N \geq N^{min}$ final states, as a function of the minimum S_T requirement, S_T^{min}. These limits can then be translated into limits on the minimal black hole mass in a variety of models or on any other signal resulting in a multiobject final state. We start with the special case of an exclusive multiplicity $N = 2$ limit for S_T^{min} beyond the background fit region, which could be used for QBH and other

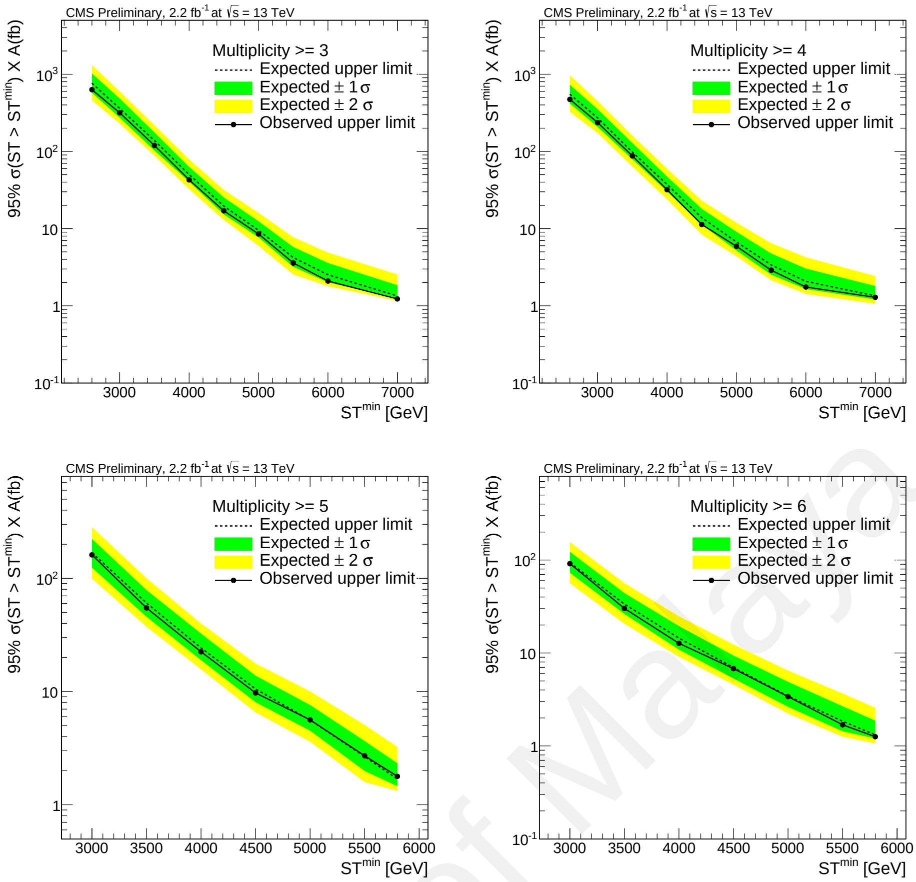

Figure 8.2: Model-independent upper limits on the cross section times acceptance for four sets of inclusive multiplicity thresholds: a) $N \geq 3$, b) $N \geq 4$, c) $N \geq 5$, and d) $N \geq 6$. Observed (expected) limits are shown as blue solid line (red dotted line)

low-multiplicity model interpretation. Here the background estimate comes from simple extrapolation of the fitted function beyond the fit range. The model-independent limit at a 95% confidence level (CL) are based on a simple counting experiment for $S_T > S_T^{min}$. This limit at a 95% CL is shown in Figure 8.1. Similar model-independent limits for $N \geq N^{min}$ and $S_T > S_T^{min}$ and presented in Figures 8.2, 8.3 for $N^{min} = 5\ldots10$. When computing the limits, we use systematic uncertainties applicable to the black hole signals, as documented in Chapter 7, as we expect them to apply for large variety of multijet signal models. These limits on the cross section times acceptance approach 2 fb at high values of S_T.

We proceed with the conversion of the model-independent limits into limits on minimum BH mass in two benchmark models: semiclassical nonrotating BHs evaporating without

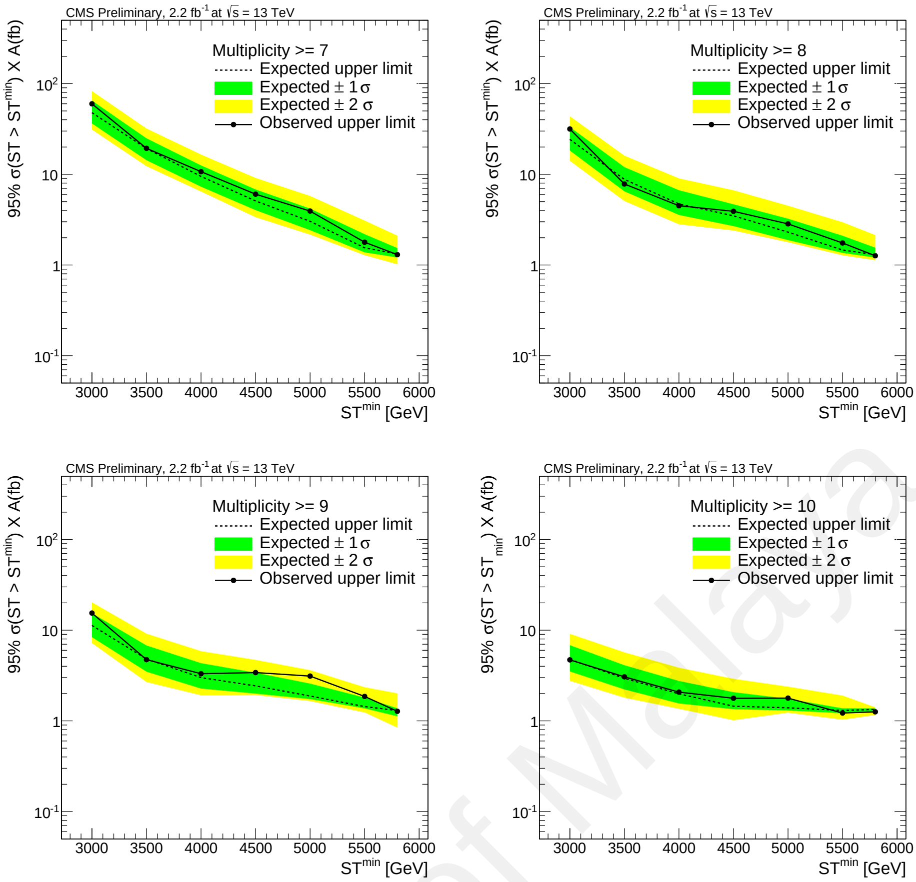

Figure 8.3: Model-independent upper limits on the cross section times acceptance for four sets of inclusive multiplicity thresholds: a) $N \geq 7$, b) $N \geq 8$, c) $N \geq 9$, and d) $N \geq 10$. Observed (expected) limits are shown as blue solid line (red dotted line)

remnant formation and quantum black holes. These models are representative of a larger class of models studied in the 8 TeV publication (CMS Collaboration, 2013). The semiclassical BH model used, corresponds to the number of extra dimensions $n = 6$ and the fundamental Planck scale value $M_D = 4$ TeV. The QBH model studied also corresponds to $n = 6$ and uses the minimum BH mass equal to the Planck scale, $M_D = M_{BH}^{min}$ assumption.

As an example of exclusion, on Figure 8.6 (top) we show the simulated semiclassical black hole signal for $M_D = 4$ TeV, $n = 6$, for the minimum BH masses of 5, 6, and 7 TeV, together with the background prediction for $N \geq 8$ as a function of S_T. It's clear from the plot that we exclude all three black hole masses with a present analysis. To quantify the exclusion, we show the cross section times acceptance for additional points with the minimum BH masses of 8–11 TeV on Figure 8.6. Comparison of these cross sections times acceptance as functions of S_T^{min} with the expected model-independent limits from from Figure 8.3 for $N \geq 8$ is shown in Figure 8.5 (left). We can now compute the optimal S_T^{min} selection as a function of the minimum BH mass, using the Z_{Bi} test statistic (Cousins et al., 2008), for each signal point, as shown in Figure 8.5 (right) in blue line.

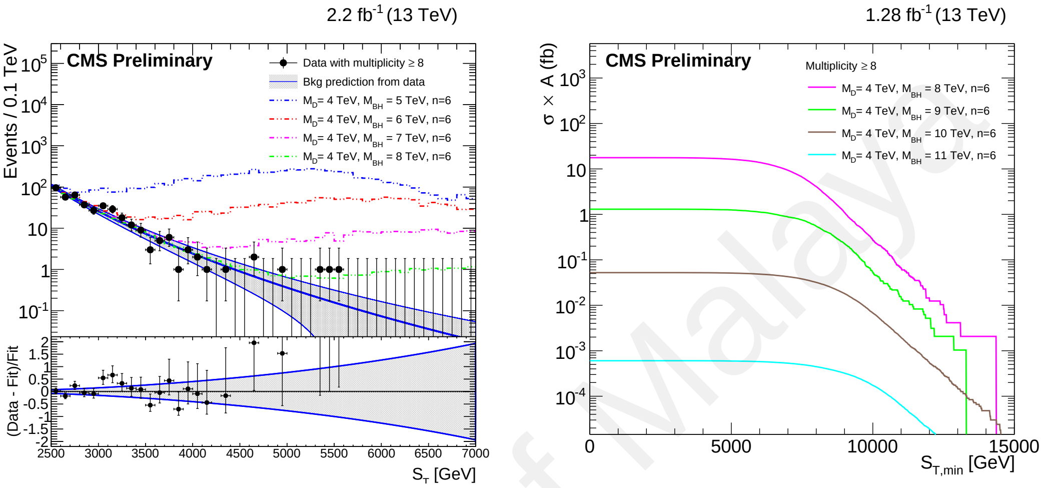

Figure 8.4: (left) The S_T spectrum for $N \geq 8$ inclusive multiplicity, with the three signal points overlaid. (right) Cross section times acceptance $\sigma \times A$, in pb, for the four signal points with the minimum BH mass of 8–11 TeV

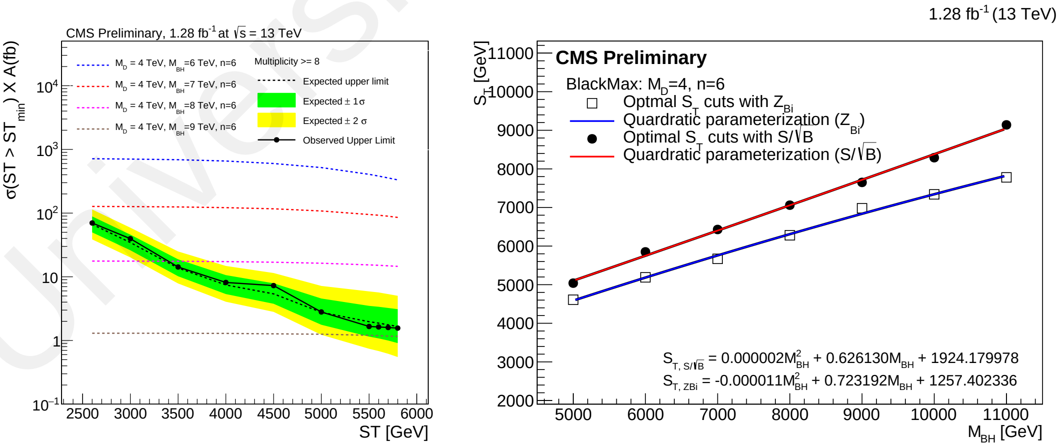

Figure 8.5: (left) Model-independent limit for $N \geq 3$ with the BH signal cross section times acceptance overlayed. (right) Optimal S_T^{min} requirement as a function of minimum BH mass for the $M_D = 4$ TeV, $n = 6$ nonrotating semiclassical BH model

Following the procedure as in the example above, in Figure 8.6 (top), we show the expected and observed 95% CL upper limits on the cross section at these optimal values of

S_T^{min} and N^{min}, as well as the production cross section times acceptance, as a function of the minimum BH mass. The intersect of the theoretical cross section with the expected (observed) limit curve gives and expected (observed) lower 95% CL limit set by the present analysis on the minimum BH mass for this model line; in this case both expected and observed limit are at 8.7 TeV. For the QBH model, the best sensitivity is achieved either for $N \geq 2$ or $N \geq 3$, and the two choices have almost the same sensitivity. To be completely orthogonal to the $N = 2$ multiplicity sample used to determine the background prediction, we chose $N \geq 3$ to set limits on this model. Figure 8.6 (bottom) shows the upper limits on the cross section compared with the theoretical prediction for the QBH model. The search excludes quantum black holes with $M_{BH}^{min} = M_D = 8$ TeV. Both these results extend significantly the sensitivity of Run 1 searches with the limits in the 5.5–6.0 TeV range, and are very similar to 13 TeV limits set by the ATLAS Collaboration (ATLAS Collaboration, 2015).

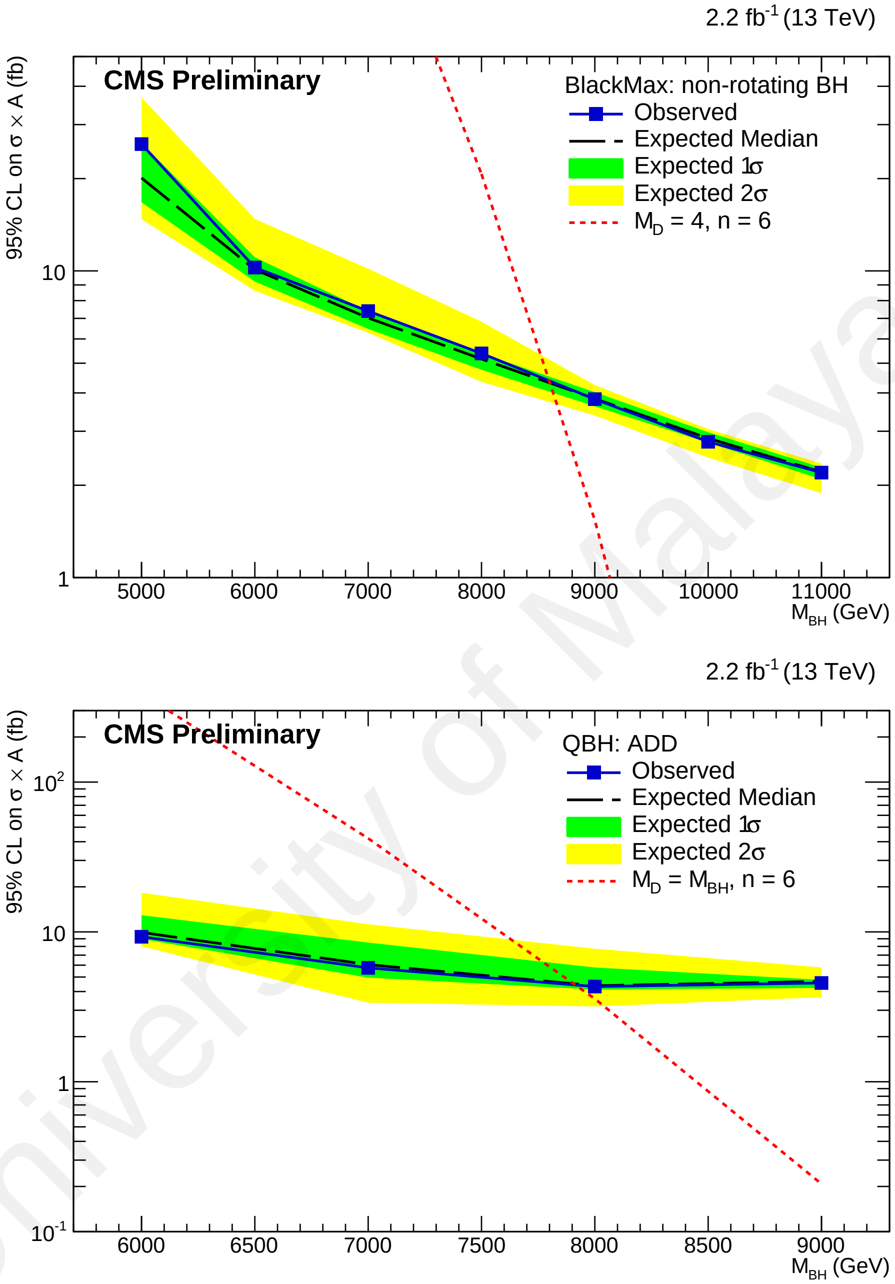

Figure 8.6: (top) Observed and expected upper 95% CL cross section times acceptance limits overlaid with the predicted values for a semiclassical BH with $M_D = 4$ TeV, $n = 6$, and varying M_{BH}^{min}, at the multiplicity and S_T^{min} values maximizing the Z_{Bi} test statistic. Depending on the signal point, optimal sensitivity is achieved for $N \geq 9$ or 10. (bottom) Same for a quantum BH model with $M_{BH}^{min} = M_D$; in this case the limits come from the $N \geq 3$ spectrum, which provides optimal sensitivity

CHAPTER 9: CONCLUSION AND DISCUSSION

9.1 Event Candidates

The event displays for three high-S_T candidates with large multiplicity are shown in Figures 9.1–9.3. The main parameters of these events are listed in Table 9.1.

Table 9.1: Parameters of three high-S_T and high-multiplicity black hole candidate events

S_T, TeV	N	E_T^{miss}, TeV	$Jet\ p_T$'s, TeV
		Run 260627, Event 2097040310	
6.67	4	0.11	2.63, 2.49, 1.17, 0.27
		Run 259685, Event 155512460	
5.56	9	0.01	1.96, 1.65, 0.58, 0.41, 0.37, 0.17, 0.14, 0.13, 0.12
		Run 257645, Event 1610868539	
5.35	12	0.12	1.80, 0.88, 0.54, 0.40, 0.37, 0.36, 0.36, 0.26, , 0.09, 0.07, 0.07, 0.05

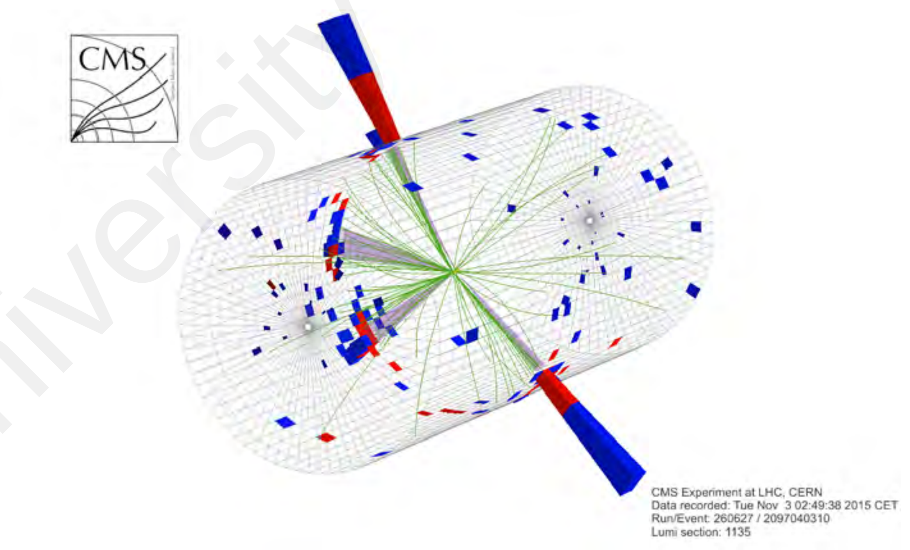

Figure 9.1: Event display for a black hole candidate collected in Run 260627, Event 2097040310. This event has 4 jets, S_T of 6.67 TeV, E_T^{miss} of 110 GeV, and the multiplicity $N = 4$

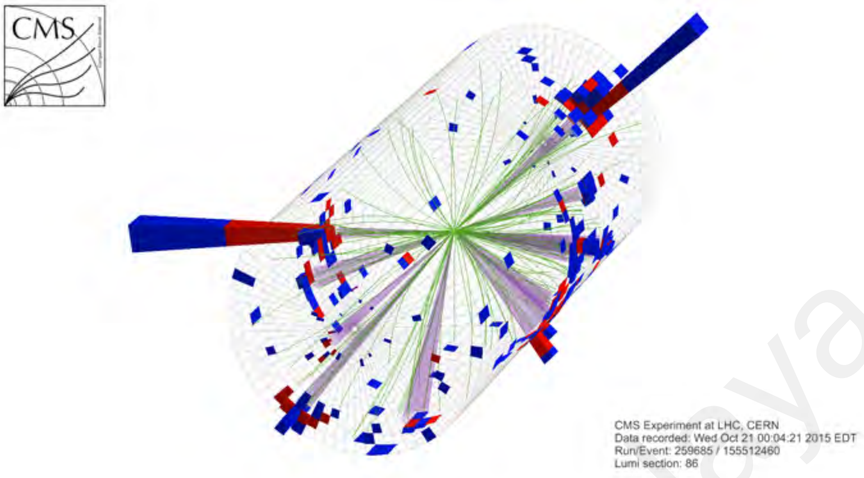

Figure 9.2: Event display for a black hole candidate collected in Run 259685, Event 155512460. This event has 9 jets, S_T of 5.56 TeV, E_T^{miss} of 8.4 GeV, and the multiplicity $N = 9$

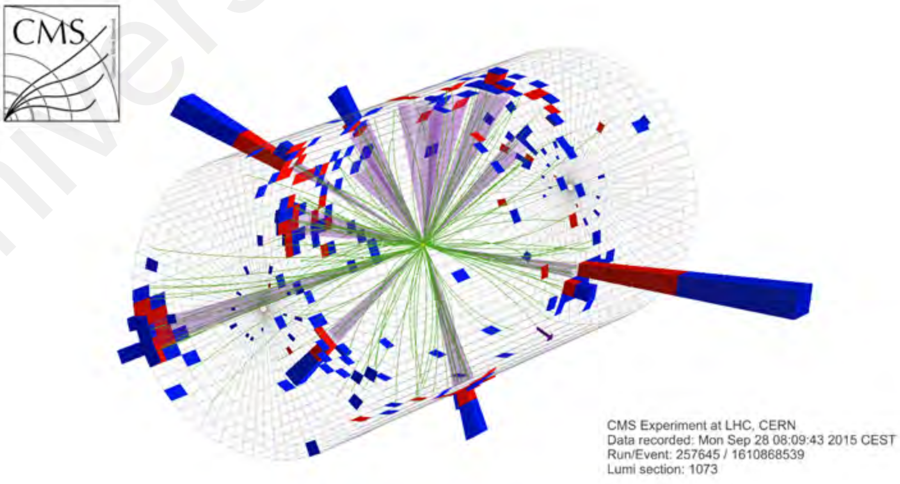

Figure 9.3: Event display for a black hole candidate collected in Run 257645, Event 1610868539. This event has 12 jets, S_T of 5.48 TeV, E_T^{miss} of 120 GeV, and the multiplicity $N = 12$

9.2 Summary

To conclude with, we have searched for microscopic black holes in $1.28 \pm 0.06\ fb^{-1}$ of 13 TeV pp collision data collected with the CMS detector as one of the possible solutions to the hierarchy problem. To have a more realistic estimate of the QCD multijet background, we have used a data-driven technique that allows one to use low multiplicity S_T distribution shape and extrapolate it to the final selection sample. Comparing the S_T distribution in data with that from the backgrounds, we set model-independent cross section 95% CL limits. These limits are roughly 2 fb at high values of S_T. Adding acceptance values for particular signal models to the equation, we set the 95% CL lower (upper) limits on the minimum semiclassical black hole mass in the 8.6 TeV range, thus significantly expanding previous limits coming from the LHC Run 1 data.

REFERENCES

Ackerman, L., Buckley, M. R., Carroll, S. M., Kamionkowski, M. (2009). Dark matter and dark radiation. *Physical Review D, 79*(2), 023519.

Adler, R. J., Chen, P., Santiago, D. I. (2001). The generalized uncertainty principle and black hole remnants. *General Relativity and Gravitation, 33*(12), 2101-2108.

Ali, A. F., Das, S., Vagenas, E. C. (2011). Proposal for testing quantum gravity in the lab. *Physical Review D, 84*(4), 044013.

Amati, D., Ciafaloni, M., Veneziano, G. (1989). Can spacetime be probed below the string size?. *Physics Letters B, 216*(1-2), 41-47.

Amelino-Camelia, G. (2002). Relativity in spacetimes with short-distance structure governed by an observer-independent (Planckian) length scale. *International Journal of Modern Physics D, 11*(01), 35-59.

Amelino-Camelia, G., Mandanici, G., Procaccini, A., Kowalski-Glikman, J. (2005). Phenomenology of doubly special relativity. *International Journal of Modern Physics A, 20*(26), 6007-6037.

Anchordoqui, L. A., Goldberg, H., Shapere, A. D. (2002). Phenomenology of Randall-Sundrum black holes. *Physical Review D, 66*(2), 024033

Antoniadis, I., Arkani-Hamed, N., Dimopoulos, S., Dvali, G. (1998). New dimensions at a millimeter to a Fermi and superstrings at a TeV. *Physics Letters B, 436*(3), 257-263.

Argyres, P. C., Dimopoulos, S., March-Russell, J. (1998). Black holes and sub-millimeter dimensions. *Physics Letters B, 441*(1), 96-104.

Arkani–Hamed, N., Dimopoulos, S., Dvali, G. (1998). The hierarchy problem and new dimensions at a millimeter. *Physics Letters B, 429*(3), 263-272. ; Antoniadis, I., Arkani-Hamed, N., Dimopoulos, S., Dvali, G. (1998). New dimensions at a millimeter to a Fermi and superstrings at a TeV. *Physics Letters B, 436*(3), 257-263.; Arkani-Hamed, N., Dimopoulos, S., Dvali, G. (1999). Phenomenology, astrophysics, and cosmology of theories with submillimeter dimensions and TeV scale quantum gravity. *Physical Review D, 59*(8), 086004.

ATLAS, C., (2012). Search for TeV-scale gravity signatures in final states with leptons and jets with the ATLAS detector at. *Physics Letters B, 716,* 122-141.

ATLAS, C., Aad, G., Abbott, B., Abdallah, J., Khalek, S. A., Abdinov, O., Aben, R., ... Abreu, H. (2014). Search for microscopic black holes and string balls in final states with leptons and jets with the ATLAS detector at s= 8 TeV. *Journal of High Energy Physics, 2014*(8), 103.

ATLAS, C., Beck, H. P., Cervelli, A., Ereditato, A., Haug, S., Kabana, S., ... Stucci, S. (2015). Search for low-scale gravity signatures in multi-jet final states with the ATLAS detector at s= 8 TeV. *Journal of High Energy Physics, 7*(7), 32.

ATLAS C., Aad, G., Abbott, B., Abdallah, J., Abdinov, O., Abeloos, B., Aben, R., ... Abreu, R. (2016). Search for strong gravity in multijet final states produced in pp collisions at s= 13 TeV using the ATLAS detector at the LHC. *Journal of High Energy Physics, 2016*(3), 26.

E. C. based ID. https://twiki.cern.ch/twiki/bin/view/CMS/CutBasedElectronIdentificationRun2

P. C. based ID. https://twiki.cern.ch/twiki/bin/view/CMS/CutBasedPhotonIdentificationRun2

Barbieri, R., Giudice, G. F. (1988). Upper bounds on supersymmetric particle masses. *Nuclear Physics B, 306*(1), 63-76.

J.Bardeen, J. M., Carter, B., Hawking, S. W. (1973). The four laws of black hole mechanics. *Communications in Mathematical Physics, 31*(2), 161-170.

Beaudette, F. (2010). *Performance of the particle flow algorithm in CMS* (No. CMS-CR-2010-276).

Bekenstein, J. D. (1973). Black holes and entropy. *Physical Review D, 7*(8), 2333.

Bekenstein, J. D. (1974). Generalized second law of thermodynamics in black-hole physics. *Physical Review D, 9*(12), 3292.

Berezhiani, Z., Comelli, D., Villante, F. L. (2001). The early mirror universe: inflation, baryogenesis, nucleosynthesis and dark matter. *Physics Letters B, 503*(3), 362-375.

Berezhiani, Z. G., Dolgov, A. D., Mohapatra, R. N. (1996). Asymmetric inflationary reheating and the nature of mirror universe. *Physics Letters B, 375*(1-4), 26-36.

Calmet, X., Gong, W., Hsu, S. D. (2008). Colorful quantum black holes at the LHC. *Physics Letters B, 668* (1), 20-23.

Amelino-Camelia, G. (2002). Relativity in spacetimes with short-distance structure governed by an observer-independent (Planckian) length scale. *International Journal of Modern Physics D, 11*(01), 35-59.

Carlip, S. (1999). Black hole entropy from conformal field theory in any dimension. *Physical Review Letters, 82*(14), 2828.

Chen, P., Adler, R. J. (2003). Black hole remnants and dark matter. *Nuclear Physics B-Proceedings Supplements, 124,* 103-106.

Chuzhoy, L., Kolb, E. W. (2009). Reopening the window on charged dark matter. *Journal of Cosmology and Astroparticle Physics, 2009*(07), 014.

CMS C. (2009). Parton Distribution Uncertainty Determination within CMSSW. *CMS Analysis Note AN-2009,* 048.

CMS C. (2010). Searches for Black Holes in pp Collisions ats = 7 TeV at the LHC. *CMS Analysis NoteAN-2010,* 313.

CMS C., Khachatryan, V., Sirunyan, A. M., Tumasyan, A., Adam, W., Bergauer, T., Dragicevic, M., ... Ghete, V. M. (2011). Search for microscopic black hole signatures at the Large Hadron Collider. *Physics Letters B, 697*(5), 434-453.

CMS C., Chatrchyan, S., Khachatryan, V., Sirunyan, A. M., Tumasyan, A., Adam, W., Aguilo, E., ... Friedl, M. (2013). Search for narrow resonances and quantum black holes in inclusive and b-tagged dijet mass spectra from pp collisions at $\sqrt{s}$ = 7TeV. *Journal of High Energy Physics, 2013*(1), 13.

CMS C., (2015). Search for stealth supersymmetry in events with jets, either photons or leptons, and low missing transverse momentum in pp collisions at 8 TeV. *Physics Letters B, 743,* 503-525.

Cousins, R. D., Linnemann, J. T., Tucker, J. (2008). Evaluation of three methods for calculating statistical significance when incorporating a systematic uncertainty into a test of the background-only hypothesis for a Poisson process. *Nuclear Instruments and Methods in Physics Research Section A: Accelerators, Spectrometers, Detectors and Associated Equipment, 595*(2), 480-501.

Dai, D. C., Freese, K., Stojkovic, D. (2009). Constraints on dark matter particles charged under a hidden gauge group from primordial black holes. *Journal of Cosmology and Astroparticle Physics, 2009*(06), 023.

Das, S., Vagenas, E. C. (2008). Universality of quantum gravity corrections. *Physical Review Letters, 101*(22), 221301.

Dimopoulos, S., Landsberg, G. (2001). Black holes at the large hadron collider. *Physical Review Letters, 87* (16), 161602.

Dimopoulos, S., Emparan, R. (2002). String balls at the LHC and beyond. *Physics Letters B, 526*(3), 393-398.

Bambi, C., Dolgov, A. D., Freese, K. (2007). Baryogenesis from gravitational decay of TeV particles in theories with low scale gravity. *Journal of Cosmology and Astroparticle Physics, 2007*(04), 005.

Emparan, R., Horowitz, G. T., Myers, R. C. (2000). Black holes radiate mainly on the brane. *Physical Review Letters, 85*(3), 499.

Feng, J. L., Kumar, J. (2008). Dark-matter particles without weak-scale masses or weak interactions. *Physical Review Letters, 101*(23), 231301.

Foot, R., Volkas, R. R. (2004). Spheroidal galactic halos and mirror dark matter. *Physical Review D, 70*(12), 123508.

Frolov, A. V., Kristjánsson, K. R., Thorlacius, L. (2005). Semiclassical geometry of charged black holes. *Physical Review D, 72*(2), 021501.

Geant4 Collaboration., Ivanchenko, V. N., (2003). Geant4 toolkit for simulation of HEP experiments. *Nuclear Instruments and Methods in Physics Research Section A: Accelerators, Spectrometers, Detectors and Associated Equipment, 502*(2), 666-668.

Ghosh, S. G., Papnoi, U. (2014). Spinning higher dimensional Einstein–Yang–Mills black holes. *The European Physical Journal C, 74*(8), 3016.

Giddings, S. B., Thomas, S. (2002). High energy colliders as black hole factories: The end of short distance physics. *Physical Review D, 65*(5), 056010.

Gingrich, D. M. (2010). Quantum black holes with charge, color and spin at the LHC. *Journal of Physics G: Nuclear and Particle Physics, 37* (10), 105008.; Gingrich, D. M. (2010). Monte Carlo event generator for black hole production and decay in proton–proton collisions–QBH version 1.02. *Computer Physics Communications, 181*(11), 1917-1924.

Glashow, S. L. (1961). Partial-symmetries of weak interactions.*Nuclear Physics, 22*(4), 579-588.

Hagedorn, R. (1965). Statistical thermodynamics of strong interactions at high energies. *Nuovo Cimento Supplemento, 3(CERN-TH-520),* 147-186.

Harland-Lang, L. A., Martin, A. D., Motylinski, P., Thorne, R. S. (2015). Parton distributions in the LHC era: MMHT 2014 PDFs. *The European Physical Journal C, 75*(5), 204.

Harris, C. M., Richardson, P., Webber, B. R. (2003). CHARYBDIS: a black hole event generator. *Journal of High Energy Physics, 2003*(08), 033.

Hawking, S. W. (1971). Gravitational radiation from colliding black holes. *Physical Review Letters, 26*(21), 1344.

Hawking, S. W. (1975). Particle creation by black holes. *Communications in Mathematical Physics, 43*(3), 199-220.

Hinrichsen, H., Kempf, A. (1996). Maximal localization in the presence of minimal uncertainties in positions and in momenta. *Journal of Mathematical Physics, 37*(5), 2121-2137.

Hossenfelder, S., Bleicher, M., Hofmann, S., Ruppert, J., Scherer, S., Stöcker, H. (2003). Signatures in the Planck regime. *Physics Letters B, 575*(1), 85-99.

Hooper, D., Zurek, K. M. (2008). Natural supersymmetric model with MeV dark matter. *Physical Review D, 77*(8), 087302.

Huh, J. H., Kim, J. E., Park, J. C., Park, S. C. (2008). Galactic 511 keV line from MeV millicharged dark matter. *Physical Review D, 77*(12), 123503.

Ida, D., Oda, K. Y., Park, S. C. (2003). Rotating black holes at future colliders: Greybody factors for brane fields. *Physical Review D, 67*(6), 064025.

Jiang, Q. Q., Wu, S. Q. (2007). Hawking radiation from rotating black holes in anti-de Sitter spaces via gauge and gravitational anomalies. *Physics Letters B, 647*(2), 200-206.

Junk, T. (1999). Confidence level computation for combining searches with small statistics. *Nuclear Instruments and Methods in Physics Research Section A: Accelerators, Spectrometers, Detectors and Associated Equipment, 434*(2-3), 435-443.

Kanti, P. (2009). *Black holes at the large Hadron collider*. In Physics of Black Holes (pp. 387-423). Springer Berlin Heidelberg.

Kempf, A. (1997). On quantum field theory with nonzero minimal uncertainties in positions and momenta. *Journal of Mathematical Physics, 38*(3), 1347-1372.; Kempf, A., Mangano, G. (1997). Minimal length uncertainty relation and ultraviolet regularization. *Physical Review D, 55*(12), 7909.

Kempf, A., Mangano, G., Mann, R. B. (1995). Hilbert space representation of the minimal length uncertainty relation. *Physical Review D, 52*(2), 1108.

Kikuchi, T., Okada, N. (2008). Unparticle dark matter. *Physics Letters B, 665* (4), 186-189.

Lee, K. Y., Kim, Y. G., Shin, S. (2008). Singlet fermionic dark matter. *Journal of High Energy Physics, 2008*(05), 100.

Kusenko, A., Shaposhnikov, M. (1998). Supersymmetric Q-balls as dark matter. *Physics Letters B, 418*(1), 46-54.

Landsberg, G. (2006). Black holes at future colliders and beyond. *Journal of Physics G: Nuclear and Particle Physics, 32*(9), R337.

Landsberg, G. (2015). Searches for extra spatial dimensions with the CMS detector at the LHC. *Modern Physics Letters A, 30* (15), 1540017.; Landsberg, G. (2015). *Black Holes at the Large Hadron Collider.* In Quantum Aspects of Black Holes (pp. 267-292). Springer International Publishing.

Ledroit-Guillon, F. (2015). Constraints on extra dimensions from the ATLAS experiment at the LHC. *Modern Physics Letters A, 30*(15), 1540016.

Lightman, A. P., Press, W. H., Price, R. H., Teukolsky, S. A. (2017). *Problem book in relativity and gravitation.* Princeton University Press.

Martin, A. D., Stirling, W. J., Thorne, R. S., Watt, G. (2010). Heavy-quark mass dependence in global PDF analyses and 3-and 4-flavour parton distributions. *The European Physical Journal C-Particles and Fields, 70*(1), 51-72.

Maggiore, M. (1993). A generalized uncertainty principle in quantum gravity. *Physics Letters B, 304*(1-2), 65-69.

Magueijo, J., Smolin, L. (2003). Generalized Lorentz invariance with an invariant energy scale. *Physical Review D, 67*(4), 044017.

Barrow, J. D., Copeland, E. J., Liddle, A. R. (1992). The Cosmology of black hole relics. *Physical Review D, 46* (2), 645.; Carr, B. J., Gilbert, J. H., Lidsey, J. E. (1994). Black hole relics and inflation: Limits on blue perturbation spectra. *Physical Review D, 50*(8), 4853.

Meade, P., Randall, L. (2008). Black holes and quantum gravity at the LHC. *Journal of High Energy Physics, 2008*(05), 003.

Medved, A. J. M., Vagenas, E. C. (2004). When conceptual worlds collide: the generalized uncertainty principle and the Bekenstein-Hawking entropy. *Physical Review D, 70*(12), 124021.

Meissner, K. A. (2004). Black-hole entropy in loop quantum gravity. *Classical and Quantum Gravity, 21*(22), 5245.

Misner, C. W., Thorne, K. S., Wheeler, J. A. (2017). *Gravitation*. Princeton University Press.

Mohapatra, R. N., Teplitz, V. L. (2000). Mirror dark matter and galaxy core densities. *Physical Review D, 62*(6), 063506.

Myers, R. C., Perry, M. J. (1986). Black holes in higher dimensional space-times. *Annals of Physics, 172*(2), 304-347.

Nozari, K., Mehdipour, S. H. (2006). Black holes remnants in extra dimensions and dark matter. *International Journal of Modern Physics A, 21*(23n24), 4979-4992.

Nozari, K., Sefidgar, A. S. (2007). On the existence of the logarithmic correction term in black hole entropy-area relation. *General Relativity and Gravitation, 39*(4), 501-509.

NNPDF Collaboration, Ball, R. D., Bertone, V., Carrazza, S., Deans, C. S., Del Debbio, L., Forte, S., ... Ubiali, M. (2015). Parton distributions for the LHC Run II. *Journal of High Energy Physics, 2015*(4), 40.

Orbaker, D., Cms collaboration. (2010). Fast simulation of the CMS detector. *In Journal of Physics: Conference Series (Vol. 219, No. 3, p. 032053).* IOP Publishing.

Padmanabhan, T. (2005). Gravity and the thermodynamics of horizons. *Physics Reports, 406*(2), 49-125.

Particle Data Group Collaboration, Olive, K. A., Particle Data Group. (2014). Review of particle physics. *Chinese physics C, 38*(9), 090001.

PDF4LHC, Butterworth, J., Carrazza, S., Cooper-Sarkar, A., De Roeck, A., Feltesse, J., Forte, S., ... McNulty, R. (2016). PDF4LHC recommendations for LHC run II. *Journal of Physics G: Nuclear and Particle Physics, 43*(2), 023001.

Peebles, P. J. E. (1982). Large-scale background temperature and mass fluctuations due to scale-invariant primeval perturbations. *Astrophys Journal, 263,* L1-L5.

POG, J., https: //twiki.cern.ch/twiki/bin/view/CMS/MissingETOptionalFiltersRun2

Randall, L., Sundrum, R. (1999). Large mass hierarchy from a small extra dimension. *Physical Review Letters, 83*(17), 3370.; Randall, L., Sundrum, R. (1999). An alternative to compactification. *Physical Review Letters, 83*(23), 4690.

Read, A. L. (2002). Presentation of search results: the CLs technique. *Journal of Physics G: Nuclear and Particle Physics, 28*(10), 2693.

Sanchez, N. (1978). Absorption and emission spectra of a Schwarzschild black hole. *Physical Review D, 18*(4), 1030.

Scardigli, F. (1999). Generalized uncertainty principle in quantum gravity from micro-black hole gedanken experiment. *Physics Letters B, 452* (1), 39-44.

Wu, S. Q. (2005). New formulation of the first law of black hole thermodynamics: a stringy analogy. *Physics Letters B, 608*(3), 251-257.

Smarr, L. (1973). Mass formula for Kerr black holes. *Physical Review Letters, 30*(2), 71.

Solodukhin, S. N. (1999). Conformal description of horizon's states. *Physics Letters B, 454*(3), 213-222.

Strominger, A., Vafa, C. (1996). Microscopic origin of the Bekenstein-Hawking entropy. *Physics Letters B, 379*(1), 99-104.

Veneziano, G. (1986). A stringy nature needs just two constants. *EPL (Europhysics Letters), 2*(3), 199.

Wald, R. M. (2010). *General relativity*. University of Chicago press.

Weinberg, S. (1967). A model of leptons. *Physical Review Letters, 19*(21), 1264.

Working group, M., https://indico.cern.ch/20151203METChargedHadronMuonTrackFilters

Xiang, L., Wen, X. Q. (2009). A heuristic analysis of black hole thermodynamics with generalized uncertainty principle. *Journal of High Energy Physics, 2009*(10), 046.

Yang, C. N., Mills, R. L. (1954). Conservation of isotopic spin and isotopic gauge invariance. *Physical Review, 96*(1), 191.

Zarei, M., Mirza, B. (2009). Minimal uncertainty in momentum: the effects of IR gravity on quantum mechanics. *Physical Review D, 79*(12), 125007.

Zwicky, F. (1933). The redshift of extragalactic nebulae. *Helvectia Physica Acta, 6,* 110.